Generation, flow and manipulation of a microfoam

Jan-Paul Raven

UNIVERSITÉ JOSEPH FOURIER – GRENOBLE I

N° attribué par la bibliothèque

- - - - - - - - - -

THÈSE

pour obtenir le grade de

DOCTEUR DE L'UJF

Spécialité : Physique

préparée au Laboratoire de Spectrométrie Physique

dans le cadre de **l'École Doctorale de Physique**

par

Jan-Paul RAVEN

soutenance le 24 octobre 2007

MICRO-MOUSSE : GÉNÉRATION, ÉCOULEMENT ET MANIPULATION

GENERATION, FLOW AND MANIPULATION OF A MICROFOAM

Directeurs de thèse :

Philippe MARMOTTANT
François GRANER

JURY

M.	Christophe BAUDET	,
Mme	Annie COLIN	, Rapporteur
M.	Patrick TABELING	, Rapporteur
M.	Philippe MARMOTTANT	, Co-directeur de Thèse
M.	François GRANER	, Directeur de Thèse
M.	Michel VERSLUIS	,

Remerciements

Voici enfin l'occasion d'un peu de rétrospection sur les trois années de thèse passées à Grenoble, et de remercier tous les gens sans l'aide de qui ce séjour aurait été impossible.

Je remercie en premier lieu mes directeurs de thèse, Philippe et François. Philippe, merci de m'avoir proposé de venir faire une thèse avec toi à Grenoble. Ton encadrement a été excellent, plus directif au début, plus sur les grandes lignes vers la fin, mais toujours avec beaucoup de patience et de tolérance envers mon attitude parfois un peu trop pessimiste. François, merci de m'avoir permis d'intégrer l'équipe des mousseux et d'avoir accepté de co-encadrer ma thèse, ce qui, vu le fait qu'on se connaissait à peine avant le début de la thèse, montre une confiance presque aveugle que j'espère avoir méritée. Merci aussi pour tes conseils pour tout ce qui est communication scientifique : articles et exposés oraux. Mon travail en a beaucoup profité.

Je remercie les membres du jury, en premier lieu les rapporteurs Annie Colin et Patrick Tabeling, pour leur examen approfondi de ce manuscrit. Je remercie Christophe Baudet pour avoir accepté de présider le jury et Michel Versluis d'avoir fait le déplacement des Pays-Bas, d'avoir amené Benjamin "dans tes bagages" et pour le petit moment de détente pendant la séance des questions qui était ton discours en hollando-français parfait.

Un merci aussi à tous celles et ceux avec qui j'ai pu collaborer pendant ma thèse. Wiebke, l'optimisme et la créativité que tu as montrés, pendant les deux semaines que tu a passées au labo au printemps 2005, étaient plus que bienvenu dans cette période un peu ingrate de montage de manip. Wim, pour notre collaboration sur les très petites bulles qui m'a permis de rester en contact avec le laboratoire Physics of Fluids de l'université de Twente où j'ai effectué mon Master. Je te remercie David pour ton aide avec les manips acoustiques pendant ton stage de M2, et je te souhaite beaucoup de succès pour ta thèse. Magalie, merci de m'avoir hébergé quelques jours à Harvard avant l'APS 2005 et d'avoir organisé une visite des équipes là-bas qui travaillent sur la microfluidique.

Un grand merci à tous ces gens du labo sans qui ma thèse n'avait sûrement jamais vu le jour. Benjamin, un énorme merci pour toi. Ton support pendant le début de ma thèse a été d'une valeur inestimable. Dès mon arrivé des Pays-Bas en tant que jeune thésard naïf, tu a été un grand aide pour mon intégration à Grenoble et au labo. Merci pour les innombrables discussions qui n'étaient pas seulement très agréables mais aussi très utile pour me repérer dans ce très beau pays au fonctionnement quand même très différent de ce que je connaissais auparavant. Aussi un grand merci à Christophe, mon "collègue de promotion", pour toutes les soirées jeux, les chasses aux champignons et toutes les "micro"-

pauses. Mon co-bureau Catherine, je te remercie pour l'ambiance agréable et détendue dans notre bureau et pour avoir enrichi considérablement mon vocabulaire en français. Merci aux compagnons de pétanque, Christophe, David, Gwennou, Yoann, merci à Malika, Maud et Catherine pour avoir amené une touche de féminité dans un monde de brutes, et à tous les autres thésards qui ont agrémenté mon séjour au labo : Jos, Giovanni, Cyrille, BJ, Philippe R. G., Isabelle, Pascale, Cécile, Andrea et Shirin.

Ik zou hier ook graag al mijn Nederlandse vrienden willen bedanken, die hebben laten zien dat "uit het oog, uit het hart" lang niet altijd opgaat. Alexander, Cas, Herrie, Jaap, Jasper, Jiri, Maaike, Maarten-Jan, Martijn, Sander, Sjors en Theo, jullie vele bezoekjes waren een waar genoegen en jullie masale aanwezigheid tijdens de verdediging een hele steun! Ook bedankt voor alle halve waarheden die jullie rondgestrooid hebben op de borrel na afloop, mijn collega's hebben het zeer gewaardeerd :-).

De ereplaats in dit dankwoord is gereserveerd voor mijn ouders. Jullie niet aflatende ondersteuning van mijn keuzes was essentieel voor het succes van dit verblijf ver van huis.

Ces trois années de thèse étaient très riches, en tant que expérience professionnelle et surtout sur le plan humain. Merci encore à tous les gens qui m'ont accompagnés pendant.

Contents

Chapter 1

Introduction

The work presented in this thesis is at the intersection of two domains: the old and still very active domain of foam research and the recently appeared field of microfluidics. In this chapter we will sketch the context for this work, both in the foams and in the microfluidics field (section 1.1). Then we will briefly present the most important concepts, issuing from recent developments, that we will need in the following chapters (section 1.2). Finally, we will show our expectations upon the application of microfluidic techniques and lengthscales to foams, and give an outline of the work presented in the following chapters.

1.1 Context

1.1.1 Foams

Gas, liquid and surfactant

A foam consists of gas bubbles, surrounded by liquid (in a quantity typically ten to a hundred times less than the gas) and stabilized by surfactants (typically ten to hundres times less than the liquid). An important property to characterize a foam is its liquid fraction: for large liquid quantities (between 10 to 30%, "wet foam") a foam consists of round bubbles surrounded by thick liquid films; for lower liquid quantities (down to 1%, "dry foam") bubbles assume polyhedral shapes separated by thin liquid films.

Every gas-liquid interface costs a certain energy per unit of surface, called surface tension. This energy determines the shape that the bubbles assume: the one that, for a given volume, minimizes their surface. An isolated bubble will take the form of a sphere. In a foam a bubble is hindered in its relaxation to a spherical shape by the presence of the other bubbles.

Foam stability is guaranteed by the presence of amphiphilic, or "surfactant" (from the contraction of surface and active) molecules, with a hydrophilic polar (usually bearing an electrical charge or dipole) head and a hydrophobic, apolar

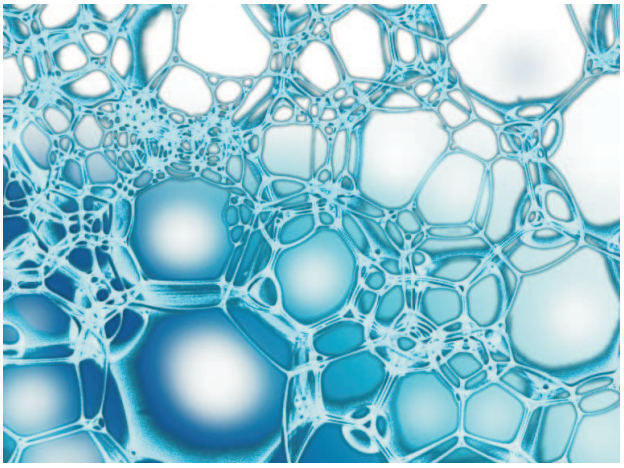

Figure 1.1: A foam.

tail. These molecules prefer a position at the gas-liquid interface, thereby decreasing the surface tension compared to the one for the pure liquid. Above a certain critical concentration (the critical micellar concentration or CMC), interfaces are saturated with surfactant, and the surface tension does not vary any more. Two surfaces covered with charged molecules have a tendency to repel each other, thereby stabilizing the liquid films. Furthermore these surfactant monolayers have mechanical properties that can influence the foam behavior [12, 13].

In a dry foam at equilibrium bubbles are separated by thin liquid films. Three of these films meet in a so-called Plateau border, and four Plateau borders meet in a vertex. In a bulk foam three films will meet under equal 120° angles, and four Plateau borders join at the tetrahedal angle $\arccos(-1/3) \simeq 109.5°$. These equal angles are due to the constant tension in each film, leading to Plateau's equilibrium rules [66].

The foams that we will encounter in this thesis are quasi 2D foams. These foams just present one layer of bubbles, that flows in a rectangular channel. This geometrical constraint due to the channel walls leads to different equilibrium angles for Plateau borders and vertices where they are in contact with the channel walls. Fig. 1.2 now introduces the nomenclature for the foam structure that we will adopt in this thesis. In a channel, a foam has films between bubbles (Fig. 1.2a), but also between a bubble and the horizontal (b) and vertical walls (c). Three films meet in a Plateau border (d) (at an angle of 120° for a dry foam at equilibrium). A film and two wall films meet in a wall Plateau border (e and f) (at 90° equilibrium angles). In a channel geometry vertices are the points where a Plateau border and three wall Plateau borders (g), or four wall Plateau borders meet (h). Note that the 109.5° tetrahydral angle does not exist in quasi 2D foams. There is no physical difference between horizontal and vertical wall films, neither between horizontal and vertical wall Plateau borders.

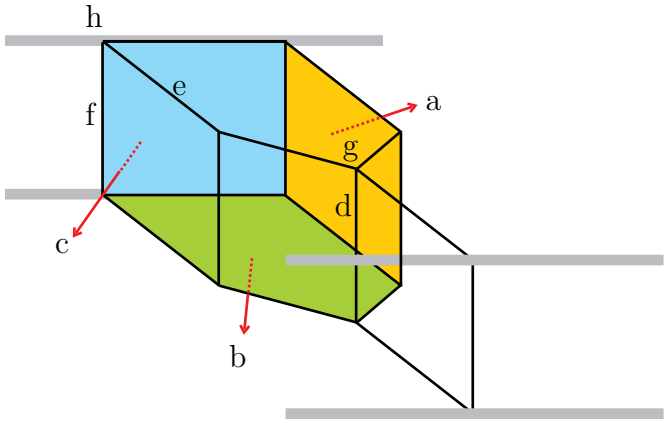

Figure 1.2: Quasi 2D foam nomenclature: (a) film, (b) horizontal wall film, (c) vertical wall film, (d) Plateau border, (e) horizontal wall Plateau border, (f) vertical wall Plateau border, (g) vertex and (h) wall vertex

Although the films are stabilized by surfactants, a liquid foam evolves and has a limited lifetime. Two phenomena govern this evolution: drainage and coarsening. Drainage is the flow, usually due to gravity, of the liquid in the films and Plateau borders: it tends to dry and thereby fragilize a foam. Furthermore gas tends to flow from high to low pressure bubbles by means of the liquid interfaces. As pressure is related to size large bubbles will become larger and small bubbles smaller until they disappear: the coarsening phenomenon.

Foam properties and applications

A foam contains a multitude of lengthscales: from molecular for the surfactants, to micronic for the liquid films, to submillimetric for the Plateau borders and up to millimeters or centimeters for the gas bubbles. Together with the surface tension, they give rise to the foam's sometimes exotic properties, which we will discuss and illustrate with a few examples.

A foam is typically very light, due to the low liquid content. It is this property that makes it particularly useful in firefighting: a foam, as opposed to water, is light enough to float on hydrocarbons. Furthermore, because of the small liquid content, a very large surface can be covered with only little soap solution by adding air on the spot. This same property is exploited in the use of foams to clean nuclear power plants. Compared with pure liquid cleaning, the amount of water that has to be decontaminated afterwards decreases with a factor ten to twenty. Another application is in ore seperation: the ore is trapped in the films of a foam that floats on a suspension of ore, debris and liquid [32].

Foams show a particularly rich rheological behavior. It is an example of a complex fluid showing elastic, plastic and viscous behavior. Although its main

constituants are a gas and a liquid one obtains a material that is situated in between an elastic and plastic solid and a viscous liquid. An example of this triple behaviour that many of us encounter on a daily basis is shaving cream. After applying it on a hand, it stays in place, behaving like a solid. Upon a small displacement, it comes back to its initial shape (elasticity). Upon applying a larger constraint (to spread it on a face), the foam starts flowing, with bubbles moving with respect to eachother (plasticity). In foam flows at high shear rate (under the razor blade) dissipation in films and Plateau borders, where liquid accumulates, becomes significant (viscosity) [66].

This complex rheological behavior lies at the basis of many applications *e.g.* in cosmetics, food industry and petroleum engineering where a material is sought that can be applied with the ease of a liquid, but after that stays in place like a solid [32].

Foam research has a long tradition and is still a very active field, both driven by applications and by fundamental interest. The triple mechanical behaviour intrigues many scientists, and foams have the advantage that the lengthscale of the individual objects which is at the basis of many phenomena (the bubble size) is easily experimentally accessible. This makes it a good model system for other complex materials. Note that the use of foams as a model system has a long tradition, as is demonstrated by Kelvin's work in which a foam is used as a model for the structure of the "ether" in which light is supposed to propagate [66].

1.1.2 Microfluidics and Lab-on-a-chip

Microfluidics deals with the manipulation of very small ($\leq 10^{-9}$ l) liquid quantities in artificial microsystems [58, 56]. It is a fast growing domain, with the potential to influence among others biology, chemistry and medecine. The miniaturising of laboratory equipment concerning fluid flows (lab-on-a-chip concept) holds a promise inspired by the enormous effect of the information revolution that followed the transition from electronics to micro-electronics [56]. Among the potential capabilities are: the ability to use very small quantities of samples and reagents, hence to work at low cost with a high resolution and sensitivity to separate and detect; short times for analysis; possibility of parallelization [67, 56].

Microfluidics is a young field. Large scale industrial applications are rare, among which the most well known is inkjet printing [58]. On a smaller laboratory scale some examples of microfluidic systems include the screening of conditions for protein cristallization, high througput screening in drug development and the examination and analysis of a single cell or molecule [56]. Proof of principle for the implementation on microfluidic chips exists for many kind of functional elements including valves, pumps, actuators, switches, sensors, dispensers, mixers, filters, separators, heaters *etc.* [57].

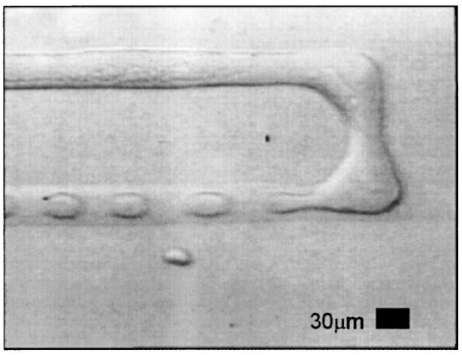

Figure 1.3: Droplet generation in a T junction. From [61]

Two-phase microfluidics

The first demonstration of the generation of bubbles and drops in a way that can easily be integrated in microfluidic devices is only as recent as 2001 (Fig. 1.3) [61]. In the time since a plethora of different systems has been developed and studied (see [10] for a recent review). Two-phase microfluidics offers new ways to produce drops and bubbles, with very good control over size and uniformity in comparison with conventional methods.

In a lab-on-a-chip context, droplets are conceived as miniature 'beakers' allowing to conduct chemical reactions and analyzes inside. The use of droplets allows for control over the spatial distribution of very small sample quantities that can be transported in a chip without contaminating walls (due to the continuous liquid film surrounding the drop). Operations like mixing, drop coalescence and sorting have been demonstrated [56].

On-chip generation of drops and bubbles also allows for the synthesis of precise materials such as highly uniform microparticles such as ultrasound contrast agents, compound droplets, emulsions and in the context of this thesis: microfoams [10].

The novelty of this approach is that foams and emulsions can be produced 'bottom-up', one bubble or drop at a time, with potentially a better control over the resulting material properties.

1.2 State of the art

1.2.1 Microdrops and -bubbles

In this section we will limit ourselves to drop and bubble generation methods that can be integrated in a microfluidic chip: those that are produced using lithography-derived techniques. This implies that device geometries will be planar, with rectangular channels that have a uniform depth.

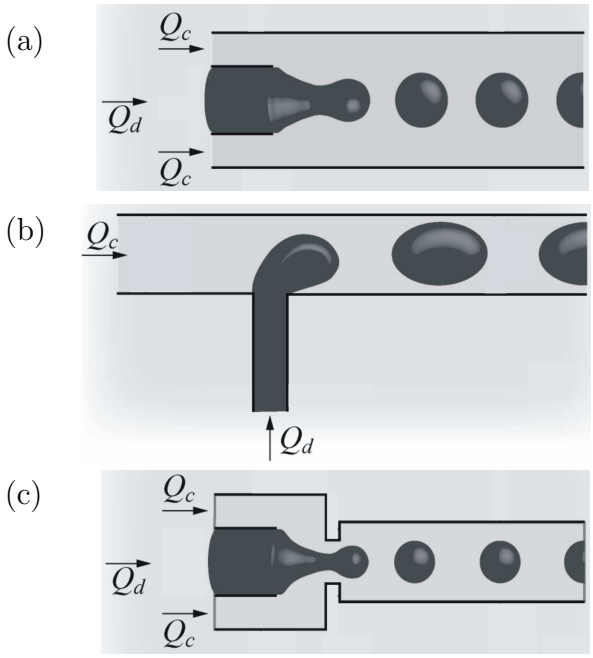

Figure 1.4: Three main microfluidic geometries used for droplet formation: (a) cross-flowing streams, (b) co-flowing streams and (c) flow focusing. Q_c: flow rate of the continuous phase. Q_d: flow rate of the dispersed phase. From [10].

Cross flowing streams: T junctions

The first, and probably most reproduced since, method to produce on-chip droplets was first reported in 2001 by Thorsen *et. al.* [61] (Fig. 1.3 and Fig. 1.4a). It consists of two cross flowing streams of inmiscible liquids (usually water and oil). The liquids meet at a so-called T junction. For certain ratios of the liquid flow rates the stream that least wets the channel walls breaks up in uniform bubbles.

The geometry plays a determininant role in the mechanism for droplet generation. Two extreme cases correspond either to $w_d/w_c \ll 1$ or $w_d/w_c \simeq 1$, with w_d the width of the part of the channel with the dispersed phase and w_c the width for the part of the channel containing the continuous phase.

For $w_d/w_c \ll 1$ droplet size is a result of a competition between between surface tension σ, trying to keep a circular shape for the interface, and viscous stresses that deform the interface in the direction of the flow of the continuous phase. This introduces the dimensionless capillary number Ca as the ratio between viscous forces and surface tension:

$$Ca = \frac{\mu v}{\sigma}, \tag{1.1}$$

with μ the viscosity and v a typical speed (or more precisely: a typical velocity gradient times a typical length). And indeed droplet size is found to depend solely of Ca, with v based on the flow rate Q_c of the continuous stream divided by the channel section: $v = Q_c/S$ [36]. For increasing Ca droplet size decreases.

In the opposite case where $w_d/w_c \simeq 1$, the emerging droplet grows enough to completely obstruct the continuous phase channel (with the exception of a thin liquid film surrounding the droplet). Now, drop pinch-off is dominated by the force due to the pressure build-up in the continuous phase upstream of the drop. This pressure build-up is due to the dispersed phase blocking the continuous phase channel. It will lead to a displacement of the tip of the dispersed phase into the outlet channel, and eventually to drop detachment. A simple model states that the drop size depends on the ratio of the dispersed and the continuous flow rate Q_d/Q_c, independently of Ca as was experimentally verified over the range $Ca \in [10^{-4}, 10^{-2}]$. The displacement of the tip of the dispersed phase is proportional to Q_c, yielding a typical time τ of drop detachment that depends on Q_c. Drop length is the volume due to influx of the dispersed phase during τ: $Q_d\tau$, plus an initial volume when the drop starts obstructing the channel:

$$\frac{L}{w_c} = 1 + \xi\frac{Q_d}{Q_c}, \tag{1.2}$$

with L the length of the drop, here normalized by the outlet channel width, and ξ a factor close to unity depending on the channel geometry [25].

The transition between a regime where drop volume only depends on the ratio of flow rates, and the one where viscous stresses start playing a role is argued to

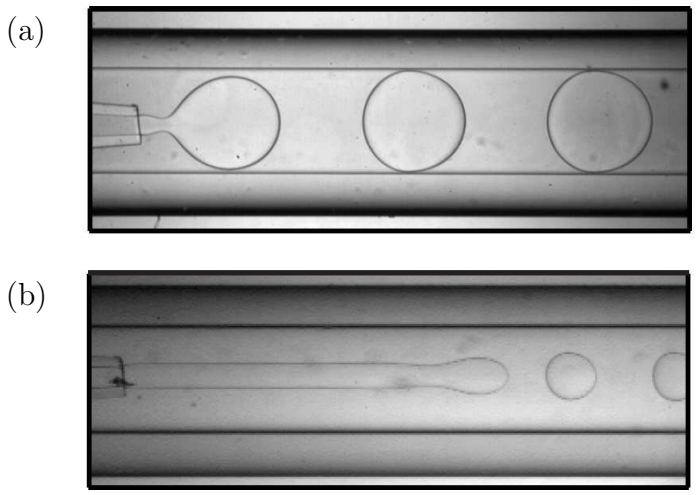

Figure 1.5: Dripping (a) and jetting (b) in a coflow in a cylindrical geometry. Pictures from [34]

take place for a width of the dispersed phase channel that is half the width of the continuous channel: $w_d = w_c/2$ [25].

Drops only form for a specific flow parameter range, mostly depending on the flow rate ratio Q_d/Q_c: approximatively for $Q_d/Q_c \leq 1$. For higher ratios, drop formation stops and the two streams form a co-flow in the outlet channel. A phase diagram and a model predicting the transition from droplet formation to parallel flow are given in [33].

Co-flowing streams

A second geometry that allows for droplet generation is the one employing a set of concentric channels (Fig. 1.4b). This creates a co-flow, which in the case of two immiscible liquids leads to break-up in drops of the inner thread for a certain range of the flow parameters. This geometry can be produced by jamming a square cross-section capillary with a tapered end, in a cylindrical capillary [34]. So strictly speaking, this method does not fulfill the criteria for implementation on a microfluidic chip (*i.e.* using 2D photolithography). On the other hand, the use of glass capillaries leads to robust devices with good wetting properties.

Drop formation in a co-flow geometry is the result of the development of a capillary instability. Two droplet formation regimes are observed: dripping and jetting [11]. In the dripping regime, drop formation takes place directly at the end of the dispersed phase channel (Fig. 1.5a). In the jetting regime, a jet is formed that subsequently breaks up into drops (Fig. 1.5b). In a recent paper [34] the different regimes have been related, by a stability analysis, to the nature of the capillary instability: an absolute instability leads to dripping and a convective to

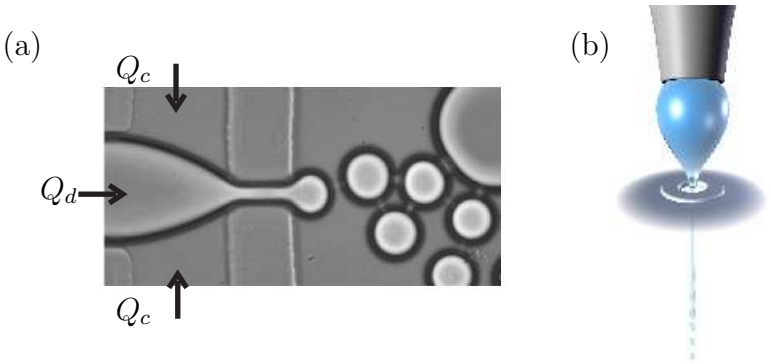

Figure 1.6: Drop generation in flow focusing geometries. (a) on a microfluidic chip, from [2]. (b) axisymmetric, from [68].

jetting.

2D flow focusing

A third method for generating drops is shown in Fig. 1.4c. In addition to the co-flow geometry it presents a small orifice in front of the outlet channel, through which both liquids must pass.

This method was first implemented on a microfluidic chip in 2003 by Anna *et. al.* [2] (Fig. 1.6a). It is an adaptation of the macroscale axisymmetric flow focusing principle in which a gas is blown out of a capillary into a liquid bath. The capillary is positioned above an orifice. The flow in the surrounding liquid is forced through this orifice, thereby creating a flow that focuses the gas into a thin jet which breaks up in bubbles [31, 30] (Fig. 1.6b).

The flow focusing method has an early precursor. Already in 1949 a device capable of producing monodisperse bubbles with diameters down to 240 μm was reported [54] (Fig. 1.7). It was used to create rafts of bubbles floating on soap solution. These bubble monolayers were applied to demonstrate aspects of crystal structure like grain boundaries and dislocations: an example of the use of foams as a model system.

The first to investigate bubble formation in a planar flow focusing geometry were Garstecki and co-workers [28]. They find, for $Ca \ll 1$ a linear relation between the flow parameters and the bubble volume V_b:

$$V_b = \frac{P_d}{\mu_c Q_c}, \tag{1.3}$$

with P_d the pressure in the dispersed phase. The bubble formation mechanism is explained as follows: both the gas and liquid flow have to pass through the small

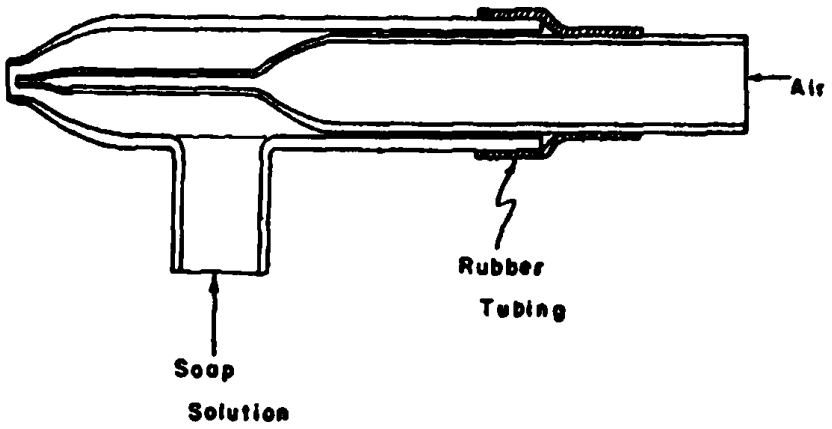

Figure 1.7: Device for the generation of small bubbles by break-up of a gas jet after a gas-liquid co-flow through a small nozzle. From [54].

orifice at the entrance of the outlet channel. When the gas thread enters this orifice it effectively blocks the access for the liquid flow. The subsequent pressure build-up pinches the gas thread, and detaches a bubble. This argument is similar to the one for drop formation at low Ca in T junctions. With the pinching time τ depending on Q_c, and V_b equal to $Q_d\tau$ with $Q_d \propto P_d/\mu$ (assuming Poiseuille flow in the exit channel), they obtain equation 1.3 [28].

Bubble size is found to be independent of surface tension. Probably because the gas-liquid interface is stable against capillary instabilities during a large part of bubble pinch-off [29].

For moderate Weber numbers, giving the ratio of inertial forces to surface tension, a rich bubble pinch-off behavior is found, including period doubling, period halving and chaotic bubbling [27]. This is due to inertial effects related to the fast retraction upstream of the gas thread after bubble detachment.

The planar flow focusing method is the only one, from the three methods mentioned here, that can generate droplets or bubbles at low volume fractions of the continuous phase, a necessary prerequisite for the generation of dry foams. Therefore in this thesis we will use and study this 2D flow-focusing geometry.

Two-phase microflows

A very large part of the literature on two-phase microfluidics deals with the generation of droplets and bubbles. Now that these generation processes start being reasonably well known (at least qualitatively), the subsequent flow is receiving more attention.

Drops can be used as mixers. The recirculation pattern in a droplet while flowing in a zigzagging channel has been used to achieve rapid mixing of different reagents. Now, every droplet position in the channel corresponds to a certain

time after mixing of the reagents and initiation of the reaction. By matching typical displacement times and reaction times, reaction kinetics can be studied and exploited. This time-to-distance transformation has *e.g.* been used in [55] and [53].

Bubbles too have been used as mixers. Now the mixing does not take place in the dispersed phase, but in the continuous phase (liquid slugs) between bubbles (that apart from a thin wetting film completely fills the channel width) [23, 24]. Mixing with bubbles or drops offers the advantage that they are passive methods: no external actuation is necessary to make them function.

Flows in more complex channel geometries are also subject to study. Bifurcating channels can be used for controlled droplet break-up [42, 45], or to study droplet partitioning in the two branches [22]. Also the issue of parallelization, the coupling of multiple droplet generation elements to the same inlet channels, is receiving attention. This step is essential in the upscaling of the droplet production to quantities sufficient for practical significance, but is difficult: the coupling of two T junctions has been shown to lead to complex dynamical behavior including synchronization, quasiperiodicity and chaos [4]. Logical control operations are possible with a flow of bubbles in a microfluidic channel system *e.g.* AND/OR/NOT gates, a toggle flip-flop and a ring oscillator [47]. It opens up perspectives for the description and control of bubble flows in a lab-on-a-chip context by the well developed language of computation.

1.2.2 Foams

In this section we will very briefly introduce recent developments in those fields of foam physics that are most related to the work in these thesis. We will we will recall recent work on 2D foam flows. After that we introduce some concepts of friction in foam flows through channels. To end, we will discuss the concept of discrete microfluidics.

Quasi 2D foam flow

It is easy to make a foam: blowing with a straw in a soapy liquid is enough. But it is hard to visualize: a foam is a highly diffusive medium. The most performant method, X-ray tomography, works on times scales that are too long to visualize flowing bubbles [38], although fast progress is being made. So far, the easiest way to study a foam flow is by creating a single bubble layer, a quasi 2D foam, keeping in mind that the friction on the confining plates adds a term with respect to 3D flows. This approach also presents the advantage of simplifying the theoretical analysis.

Our lab has a strong experience in the use of quasi 2D flows to study foam rheology (see *e.g.* [18, 15]). Different setups have been developed to study the flow of a foam around an obstacle (Stokes experiment). For low speed foam

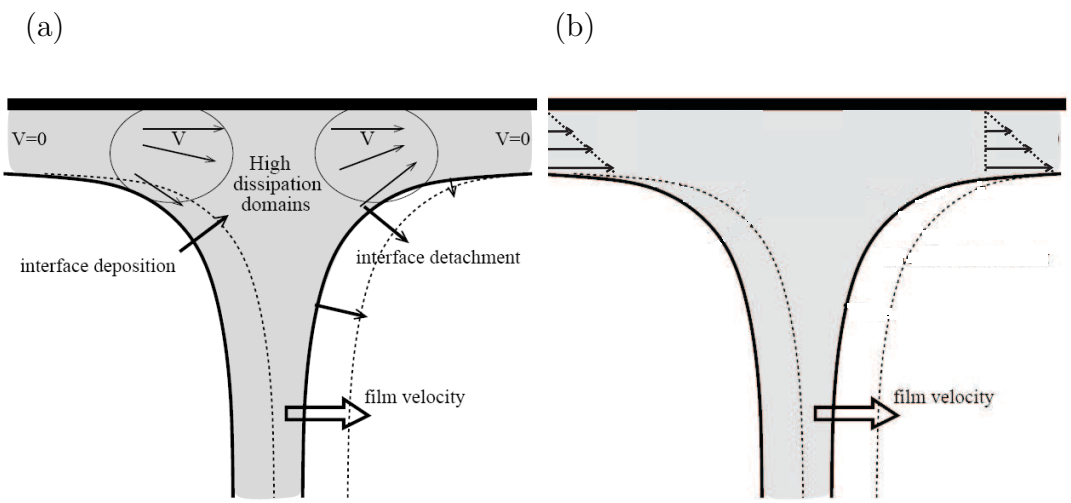

Figure 1.8: Dissipation in foam plug flows. (a) dissipation localized in the Plateau borders. Image from [9]. (b) dissipation in the thin wall films.

flow the geometry of the confined bubble raft was employed [17]. Here bubbles are confined between a liquid pool below and a glass plate above. Higher foam speeds have been investigated in a Hele-Shaw configuration, where the 2D foam is completely confined between glass plates [50].

The force exerted by the foam on the obstacle can be measured. In the same time the obstacle deforms the foam by imposing both an elongational and shear flow. The force measurement and the analysis of the flow field are used to create a database to test different rheological models. Furthermore this kind of experiments enables to investigate the coupling between the individual (single bubble) and the global (foam) level.

Dissipation

The 2D-foam flows that we will encounter in this thesis behave like a plug flow. Bubbles do not move with respect to each other, this implies that all friction will be in the liquid between bubbles and the channel walls. The study of this foam-wall friction is an active subject of research [9, 60, 12, 13, 52]. Here we will give a very short overview of the basic concepts.

It is much harder to push a foam than to push the pure liquid or pure gas. The bubbles are actually confining the liquid to the thin films and Plateau borders. This implies that all dissipation is in the wall films and wall Plateau borders. The velocity gradients are much higher, leading to an effective foam viscosity that is orders of magnitude larger than the liquid viscosity.

Foam flow is an example of shear thining: the relation between pressure and flow rate follows a power law with an exponent smaller than one. Wall films and

Plateau borders swell at higher velocity, thereby leading to a smaller increase in velocity gradients. This effect was already theoretically and experimentally studied fifty years ago for the case of a single bubble by Bretherton [7].

For a more detailed study one needs to know the localization of the dissipation zones. Cantat *et. al.* propose a model in [9] that assumes all the dissipation to take place in the wall Plateau borders (Fig. 1.8a). In this model a foam flow is described to be essentially a flow of films. This model has the implicite assumption of completely liquid interfaces (as can be seen by the indication $V = 0$ in the wall film in Fig. 1.8a). Bubbles move at a non-zero speed, so there is a discontinuity in the speed at the interface, that can only exist if the interface is perfectly fluid, *i.e.* with a negligible surface viscosity.

In reality the interfaces are covered with surfactant molecules. Some of those are sufficiently fluid to allow the model described above to work. Others lead to rigid interfaces that introduce velocity gradients in the wall films (Fig. 1.8b). The above is demonstrated by the work of Denkov *et. al.* [12, 13]. Both experimentally and theoretically, different regimes are found that are related to dissipation either in wall Plateau borders or wall films.

Discrete microfluidics

Also from within the foam community thought has been given to the use of foams in microfluidics. The Dublin group developed the discrete microfluidics concept for foams (see [19] by Drenckhan and co-workers). It is a continuation of the digital microfluidics idea, which is an ensemble of methods to manipulate single drops.

The energy of a two-phase system is related to its interfacial area and therefore to its structure. Now through a certain purpose-designed channel geometry one can impose boundary counditions upon the foam structure. Driven by energy-minimization, the foam will adapt to the geometry by assuming a certain sample arrangement. [19] gives a proof of principle in millimetric channels for operations like sample separation, flipping or replacing (Fig. 1.9). The advantage compared to digital microfluidics is that now, by using the interplay between a foam and a certain geometry, a whole series of gas (or liquid) pockets can be treated in series.

The experimental results in [19] have all been reproduced by simulations with *Surface Evolver*, *i.e.* by simple surface minimisation. This succesful use of simulations opens up a method to test the functionality of channel geometries during the design phase, thereby shortening the time needed for experimental trial-and-error.

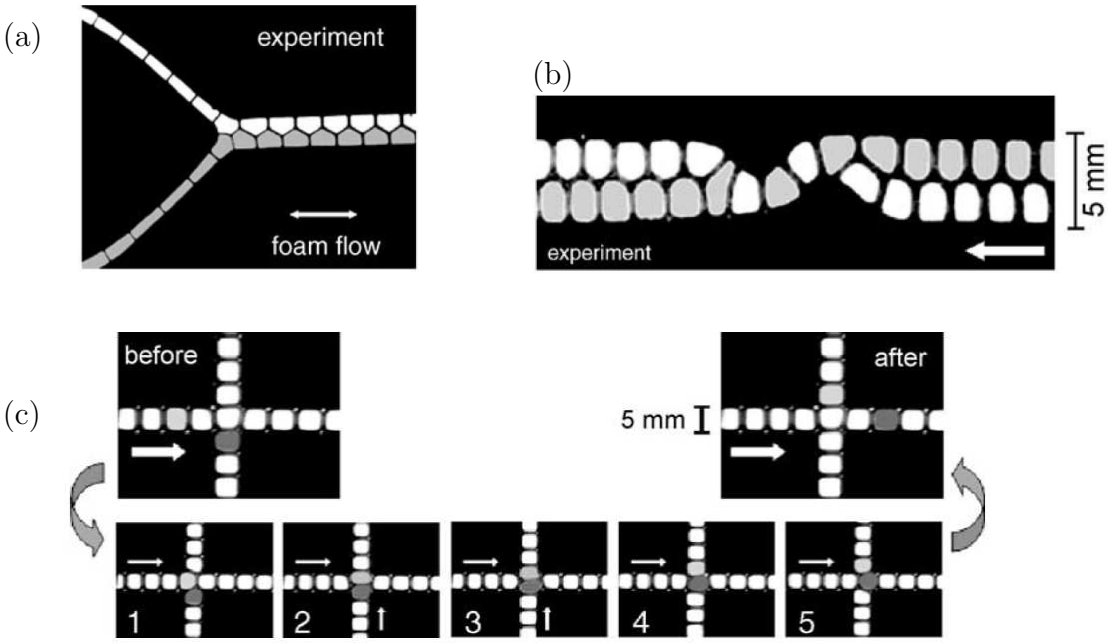

Figure 1.9: Digital microfluidics. (a) Bubble separation and merging (depending on flow direction) in an Y-junction. (b) The flipper: position of the two bubble rows is reversed due to two "bumps". (c) Bubble replacing: the bubbles in the horizontal row flow continuously. Upon application of a pressure pulse in the vertical channel, a bubble (light gray) from the horizontal channel can be replaced with a bubble (dark grey) from the vertical one. Pictures from [19].

1.3 Microfoams

We will use the word "microfoams" for those that we obtain by applying the techniques and lengthscales of microfluidics. Here we will introduce some of their properties, followed by a description of the goals and methods for this thesis.

1.3.1 Properties

Due to the smaller lengthscales involved, microfoams have potentially better controlled properties compared to macrofoams. In the following we will list these properties as we anticipated them at the start of this thesis.

- Microfluidic flow focusing geometries can produce remarkably monodisperse bubbles and drops (variation < 3 % [28]), due to the very low Re numbers involved. The assembly of these bubbles into a foam leads to foams with very good control over the bubble size. *E.g.* coarsening, one of the major factors limiting foam lifetime, is driven by pressure differences between bubbles, that are related to size differences. Higher monodispersity thus equals stable foams.

- On the scale of a 2D foam (in the xy-plane, with gravity pointing in the $-z$ direction), gravity leads to asymmetric liquid films: thin at the top and thick at the bottom. That effect should be absent in a microfoam. A microfluidic approach allows to work with channel heights h smaller than the capillary length $l_c = 2.0$ mm (for our soap solution with the surface tension $\sigma = 35$ mN/m), the critical length below which surface tension effects dominate gravity. Gravity plays an important role in macroscopic foam. It leads to the phenomenon of drainage, a liquid flow leading to the accumulation of water at the bottom of the sample. It induces a gradient of the liquid fraction, dry on top and wet at the bottom.

- The foam liquid fraction (ratio of liquid volume to total volume) is not always well controlled in a macroscopic foam. This depends on the method of foam generation; *e.g.* if a foam is produced by bubbling in a soapy liquid, the amount of liquid entrained between bubbles is not a control parameter. Furthermore it tends to change over time due to drainage. In a microfoam produced by flow focusing, the liquid flow rate is one of the control parameters. Therefore the injected liquid fraction (ratio of liquid flow rate to the total flow rate) is well known and can be varied at will.

1.3.2 Goals and methods for this thesis

Better controlled foam properties are an advantage for many studies among which that of wall dissipation. The friction force critically depends on the liquid fraction [60], and hence on the symmetry of the liquid films.

Another motivation for this thesis lies in the discrete microfluidics concept, the adaptation of foam for uses in a lab-on-a-chip environment. This principle had been demonstrated in millimetric foams and awaited downscaling. Furthermore if one wants to maximize the production of a microfluidic drop or bubble generator, apart from strategies like parallelization or high flow rates, one will want to increase bubble or drop density.

The goal of this experimental work is threefold. First, to develop a microfluidic foam generator. This implies exploring and optimizing the geometrical parameters for the flow focusing setup, and the gas and liquid flow rates. Then, to characterize the foam flow in the outlet channel. Finally, to investigate the applicability of ultrasound as a tool to manipulate a microfoam after formation.

This study is part of the desire in our laboratory to create a microfluidic activity, a development that started with the creation of a microfabrication facility upon the arrival of Philippe Marmottant in 2004. This thesis has benefitted a lot from the know-how on 2D foams from François Graner and Catherine Quilliet, and the PhD theses on 2D foam flow around an obstacle by Benjamin Dollet and Christophe Raufaste.

1.3.3 Outline

We will begin this manuscript with a description of our microfabrication protocol, followed by a presentation of our experimental setup, its control parameters and how we extract data from it (chapter 2). Then we will present in chapter 3 the generation of a microfoam and how it depends on the different flow and geometrical parameters. In chapter 4 we will show our results on the characterization of the foam flow. We will detail, among other, a retroactive effect of the flow on the bubble generation. The manipulation of bubbles by the use of acoustic forces will be demonstrated in chapter 5. We will end with a summary and the perspectives that follow from this thesis in chapter 6.

1.4 Résumé

Ce chapitre d'introduction commence avec une description du contexte de cette thèse (paragraphe 1.1), à la fois pour la domaine des mousses et pour celui de la microfluidique.

Pour les mousses nous presentons ses composants : gaz, liquide et molécules de surfactants. Nous parlons aussi de la structure de la mousse en général et, dans notre cas particulier, des mousses quasi-2D dans des canaux rectangulaires. Nous traitons quelques propriétés des mousses notamment leur poids faible et leur comportement rhéologique (élastique, plastique et visqueux) très riche. On indique aussi quelques applications de ces propriétés.

La microfluidique s'occupe de la manipulation de très petites quantités de liquide dans des microsystèmes artificiels. La microfluidique diphasique est discutée notamment dans le contexte de l'utilisation de petites gouttes, dans des systèmes de 'laboratoire sur puce', en tant que micro-conteneurs de produit.

Paragraphe 1.2 décrit l'état de l'art pour la génération de gouttes et bulles dans des systèmes microfluidiques et pour les aspects des mousses qui concernent ce travail. Pour les microgouttes et bulles trois différentes méthodes de production sont décrites : un écoulement dans une géométrie de jonction en forme de T, un co-écoulement et le méthode de focalisation hydrodynamique. Pour les mousses on discute dans un premier temps leur étude dans le contexte d'un écoulement de mousse 2D autour d'obstacle. Deuxièmement nous parlons de l'état de l'art dans l'étude de la dissipation d'un écoulement de mousse de type bouchon dans un canal. Nous finissons ce paragraphe avec une discussion de la microfluidique discrète, un concept pour manipuler la mousse, vue ici comme une ensemble de micro-conteneurs, en utilisant l'interaction entre la géométrie du canal et l'écoulement.

Le dernier paragraphe (1.3) introduit les micro-mousses: celles qu'on obtient en appliquant les techniques et les échelles de la microfluidique. Nous discutons les propriétés attendues : des bulles très monodisperses, absence de gravité et une fraction liquide injectée bien contrôlée.

Le but de ce travail expérimental est triple. D'abord, le développement d'un générateur de mousse microfluidique avec la technique de la focalisation hydrodynamique. Cela implique l'exploration et l'optimisation des paramètres géométriques pour le dispositif de focalisation hydrodynamique en fonction des débits de gaz et de liquide. Après, la caractérisation de l'écoulement de la mousse dans le canal de sortie. Et finalement, l'étude de l'applicabilité des forces ultrasonores pour la manipulation de la mousse pendant son écoulement.

Ce manuscrit de thèse commence avec une chapitre matériel et méthodes qui introduit la microfabrication et les détails du dispositif expérimental. Dans le chapitre 3 nous discutons la génération d'une micromousse et sa dépendance envers la géométrie et les paramètres de contrôles. Dans le chapitre 4 nous montrons nos résultats sur la caractérisation de l'écoulement. La manipulation des bulles avec des forces acoustiques est démontrée dans le chapitre 5. Nous finissons avec un résumé et les perspectives qui font la suite de ce travail de thèse (chapitre 6).

Chapter 2

Materials and methods

In this chapter we will describe the set of experimental techniques that we use to study the generation and flow of microfoams.

First we will present in detail how we make our micro channels using the soft lithography method [44][20]. Second we will describe the actual experimental set-up, its control parameters, how we visualise the experiments, which liquid and gas we use, and the information we can extract from the experimental results. To end this chapter, we will show preliminary results on 3D imaging for microfoams with confocal microscopy.

2.1 Microchannel production by soft lithography

This method uses traditional lithography techniques to create a template. The actual devices, which we use during the experiments, are imprints of this template in the polymer polydimethylsiloxane (PDMS). PDMS is a mechanically soft material, this, combined with the fact that its processing does not necessarily take place in a cleanroom environment, explains the origin of the name "soft"-lithography [20]. First we will describe how we make the template. Then we will detail how we make imprints of this template in PDMS and how to seal them against a glass cover slide or another PDMS surface. We will also discuss the design and use of on-chip filters to prevent dust from entering the system and possibly clogging the channels. We will end this section with a discussion of the possibilities and limits of the soft-lithography method.

The general principles of soft lithography are very well explained in references [44] and [20]. Template production depends very much on the choice of the photo curable resin, with all details given in the manufacturer's manuals. The purpose of this section is not so much to repeat the information contained in the references stated above, but to detail what is specific to our case: our experiences and slight modifications of the standard protocol.

2.1.1 Template

A short overview of the micro fabrication process including template fabrication is given in Fig. 2.1.

Wafer

We use either 2 or 3 inch silicon wafers (Siltronix). There is no need for cleaning the wafers before spin-coating. Wafers are delivered in vacuum-sealed boxes that we store in our clean-room. Therefore we consider the wafers to be free of any depot. Before use we dehydrate the wafer surface by heating on a hot-plate (typically 20 min at 200 °C). To avoid thermal shocks we let the wafer cool down to room temperature before continuing.

Resin

During this thesis we used several resins: a positive resist, ma-P 100 (Micro Resist Technology), and several negative resists, SU-8 2100 (MicroChem), SU-8 GM 1070 and GM 1060 (both Gersteltec). We quickly abandoned the use of ma-P 100 because of the poor results. The ma-P 100 layers had an inhomogeneous thickness, with cracks and a bad adherence to the wafer. SU-8 is the standard resin used in the MEMS and microfluidics community. It is an epoxy-based resine that starts polymerising after exposure to UV-light. In its polymerised form it is resistant to solvents, acids and bases. It is also mechanically very robust. The SU-8 solution consists of epoxy-molecules in a solvent (cyclopentanone for SU-8 2100). The amount of solvent controls the solution viscosity and thereby the thickness range accesible by spin coating on a substrate. Chosen the proper solution, uniform layers with a thickness from less than 1 μm up to 300 μm can be made in a single spin coat. The Gersteltec resins are about a factor two less expensive than the ones from Microchem. We obtained good results with these resins and therefore they have become our standard.

Spin coating

Spin coating is a procedure to apply a thin film on a substrate. By rotating the substrate, the solution is spread and the excess amount is removed by centrifugal forces. The final thickness mainly depends on rotation frequency and solution viscosity. There are three control parameters: acceleration, rotation frequency and spinning time. We usually spin coat in two steps. First we spin at low frequency just to spread the solution all over the wafer (spread cycle). Sometimes this step needs to be repeated several times, especially for viscous resins. Once the solution is spread, we spin at higher frequencies to obtain the final thickness.

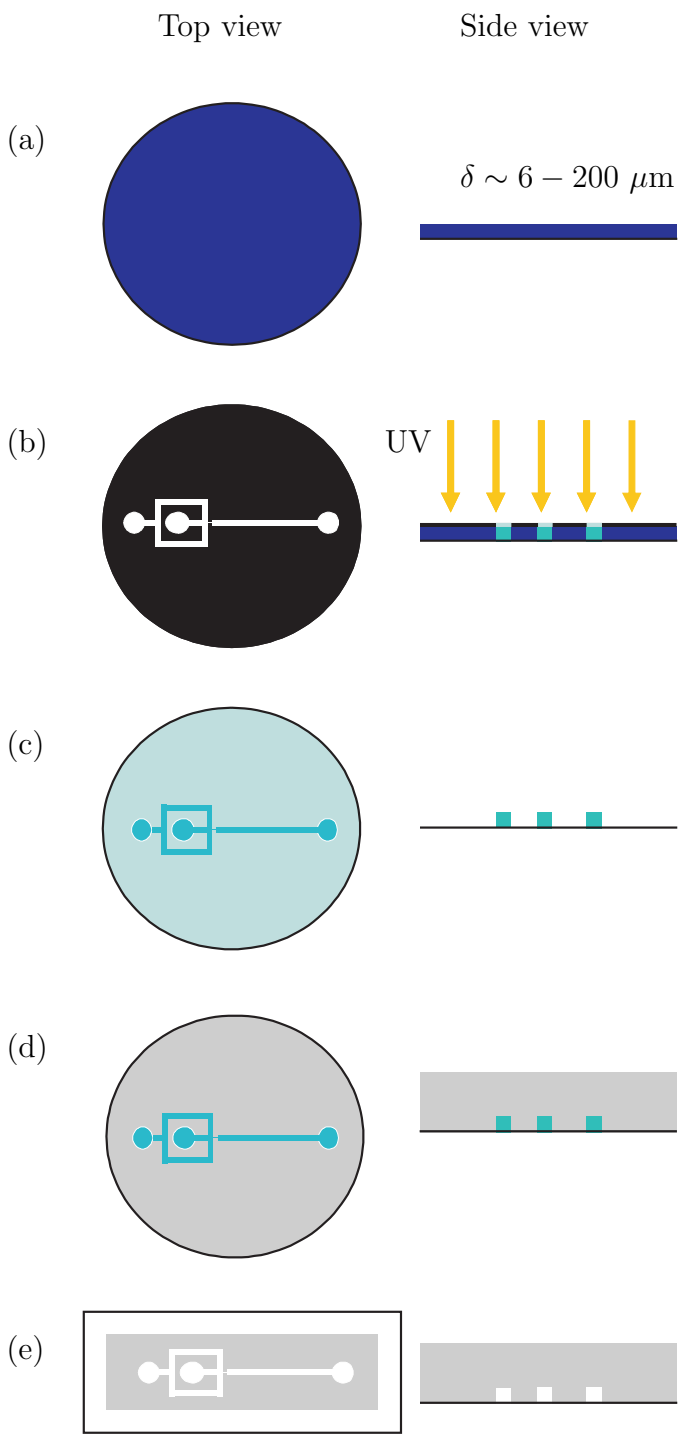

Figure 2.1: Schematic outline of the micro fabrication process. (a) A thin layer (typically in our case between 6 and 200 μm) of the photo curable resin SU-8 is applied, by spin-coating, on a silicone wafer. (b) A mask containing the design of the microfluidic system is placed in contact with the wafer. A cross-linking reaction takes places in the parts of the resine exposed to UV. (c) Development of the resin removes the non-exposed part of the SU-8. We now have the template showing in relief the structure of the microchannels. (d) A replica of the template is made in PDMS. (e) The channels in PDMS are sealed against a glass cover slide.

Pre bake

In this step the wafer is slowly heated to 95 °C to let the solvent evaporate. The required heating time increases with substrate thickness. If not all the solvent has evaporated, strong deformations of the substrate can take place after contact with the mask. The resin is also very sensitive to the Scotch tape we use to keep the mask in place. Temperature shocks are known to weaken the substrate and cause cracks and ondulations. Therefore, after every baking step, we slowly return to room temperature with a ramp of about 2 °C/min.

Masks

Our masks are transparency sheets on which the design is printed with a high precision printer at 5000 dots per inch (printershop Xyrius, Seyssinet). This means a typical dot size of about 5 μm, thereby imposing a limit to the mask's resolution. We draw our designs with the help of a home-written Matlab code that generates a file in the postscript format. The designing is text based, which allows for easy modification of the design parameters.

Exposure

We expose using a SUSS MJB3 mask aligner with lamp intensity $I = 4.3\,\mathrm{mW}/cm^2$. SU-8 should be exposed at wavelengths around $\lambda = 365$ nm. Shorter wavelengths are quickly absorbed at the surface of the resin. The presence of these wavelengths thus leads to an overexposure of the upper part of the resin, creating negatively sloped side-walls. To get rid off these wavelengths, we use a high-pass filter. This filter is a glass piece with a 50 μm thick SU-8 layer coated on it. It reduces the lamp intensity to 1.50 mW/cm^2. Exposure time increases with the thickness of the SU8 layer (typically around a minute). Too short exposure times lead to cracks in the resin's surface, too long exposure times to non-vertical side-walls.

Post bake

Exposure just initiates the polymerisation. To complete the process the wafer needs again to be heated to 95 °C and slowly cooled afterwards.

Development

After the post bake, the non-exposed SU-8 can be removed by developing in the solvent propylene glycol monomethyl ether acetate (PGMEA). Afterwards wafers should be rinced with isopropanol. Any remaining non-exposed SU-8 leads to white traces. In this case development should be prolonged until no more white traces appear during rincing.

Hard bake

Sometimes we apply a hard bake, at 160 °C for one hour, after development. This step removes any possible cracks that have appeared during the exposure and post bake. This is the last step of the template production process.

2.1.2 Imprints in PDMS

Polydimethylsiloxane (Sylgard 184) is the standard material for microfluidic chips. Its most important properties include optical transparence (a necessary condition for visualisation), ease to clean, bio-compatibility and tunable stiffness. Very small structures, down to 10 nm, can be replicated in PDMS [49].

Duplication protocol

PDMS is a two-component mixture of a polymer base and a curing agent. The stiffness of the PDMS is determined by the base-to-curing agent ratio. We use a ratio of 10:1, ten parts of polymer base for one part of the curing agent. For the fabrication of a PDMS layer for a 2-inch template we use 10 grams of polymer base. For 3-inch wafers we use 23 grams. We mix the components thoroughly in a clean recipient. To evacuate the small bubbles that are formed during mixing we degas the liquid PDMS by placing it under vacuum until all bubbles have disappeared. The template is put in a Petri dish and the degassed PDMS is poured over it. Typical thickness of the PDMS-layer is $\delta = 5$ mm. The PDMS is cured in an oven at 65 °C for one hour. After curing, the solid PDMS is peeled off the template. We use Scotch-tape to protect the PDMS surface from getting dirty.

We now pierce holes in the PDMS at the position of the inlets and outlets, with a needle, of diameter $\delta = 1.97$ mm. The sharp end of the needle has been flattened, to create an object that pierces instead of cutting. The holes created in this way are slightly smaller than the needle diameter, because of the flexibility of the PDMS, and also slightly smaller than the outer diameter of our tubes (PTFE microtubes with $I.D. = 0.81$ mm and $O.D. = 1.63$ mm). This ensures a tight fit able to withstand pressures of several bars. This method requires fairly thick (several millimeters) PDMS surfaces that can cause problems for visualisation with objectives with a short focal distance. Furthermore piercing introduces small PDMS lumps that can enter the system and in some cases even clog channels. An alternative, but somewhat more laborious strategy consists of drilling holes in the glass [65]. To prevent the PDMS-lumps from entering the vital parts of the system we have developped filters. Their design and use will be discussed in 2.1.3.

Sealing PDMS

The PDMS imprint is a negative relief structure. To create channels it has to be sealed against another surface, that will form the fourth channel wall. We seal against a glass surface and in some cases another layer of PDMS. We have tried sealing with an ozone cleaner and with a plasma treatment. We will discuss both methods.

Ozone cleaner Our home-built ozone cleaner consists of a chamber, with a UV-lamp, connected to an oxygen bottle. Under the influence of UV, ozone (O_3) is formed. Ozone is an oxidant that can react with PDMS and glass surfaces. After putting the samples in the chamber, we fill with oxygen and expose to UV for 5 minutes. We bring the surfaces in contact immediately afterwards. Results are very unpredictable. Excellent sealing is possible, but does not occur very often. We suspect air humidity to play an important role in improving the sealing. We thus prefer the, more reliable, plasma treatment.

Plasma cleaner The central element of our plasma cleaner (Harrick Plasma) is a reaction chamber in which we place the surfaces we want to treat. With a vacuum pump we create a low pressure environment in the chamber. An oscillating electromagnetic field of radio frequency (RF) $f = 8 - 12$ MHz ionises the air remaining in the chamber. We use an air plasma and not a pure oxygen plasma.

PDMS contains repeated units of -O-Si(CH_3). The highly reactive oxygen ions in the air plasma are thought to create silanol groups (Si-OH) at the expense of methyl groups (SiCH_3) at the PDMS-surface. If this surface is brought into contact with a glass surface Si-O-Si bonds will form [44]. These covalent bonds form a tight irreversible seal.

We treat our surfaces for 40 s at pressures $P \approx 0.2$ mbar and bring them in contact immediately afterward. We have varied the exposure time. 40 s seems to be the optimum. We believe that at shorter times less Si-OH groups are created. Longer times possibly charge the surfaces electrically thereby making them repellent. Our plasma cleaner has three possible RF intensities: low, medium and high. Best results were obtained at the lowest RF level.

After sealing we wait for at least 12 hours before using the channels, because of the slow reaction kinetics involved. If both the PDMS and the glass surface are sufficiently clean, the sealing is usually successful. When, after sealing, we doubt about the success, we bake the sample for at least one hour at 95 °C, to improve the sealing.

Sealing PDMS to PDMS shows lower success rates. To achieve proper bonding the RF level should again be set to low.

2.1.3 Filters

A recurrent problem, during the experiments, consisted of the clogging of the channels, due to small PDMS particles created while piercing the holes for the gas and liquid inlet. The particles get stuck in that part of the channel system that has the smallest section, usually the orifice, where they can either perturb the flow, or completeley block the channel. In some cases the lumps can be removed by increasing the flow in the channel, or by reversing the flow direction. In other cases the clogging is permanent.

To prevent this clogging problem we developped on-chip filters, placed just after the liquid and gas inlet. The filter consists of five rows of pillars (Fig. 2.2a). The interdistance between the pillars in a row is equal to the smallest lengthscale further downstream. Assuming spherical particles, this means that those particles that are potentially big enough to block the portion of the channel under study, will not be able to enter.

During start-up of the filter-equipped system, it often occurs that the gas filter is partially filled with liquid (Fig. 2.2b). This can lead to pinching of the gas thread, both in the filter and in the orifice. This interaction creates unstable bubbling. To remove the liquid from the gas filter we strongly increase the gas pressure to above the point at which a transition from bubbling to a continuous stratified gas-liquid flow in the outlet channel takes place. The gas flow rate now becomes high enough to evacuate the remaining liquid from the filter. A subsequent decrease of the gas pressure, to below the bubbling-stratified transition, will now lead to stable bubbling, with a continuous gas flow in the filter system and bubble formation only in the orifice. The gas pressure at which this transition takes place depends on the liquid flow rate. It increases for increasing liquid flow rate. Its value can be found, for one specific geometry, in the phase diagram presented in section 4.2.4.

2.1.4 Soft lithography: discussion and outlook

The most important advantage of soft lithography is the very short time between an idea and a working system. This allows fast iterations to improve the design, but also the possibility to investigate systematically the interplay between geometry and flow. Typically 2 to 3 days of work are needed to draw the mask, make the template and generate an imprint in PDMS.

Lithography also has its restrictions. First, channels can only be rectangular. For axisymmetric systems (round channels), either glass micro-capillaries or optical fibers are used [63, 43, 59]. Their assembly, especially the aligning, is a bit troublesome though. Second, the channel system will be planar. It is possible however to make more complex systems by using multiple layers of PDMS. A well-known example consists of the pneumatic valves in [62] where two layers of channels are superposed.

(a)

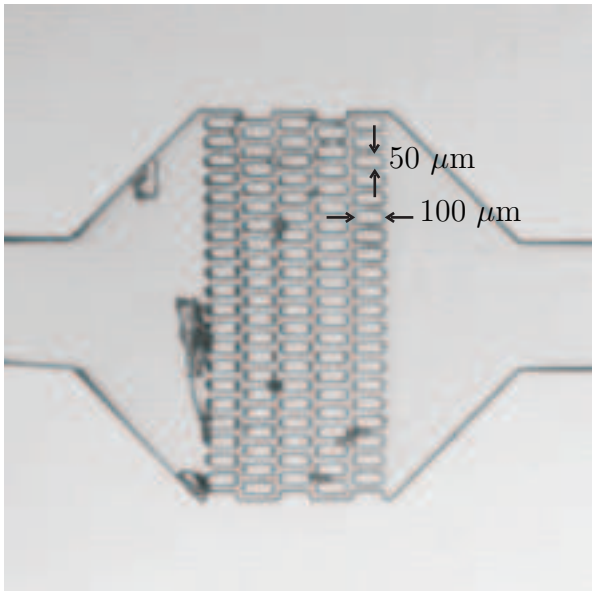

(b)

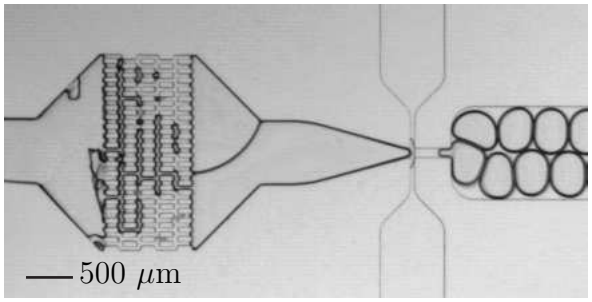

Figure 2.2: Filter for the gas and liquid flows. (a) A filter consisting of five consecutive rows of pillars. Pillar dimensions are 50×100 μm^2 with 50 μm spacing in channels with height $h = 50$ or 100 μm. One can see several PDMS lumps stopped by the filter. (b) Gas filter partially filled with liquid.

(a) (b)

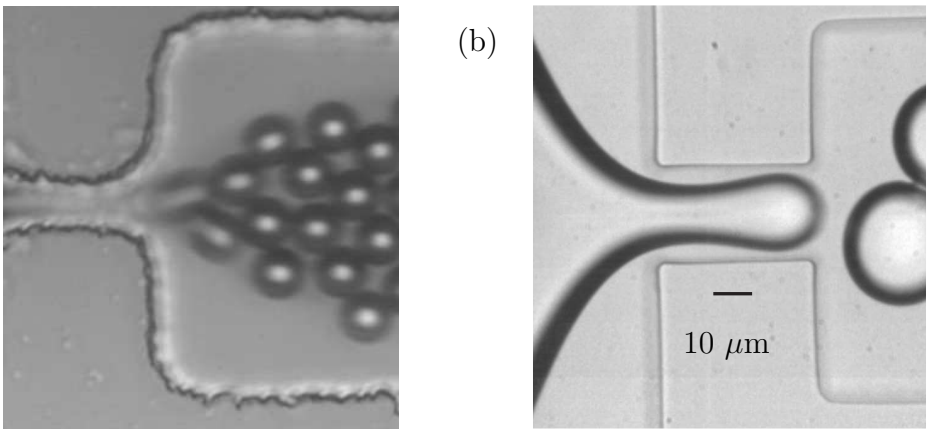

Figure 2.3: Effect of mask type. The same resin and production protocol were applied for (a) and (b). (a) is produced with a transparancy sheet mask, (b) with a chromium mask [65]. Wall roughness is much smaller for (b). Images are at the same scale.

Mask quality plays a primordial role in the template fabrication, as is shown on the pictures in Fig. 2.3. Our transparency sheets are cheap and fast to obtain. With a typical pixel size of 5 μm, walls will show a comparable roughness. Channel dimensions cannot be smaller than 20 μm, and angles cannot be too sharp. For smaller dimensions and flatter walls chromium masks need to be used. Their big disadvantage is their cost: about a factor 100 more than for transparency prints that only cost around 5 euros per A3 page.

2.2 Experimental setup

We realise our experiments in a planar flow-focusing geometry like the one first shown in [2] (see Fig. 2.4a). In total we use fourteen different geometries, all specified in Appendix A. The geometrical parameters for our standard geometry (A.1) are: channel height $h = 250$ μm, orifice width $w_{or} = 100$ μm (tall orifice), orifice length $l_{or} = 400$ μm, outlet channel width $w = 700$ μm and outlet channel length $l = 16$ mm. It will systematically be stated if we use another geometry than the one specified here.

Two distinct sections can be identified in our system: the bubble generator (I to III in Fig. 2.4a) and the flow channel (IV). The influence of size and shape of the bubble generator on foam formation is discussed in section 3.4. We have also varied the shape of the flow channel. We will discuss the influence of channel width (3.4), channel length (4.3.1), and bifurcations (5.1).

In contrast to macroscopic foam flow setups like the one described in [17] foam flow and generation cannot be dissociated in the current setup. In all our

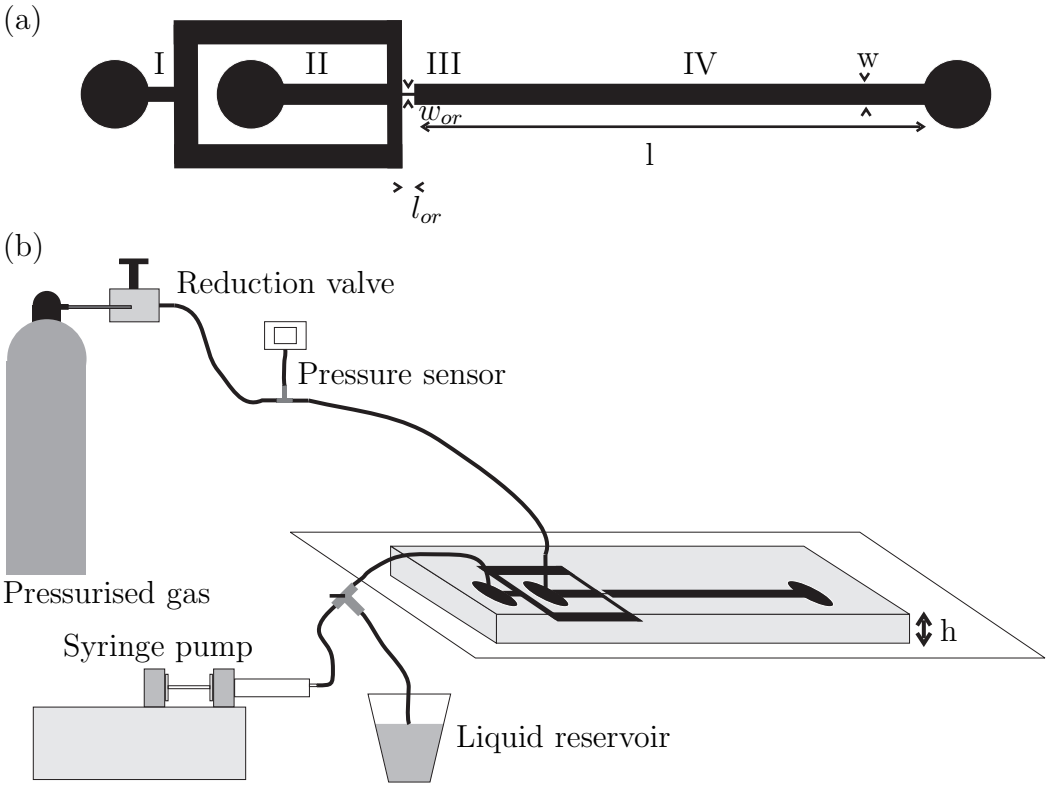

Figure 2.4: Experimental set-up. (a) Schematical outline of our microfluidic foam generator: (I) an inlet channel for the liquid, (II) another one for the gas, both ending in an orifice (III) and the outlet channel (IV). (b) Setup with pressure control for the gas and flow rate control for the liquid. The liquid reservoir allows for refilling of the syringe pump, in between experiments, without detaching any tubes, using the three-way valve. Drawing is not to scale. See text for the dimensions.

experiments bubble generation and foam flow are coupled. This coupling can lead to a retroaction of the flow on the generation. We will present an example in section 4.2. Decoupling of formation and flow can be advantageous for certain experiments. It would allow to vary foam speed for a fixed foam liquid fraction and bubble size. So far, this decoupling has not been reported. It would consist of two steps: a first step in which the foam is generated and stored in a buffer and a second in which it is pushed by some external means.

2.2.1 Control parameters

In principle, the system has two pairs of control parameters. For both the liquid and the gas, we can either impose pressure or flow rate. However, we always used flow rate control for the liquid. For the gas, in general, we fixed the pressure and measured the flow rate. We also tried fixing the gas flow rate. This has the advantage that the laborious measurement of the gas flow rate by image analysis becomes unnecessary. But as we will discuss this method shows other drawbacks.

Liquid flow rate

We impose the liquid flow rate Q_l with a syringe pump (11 Pico Plus Harvard Apparatus and KDS 100, KD Scientific). In our experiments, the flow rate is varied between $Q_l = 2$ and 200 μl/min. For the connection between the syringe pump and the channel system we use semi-rigid Teflon tubes with an internal diameter $id = 0.8$ mm. We have used also Tygon R-3603 tubes with the same internal diameter. These tubes are more flexible, thereby increasing the transition time between turning on of the syringe pump, or a change in the gas pressure, and the onset of a stable flow [58]. This is incovenient as it leads to an increase in the time needed for an experiment. The presence of bubbles in the inlet tube also leads to longer transition times, and should therefore be avoided.

Gas pressure

Gas is supplied from a pressurized bottle. A pressure reduction valve (Brooks Instruments, 8601/D6C111) (stability ± 0.15 kPa) allows to set the overpressure P_g (relative to atmospheric pressure) continuously between 0 and 70 kPa. Pressure is measured at the entrance of the device with a piezo-resistive gauge (40PC Honeywell, ± 0.2 kPa accuracy). Since the exit is at atmospheric pressure $P_{out} = 100$ kPa, the overpressure P_g is the total gas pressure drop P_{in} - P_{out} over the gas inlet tube, gas inlet channel, orifice and outlet channel. As we will show below, the pressure drop over the inlet tube and channel are negligible compared to the drop over the orifice and outlet channel. Therefore we take the measured overpressure P_g to be just the pressure drop over the orifice and the outlet channel.

We will calculate the pressure drop over the gas inlet tube and inlet channel and compare these values with the total pressure drop. We take the following typical values for the control parameters: $Q_l = 4$ μl/min and $P_g = 4.9$ kPa. We measure the gas flow rate Q_g to be 78 μl/min $= 1.3 \times 10^{-9}$ m^3/s (see section 2.2.4 for a discussion of the measurement method). Assuming the Poiseuille equation for viscous flow in a pipe:

$$\Delta P = \frac{128 \mu L}{\pi d^4} Q_g, \tag{2.1}$$

with the gas viscosity $\mu = 1.78 * 10^{-5}$ Ns/m^2 (N_2 at 27 °C), the tube length $L = 20$ cm and diameter $d = 0.8$ mm we find a pressure drop over the inlet tube of $\Delta P_{tube} = 0.46$ Pa. We can do the same for the on-chip gas inlet channel with the following approximative equation containing an error of about 10% [57]:

$$\Delta P = \left(1 - \frac{6(2^5)}{\pi^5} \frac{h}{w}\right)^{-1} \frac{12 \mu L}{w h^3} Q_g, \tag{2.2}$$

with $h < w$. We find a pressure drop $\Delta P = 0.74$ Pa for a channel height $h = 100$ μm, width $w = 700$ μm and length $l = 1.7$ mm. So the total pressure drop for the gas inlet $\Delta P_{inlet} = 0.46 + 0.74 = 1.20$ Pa. So $\Delta P_{inlet} \ll P_g$, thereby validating our assumption that P_g is essentially the pressure drop over the orifice and the outlet channel.

The gas flow rate Q_g is measured using image analysis. Details will be specified in section 2.2.4.

Gas flow rate

Instead of controlling the gas pressure, we can also control the flow rate using a syringe pump (see Fig. 2.5). The advantage of this method is that the experimental values for the gas pressure and flow rate are easy to obtain. Flow rate Q_g is the control parameter and P_g is easily measured with the pressure sensor. It avoids the image analysis necessary to obtain Q_g in the opposite case of pressure control.

A drawback of this method are the very long transients (typically up to several minutes) before reaching stable bubbling. These transients are related to the pressure build-up. If the gas in the syringe is at atmospheric pressure initially it will have to be compressed (typically a few percent), at the same time gas will start flowing out through the channel, slowing down the process. Another reason is the interplay between the syringe pump for the gas and the one for the liquid. The syringe pump for the liquid maintains a constant liquid flow rate by adapting the liquid pressure. So during pressure build-up in the gas, also the pressure in the liquid will rise. This in turn will demand a gas pressure increase which is slow due to gas compressibility.

Another issue is related to bubble formation. For a given set of control parameters the flow rate or the pressure controlled case do not always give the same

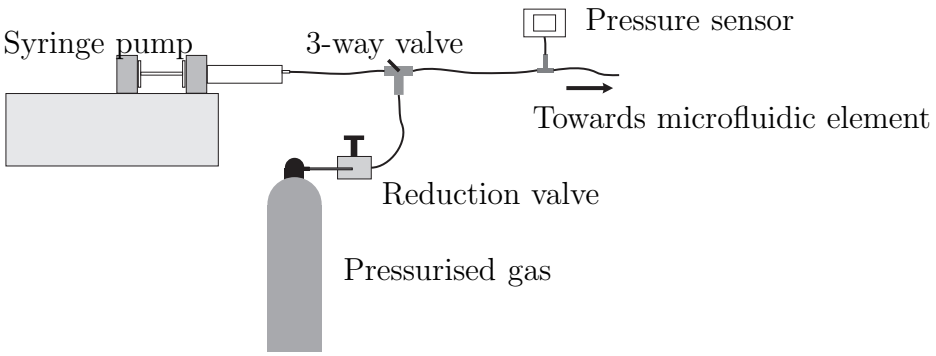

Figure 2.5: Gas flow rate control system. Gas is pushed using a syringe pump. In between experiments the syringe can be re-filled from the pressurised gas bottle, by changing the position of the 3-way valve.

result. Flow rate control leads to a preference for a bubble formation regime in which bi-disperse bubbles are formed instead of a mono disperse foam (data not shown).

The inconveniences stated above have made that we prefer to control pressure instead of flow rate for the gas. So, unless specifically stated otherwise, our system has one pair of control parameters consisting of the liquid flow rate Q_l and the gas pressure P_g.

2.2.2 Visualisation

To visualise our experiments we use a digital camera (Marlin F-131B, Allied Vision Technologies). Its frame rate f_c depends on image size and shutter time and hence on the available amount of light. With minimum shutter and images with a resolution of 1280×1024 pixel^2, a frame rate of $f_c = 25$ fps can be reached. This increases to $f_c = 94$ fps for a 640×512 pixel^2 image and up to 888 Hz for 320×40 pixel^2, which is the minimum pixel size we need. The image stack is stored as a series of bitmap files, allowing for subsequent image processing.

Close up: microscope

The usual way for imaging a microfluidic element is by connecting the camera to a microscope. We use an inverted microscope (IX 70, Olympus) with 4× objective. See Fig. 2.6a for an example of the pictures taken with this method. This combination of microscope and camera allows a field of view with a maximum size of 2.1×1.7 mm^2. This allows for close ups on a specific part of the setup, for example on the orifice, but capturing the whole system is not possible.

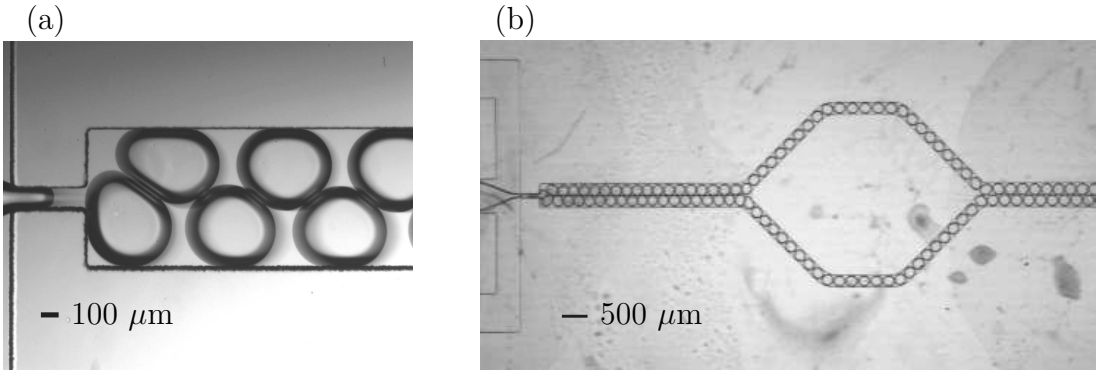

Figure 2.6: Typical images obtained by connecting the camera to (a) a microscope with 4× magnification lens, (b) a macro lens.

Overview: macro lens

If we want to follow the flow in the entire channel system, we use the setup shown in Fig. 2.7. The camera is connected to a 50 mm macro lens. The field of view can be adapted by changing the distance between the camera and the channel system, to adapt for channel systems with different overal dimensions. In general we work with a field of view of a few cm^2.

Illumination is a very important issue for our experiments. First it should be sufficiently intense to work at small camera shutter times, allowing for high image frame rates. Second, it should be continuous, thereby excluding fluorescent tubes. Third, it should be homogeneous so that images are suitable for digital analysis. The option we choose is a matrix of 6×10 LEDs. The light is sufficiently intense and constant. A diffusing plexiglas plate, placed between the LEDs and the microfluidic element, homogenises the light intensity. Fig. 2.6b shows an image acquired with this setup.

2.2.3 Gas, liquid, surfactant

Continuous phase

For the continuous phase we use deionised water with 10 % commercial dish-washing detergent (Dreft, Procter & Gamble). Dreft contains mainly anionic surfactants and the solution is far above the cmc. The use of deionised water is supposed to increase foam stability. It leads to the absence of cations, that could possibly screen the electrostatic repulsion between the two surfactant layers in a water film between bubbles. But at our very high surfactant concentration, this is probably only a very minor effect.

The surfactant ensures the stability of the liquid film, but it probably also plays a role in changing the surface properties of the PDMS. The PDMS in its

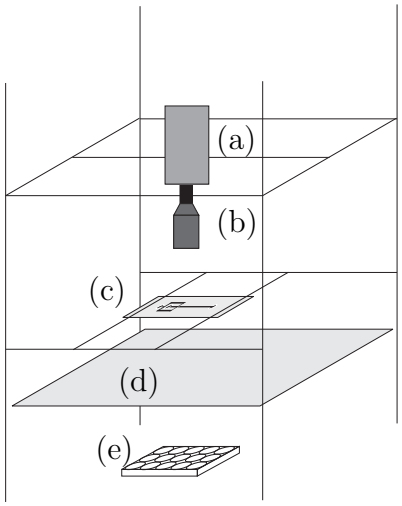

Figure 2.7: Setup allowing visualisation of the entire microfluidic element. (a) camera, (b) macro lens, (c) microfluidic element, (d) diffusing plate, (e) 6×10 LEDs.

natural state is hydrophobic. After a plasma treatment, like the one we use for sealing, the PDMS becomes hydrophilic. This effect however is not permanent. If the channels are not immediately filled with water, the PDMS will become hydrophobic in about 45 min [20]. The surface properties of PDMS are very important in a two-phase flow like the one we study, because the phase that wets the most the channel walls will be the continuous phase. This effect has been used in a very ingenious way in [3] to make double emulsions. The systems consists of two T-junctions placed in parallel. The channel walls around the first junction are untreated and therefore hydrophobic. So when oil and water flows meet at this junction, the oil will wet the channel walls and water in oil (W/O) drops are formed. The walls around the second junction are coated with a polymer rendering these hydrophilic. Now, when the initial (W/O) emulsion encounters a water flow at this junction a further encapsulation takes places. A water-in oil-in water emulsion is created. This example stresses the importance of fluid wettability in a two-phase flow.

In our case the PDMS walls are probably hydrophobic. The plasma treatment is temporary [20], and we do not fill the channels immediately with water after sealing. So the gas is supposed to preferentially wet the walls. Still we make foams in which the gas bubbles are covered by a continuous liquid film touching the walls. We suppose that the surfactant plays a role in all this. Probably a similar mechanism takes place as the one described in [41], in which a monolayer of surfactant covers the channel walls, thereby rendering them hydrophylic.

The water-Dreft solution has a surface tension $\sigma = 38 \pm 1$ mN/m, as measured by the Wilhelmy balance method, and a viscosity $\mu = 1.35\ 10^{-3}$ Pa.s.

Dispersed phase

We use nitrogen for the dispersed phase. The use of nitrogen compared to normal air leads to more stable foams. It is less soluble in water than air and therefore coarsening is limited. With the exception of the compressible foams discussed in section 4.3.1, nitrogen solubility does not play a role in our system. Residence times of the gas bubbles in the channel are small enough (typically around $t = 0.5$ s) not to see a bubble volume change during transit of a bubble from the orifice to the outlet. Coarsening however can be an important issue in microfluidics, especially for small channel heights. Because of the small length scales involved, the capillary pressure can become very high (for example, $P_c = 15$ kPa, for a spherical bubble in a channel with $h = 10$ μm), thereby driving gas transport from the bubble to the surrounding liquid. In these cases the use of a poorly soluble gas like SF_6 could be recommended.

2.2.4 Measurable quantities

With the exception of the control parameters P_g and Q_l, image analysis is used to extract all quantitative information from our experiments. We use the versatile open source program ImageJ to process our images (http://rsb.info.nih.gov/ij/). ImageJ supports the use of macros to automatise the image analysis. The amount of data in our experiments however was not consistent enough to justify the time-intensive development of these macros. So we usually proceeded with a manual approach. We can extract the following quantities: the bubble formation frequency f_b, the bubble apparent area A_b and volume V_b, the gas flow rate Q_g, the foam topology, the volume liquid fraction Φ_l and the injected liquid fraction α_l.

Bubble formation frequency

We measure the bubble formation frequency simply by counting the number of bubble creation events N_b in an image stack containing N_f images. This can be related, together with the camera frame rate f_c, to the formation frequency:

$$f_b = \frac{N_b}{N_f} f_c. \tag{2.3}$$

The accuracy of this measurement is typically in the order of 2 frames, leading to a relative accuracy $\frac{2}{N_f} \leq 1\%$, for typical values of N_f between 200 and 1000 frames.

Bubble apparent area and volume

To calculate the bubble area and volume we use two different methods depending on the foam liquid fraction. We will distinguish between a wet (Fig. 2.8a) and a

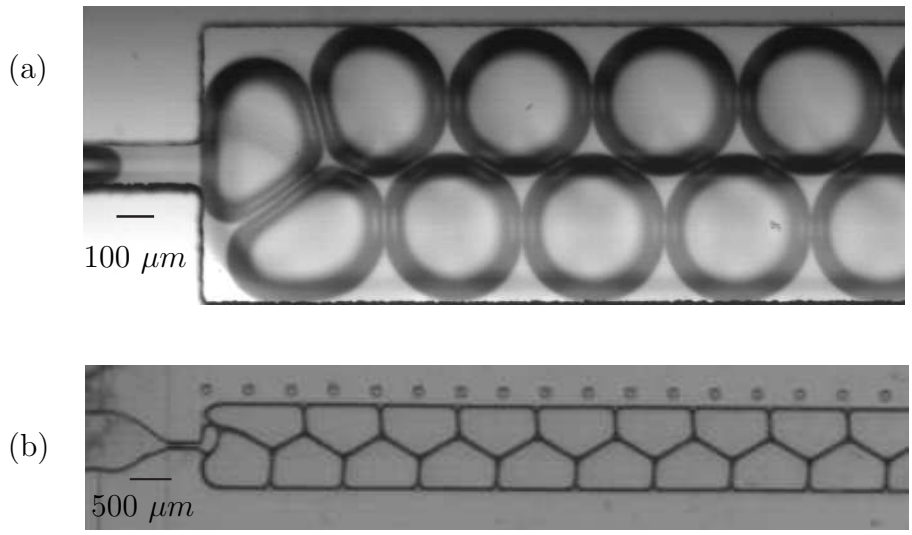

Figure 2.8: Two different cases for bubble area and volume determination. (a) Wet 2-row (F2) foam. Curved gas-liquid interfaces appear dark. (b) Dry 2-row foam. The liquid is mostly confined to the Plateau-borders appearing dark in the image.

dry case (Fig. 2.8b).

Wet foams Our channels are much larger than that they are high. Therefore bubbles are squeezed, deformed into quasi-cylinders with a flat top and bottom interface and curved sidewalls. This situation is sketched in Fig. 2.9a.

In a zero order estimate we could measure the apparent area A_b, and calculate V_b by multiplying with the channel height h:

$$V_b = A_b h. \tag{2.4}$$

The first correction is that the real height will be somewhat, but negligibly (< 1 μm) smaller than the channel height h. The second is in the contribution of the curved sidewalls (with radius $r \approx h/2$, see Fig. 2.9b) to the volume. Related to this is the question of where the flat interface stops and the curved sidewalls start. Bubbles appear in our images as light domains with dark edges (see *e.g.* Fig. 2.8a). These intensity differences are due to refractive effects. The light source is positioned below the channel system and the camera above. Therefore certain light rays will refract on the gas-liquid interface and not be able to reach the camera. We assume the curved walls to appear dark and the flat parts to appear light. This is a simplified picture, as has been shown in [64], but we suppose the error to be small. A more thorough analysis would be more laborious than can be justified for our purposes.

We take the edge of the measured area A_b in the middle of the curved interface

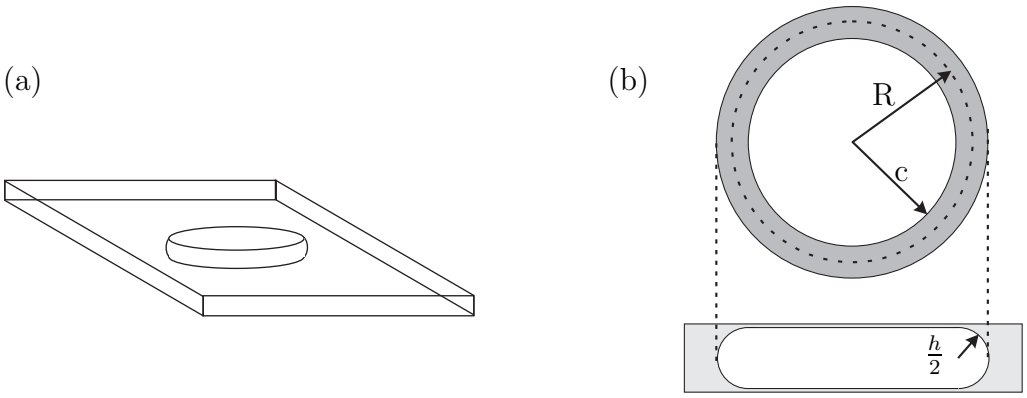

Figure 2.9: (a) Sketch of a bubble squeezed into a disk-like shape by the channel walls. (b) Top- and side view. The dark gray region indicates a curved interface. R is the radius used to calculate the apparent area A_b.

appearing black on images. In this way our measurement is more precise than in the case of just using the light area and quicker than an exact measurement. This method introduces a systematic error in the measurement of the actual gas volume that decreases with bubble size. It can be calculated analytically for the case of non-touching, so non-deformed bubbles. The volume of our squeezed cylinders equals:

$$V_b = \pi c^2 h + \frac{\pi^2}{4} c h^2 + \frac{\pi}{6} h^3. \tag{2.5}$$

This equation is obtained by summing the contribution for the volume of a cylinder with radius c and height h, with the one for the external half of a torus. See Fig. 2.9b for a definition of the symbols. Our approximation yields in this case:

$$V_{b,approx} = h\pi R^2 = \pi c^2 h + \frac{\pi}{2} c h^2 + \frac{\pi}{16} h^3. \tag{2.6}$$

Thus for the relative error e we can write:

$$e = \frac{|V_b - V_{b,approx}|}{V_b} = \frac{ch(\frac{\pi}{4} - \frac{1}{2}) + \frac{5}{48}h^2}{c^2 + \frac{\pi}{4}ch + \frac{h^2}{6}}, \tag{2.7}$$

which is in the order of 10% for small non-touching bubbles, and rapidly decreasing with c for larger ones.

Dry foams For these foams we first apply an image pre-treatment. We subsequently apply the ImageJ routines Threshold and Skeletonize (Fig. 2.10a and b). These result in a black and white image in which the borders between bubbles are one pixel thick. ImageJ can now extract the bubble area A_b. The volume V_b is again calculated by multiplying with the channel height h.

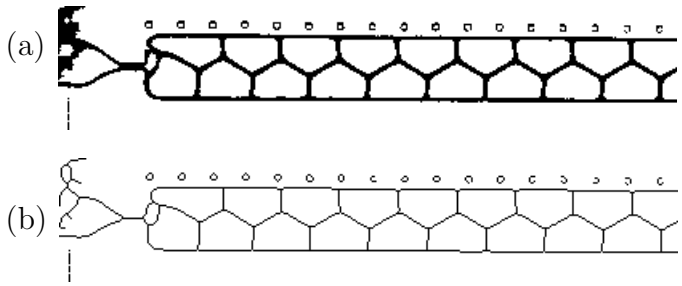

Figure 2.10: Pre-treatment of the image in Fig.2.8b. (a) Thresholding. (b) Skeletonization

This method essentially neglects the volume occupied by the liquid, thereby introducing a systematic error depending on the liquid fraction. The gas flow rate is typically about 5% overestimated.

Gas flow rate

In the general case, for which we control the gas pressure P_g, we measure the gas flow rate Q_g by multiplying the bubble formation frequency f with the bubble volume V_b:

$$Q_g = fV_b \tag{2.8}$$

Topology

We classify the foam topology by counting the number N of bubble rows that fit in the channel width. We name the different topologies F1, F2 .. FN, where F stands for foam. For F1 and F2 we also use the terms bamboo and alternate foam. We call a flow in which bubbles do not touch each other, a bubbly flow. A sketch of the different topologies is given in Fig. 2.11.

N is easily determined by visual inspection of the images.

Liquid fraction

An important parameter in characterizing a foam is the foam volume liquid fraction Φ_l, *i.e.* the proportion of the volume occupied by the liquid:

$$\Phi_l = \frac{V_l}{V_{total}} = \frac{V_l}{V_g + V_l}. \tag{2.9}$$

For fairly high liquid fractions ($\Phi_l > 0.2$), it can be estimated by image analysis as:

$$\Phi_l \simeq 1 - A_b/A. \tag{2.10}$$

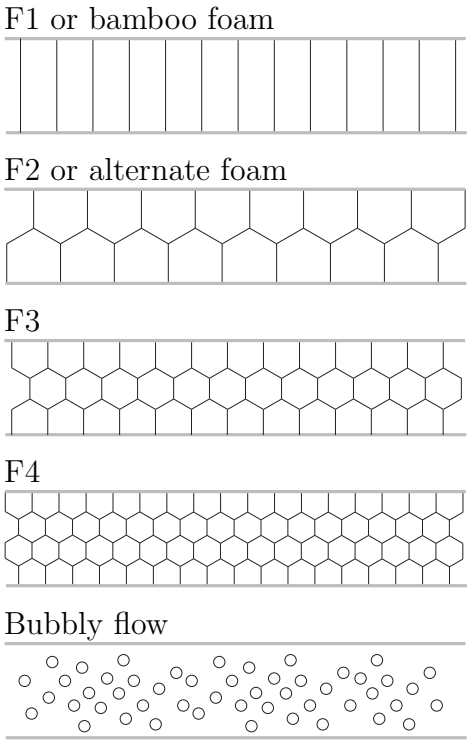

Figure 2.11: Schematical drawing of the different topologies and their nomenclature.

Another method is to measure simultaneously the time and space averaged bubble velocity $\langle\overline{u_g}\rangle$ together with the average gas flow rate; the liquid fraction then follows from $Q_g = \langle\overline{u_g}\rangle S(1-\Phi_l)$, with S the area of the channel cross section:

$$\Phi_l = 1 - \frac{Q_g}{\langle\overline{u_g}\rangle S}. \tag{2.11}$$

On the other hand, the proportion of liquid *injected* in the system is

$$\alpha_l = \frac{Q_l}{Q_g + Q_l}, \tag{2.12}$$

with $Q = Q_g + Q_l$ the total two-phase flow. It is simply measured as Q_l is one of the control parameters. The precision in this measurement is better than $\pm 10\%$ for non-touching bubbles and in general a few percent.

The two quantities Φ_l and α_l are different because liquid and gas can have different velocities. They can be linked using the time and space averaged gas and liquid velocities $\langle\overline{u_g}\rangle$ and $\langle\overline{u_l}\rangle$ since $Q_l = \langle\overline{u_l}\rangle S\Phi_l$ and $Q_g = \langle\overline{u_g}\rangle S(1-\Phi_l)$. This yields:

$$\frac{\langle\overline{u_l}\rangle}{\langle\overline{u_g}\rangle} = \frac{\alpha_l}{1-\alpha_l}\frac{1-\Phi_l}{\Phi_l}. \tag{2.13}$$

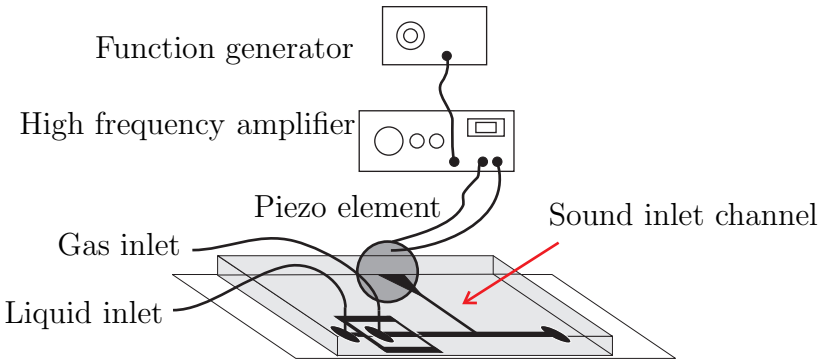

Figure 2.12: Ultrasound setup

The separate measurement of α_l and ϕ_l allows to calculate the ratio $\langle\overline{u_l}\rangle/\langle\overline{u_g}\rangle$ which informs about the relative drainage of liquid through the moving foam. The absence of relative drainage, $\langle\overline{u_l}\rangle/\langle\overline{u_g}\rangle = 1$, implies that $\alpha_l = \Phi_l$, while drainage in the direction of the flow, $\langle\overline{u_l}\rangle/\langle\overline{u_g}\rangle > 1$, corresponds to an injected liquid fraction higher than the volume liquid fraction $\alpha_l > \Phi_l$.

2.2.5 Ultrasound

To study the interaction between ultrasound (pressure waves with a frequency $f_s > 20$ kHz, so above the audible range) and a microfoam, we developped the setup shown in Fig. 2.12. We generate the ultrasound using a ceramic piezo-element (PIC151, PI). The signal for the piezo is generated with a function generator (5200, Krohn-Hite) coupled to a wideband power amplifier (DC to 1 MHz, 7600M, Krohn-Hite). The channel system contains, in addition to the elements already presented, a channel, which we name "sound inlet channel", connecting the piezo to the microfoam. This channel is in direct contact with the piezo. The piezo itself is glued to the glass and PDMS.

2.3 Outlook: 3D-imaging

The images we obtain with our setup are a 2D projection of a 3D situation. The final picture is a superposition of the information in the z-direction. This makes it hard to reconstruct the actual repartition of the volume occupied by the liquid and the gas. This is important however, for the determination of the liquid fraction, to study drainage. Also for the study of dissipation in a foam flow exact knowledge of the foam structure is very valuable. Therefore a 3D-imaging method would be advantageous.

2.3.1 Two-photon microscopy

To explore the possibilities for 3D-imaging we used Jean-Claude Vial's home-made two-photon microscope, in our lab. We performed preliminary experiments. In the following we will discuss the method, our first results and possible ways to improve these.

Two-photon microscopy is an imaging technique in which a sample is illuminated, and its image recorded, one point at a time. The point illumination is created by focalizing a light source. A scan over the x-, y- and z-direction creates a series of image points, allowing to reconstruct the complete 3D-image. Usually fluorescence microscopy is used, because it allows for the imaging of only a specific part of the sample, namely the one containing the fluorescent dye molecules.

In confocal microscopy, a pinhole eliminates all the light not coming from the focal plane. Here, to get rid off the light coming from other points than the focal point, the fluorescent dye (fluorescein) is illuminated by light at twice the excitation wavelength. These photons therefore contain only half the necessary energy, so that two photons are needed to generate emission of fluorescent light. To excite the dye molecule, the two photons have to be absorbed quasi-simultaneously. The probability of photon absorption is quadratic in the light intensity. In this method only light at the focal point is sufficiently intense to excite fluorescent light. This method is particularly useful in diffusive media (there is much less background noise due to scattering than in confocal microscopy) and in samples where high-energy one photon excitation could cause damage.

The maximum resolution of the resulting reconstructed 3D image depends on the dimensions of the image elements (voxels). Voxel size corresponds to the size of the volume around the focal point of the illumination beam in which the light intensity is sufficiently high to excite the fluorescent molecules. In our setup this corresponds to a voxel with dimensions $2 \times 0.5 \times 0.5$ μm^3.

The size of the total volume that can be imaged depends on the microscope properties. In JC Vial's setup a mirror system deflecting the light bundle allows for scanning in the xy-plane. In combination with a 20$\times$ magnification objective, a field with a size of 600×600 μm^2 can be scanned with a resolution of 512×512 pixel^2 and an acquisition time of 1 s. The lateral position of the microscope objective is controlled electro-mechanically. In this way the depth of view can be modified automatically and image stacks with a fixed step size between consecutive images can be acquired. Step size was set to 3 μm. Thus in slightly more than 1 min we can image a volume with dimensions $600 \times 600\times 200$ μm^3.

2.3.2 Preliminary results

The two-photon microscope setup, in its actual configuration, is not able to handle a flowing foam. Because of the slow acquisition time of 1 s per image and 1 min for the total box, we can only image a static foam. Therefore we first had to find

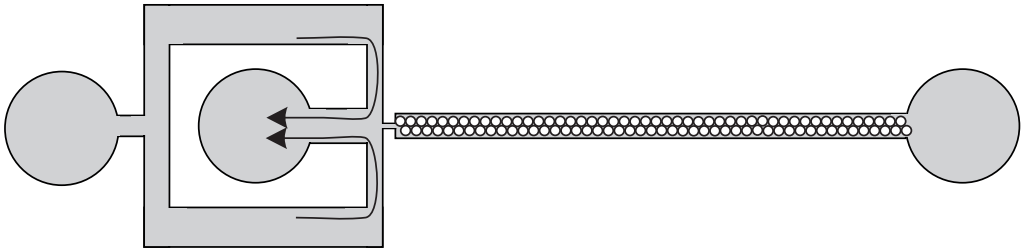

Figure 2.13: A static foam. Arrows in the drawing indicate flow direction of the liquid after the gas inlet tube has been removed.

a way to stop the foam flow while still keeping a foam in the channel. This is not easy because of the small volume of the outlet channel. First cutting the liquid flow and then the gas leads to a channel filled with only gas. Stopping the gas flow by turning the pressure gauge creates the opposite situation of a liquid filled channel.

Eventually we proceeded in the following way: in a channel with height $h = 100$ μm and width $w = 600$ μm we create a stationary foam flow with a liquid flow rate $Q_l = 35$ μl/min and a gas pressure $P_g = 9.0$ kPa. We add fluorescein to the continuous phase. To stop the flow we detach the gas inlet tube from the channel system. The liquid is still pushed by the syringe pump: it will not flow through the outlet channel, but through the gas inlet, which in the absence of a gas flow presents a lower resistance to flow than the foam-filled outlet channel, see the sketch in Fig. 2.13. Now we stop the syringe pump and place a clamp in the liquid inlet tube. Finally, this tube can be detached from the syringe pump, to enable the transport of the microfluidic chip.

The complete stack of micrographs, of which a few examples are shown in Fig. 2.14, is used to reconstruct a 3D-image with the ImageJ command 3D-project. The result can be viewed from any direction and under any angle (Fig. 2.15).

2.3.3 Discussion

Several remarks can be made about the aptitude of two-photon microscopy for the imaging of microfoams:

First, our setup's spatial resolution allows for the visualisation of the liquid in the Plateau borders. On the other hand, the thin liquid films that constitute bubble walls are not visible, neither between bubbles nor between bubbles and the channel walls (Fig. 2.15).

Second, as mentioned before, refractive effects on the gas-liquid interfaces complicate foam visualisation. Fig. 2.16 shows the liquid profile in a channel section. The actual liquid profile is symmetric, whereas the one recorded is far too narrow in the lower half. In this region, reflection and refraction seem to

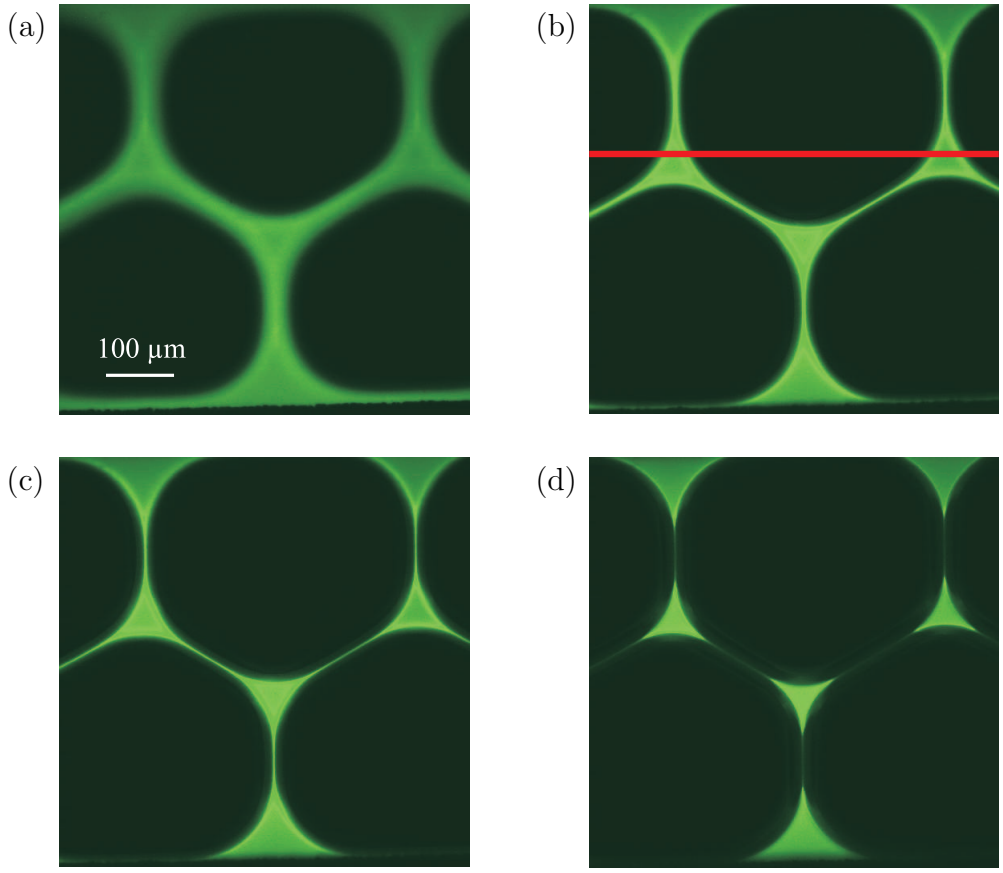

Figure 2.14: Pictures obtained with 2-photon microscopy. The liquid (continuous) phase contains fluorescent dye and appears green in the images. Consecutive images correspond to an increasing observation depth: (a) 0 μm, (b) 15 μm, (c) 30 μm and (d) 45 μm. The red line in (b) corresponds to the sidecut in Fig. 2.16.

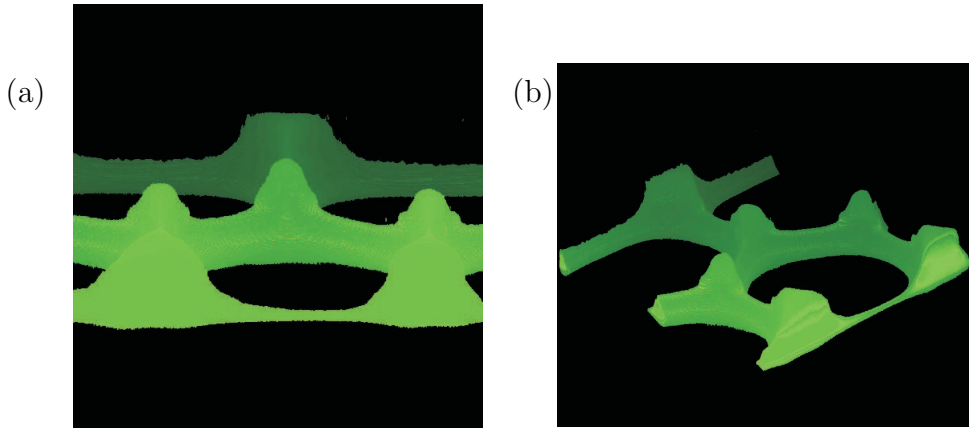

Figure 2.15: 3D-images of a microfoam, obtained with 2 photon confocal microscopy. The angle of view can be chosen at will: (a) 110 ° and (b) 120 °. For the reconstructions in (b)the original images have first been rotated 45 °.

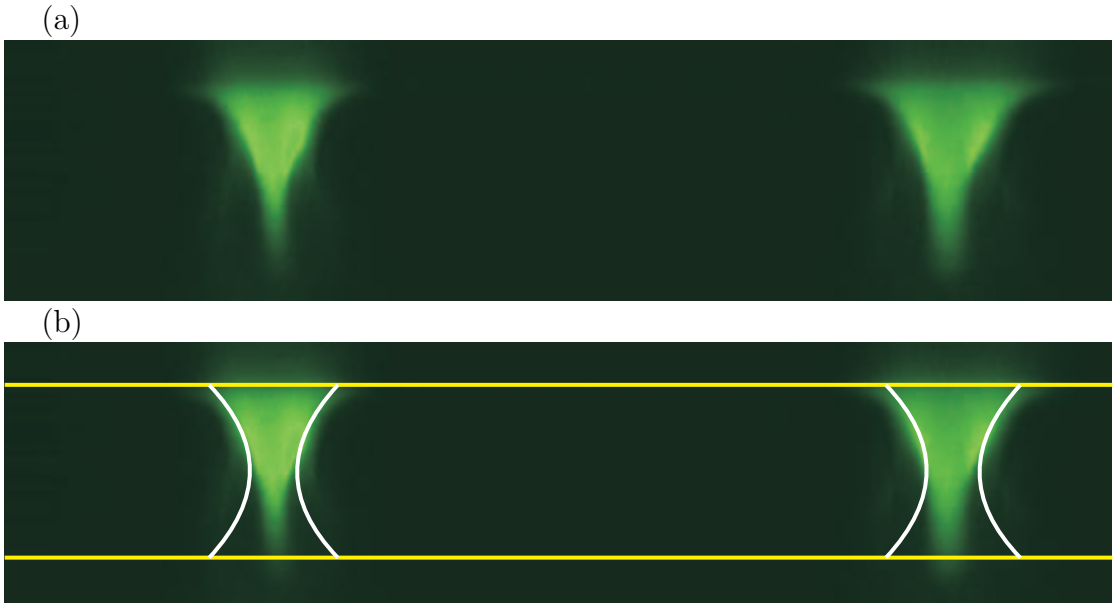

Figure 2.16: Section cut. The side view in (a) is taken along the line indicated in Fig. 2.14b. Yellow lines in (b) indicate position of the upper and lower channel walls. The approximate shape of the water-liquid interface is shown by the white lines.

obstruct the light from reaching the camera. Thus, for this experiment, only the upper half of the 2D-foam can be visualised. More or less, because the interface position is slightly altered due to the same effect. In this respect, this method might be more adapted to emulsions where optical density matching between the two phases, *e.g.* by adding glycerol to water, is possible.

Third, we visualised a static foam. It would be a big improvement, and even a necessity for the study of relative drainage, if the setup could handle flowing foams. To obtain sharp images of a typical flowing microfoam, the actual acquisition time of 1 s per frame should by decreased at least a factor 100. Another approach could take advantage of the stable period of the flow (repetitive character). The objective moves in the x-y-z space while actually the y-z plane, with y the direction parallel to the flow, would be enough. At a fixed position (y,z), the camera should record a series of points, while the foam flows by, corresponding to at least one period (the passage of one bubble). If we interprete pixels in a series as a signal with an intensity varying over time, the different series have the same period (related to the bubbling frequency) but with a phase difference. By cross-correlating these signals, the 3D-image can again be reconstructed.

Fourth, it would be interesting to do one precise experiment, for varying liquid fractions, to validate the ray-tracing approach in [64]. Thus in the future the ray-tracing technique would be enough and can be applied to flowing foams.

2.4 Résumé

Dans ce chapitre nous avons décrit l'ensemble des techniques expérimentales utilisées pour l'étude de la génération et de l'écoulement d'une micro-mousse.

Nous commençons avec une description de notre méthode de micro-fabrication : la lithographie douce (paragraphe 2.1). Cette méthode consiste en deux étapes : la fabrication d'un moule en relief, et la fabrication d'une empreinte de ce moule. Le moule consiste en une plaquette de silicium sur laquelle on a appliqué une fine couche de résine photosensible. Après application d'un masque contenant le dessin de la géométrie souhaitée, on expose la résine à la lumière UV. La partie non couverte par le masque polymérise. Pendant une étape de développement, la résine non-exposée sera enlevée, créant ainsi une structure en relief. On fait des empreintes de cette structure dans du PDMS, un polymère transparent. Pour fermer les canaux, cette couche de PDMS est collée, avec l'aide d'un traitement de plasma, contre une lame de verre.

Le paragraphe 2.2 donne les détails du dispositif expérimental. Après avoir introduit des valeurs 'standards' pour les différentes longueurs dans la géométrie des canaux nous décrivons les paramètres de contrôle de notre système : le débit de liquide Q_l, réglé avec l'aide d'une pousse-seringue, et la pression du gaz P_g. La visualisation a lieu par intermédiaire d'une camra accelerée couplée à une microscope pour des vues de détail ou à une lentille macro pour des vues d'ensemble.

Nous décrivons les composants de la mousse : de l'azote, de l'eau déionisée avec 10 % de produit vaisselle (Dreft).

Une analyse d'image nous donne accès à plusieurs grandeurs physiques. On mesure : la fréquence de formation de bulles f, l'aire apparente A_b et le volume apparent Vb et la topologie (nombre de rang de bulles). A partir de ces quantités on peut reconstituer le débit de gaz $Q_g = fV_b$ et la fraction de liquide injectée $\alpha_l = Q_l/(Q_g + Q_l)$.

Le dernier paragraphe de ce chapitre concerne une méthode de visualisation 3D : la microscopie à deux photons. A l'aide d'une source de lumière une échantillon fluorescente est illuminée et son image enregistrée point par point. La lumière envoyée a une énergie qui vaut la moitié de l'énergie nécessaire pour exciter la fluorescence. Du coup pour exciter un molécule de colorant il faut une arrivée quasi-instantanée de deux photons, ce qui est possible seulement dans le point focal. Comparé avec la microscopie confocale cette méthode présente l'avantage de créer beaucoup moins de bruit. Nous avons essayé de visualiser une micro-mousse au repos. Les résultats sont fortement influencés par le contraste d'indice optique du gaz et du liquide.

Chapter 3

Microfoam generation

In this chapter we will present our study of microfoam generation in a flow-focusing system. A foam is a collection of bubbles, therefore we study essentially the bubble formation process and its dependence on the control parameters. First we will give an overview of aspects of bubble formation in our standard channel geometry. We will discuss the different regimes of bubble formation that we encounter, the dependance of the bubble volume and formation frequency on the liquid flow rate and gas pressure. This section will serve to establish what we will refer to as the standard case of dry foam formation.

Then, we will show that this standard case of dry foam formation critically depends on confinement of the gas thread break-up to the orifice. We will show how this confinement can be influenced both by the channel geometry and by the value of the liquid flow rate Q_l. As a transition to the following chapter on microfoam flow, we will discuss the interplay between control parameters and channel geometry on the foam structure (number of bubble rows) in the outlet channel. Finally, we will compare our results with the available literature on similar systems.

3.1 High gas fraction foam formation: overview

3.1.1 Bubbling regimes

To study the different regimes of bubble formation and the accompanying bubble topology in the channel we vary the gas pressure at constant liquid flow rate for our standard channel geometry. See Fig. 3.1 for examples of the observations in this channel, near the orifice at the channel entrance for a fixed flow rate of $Q_l = 167$ μl/min. Above a certain threshold in gas pressure P_g, bubbles form in the channel. The bubble volume globally grows when increasing P_g, inducing several regimes of bubble formation and flow, which we now present briefly, before discussing them in detail in the next sections.

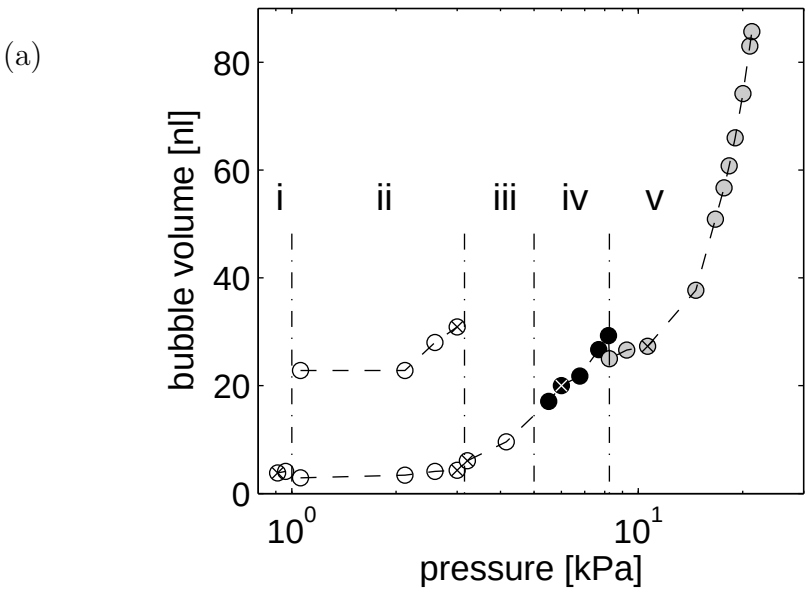

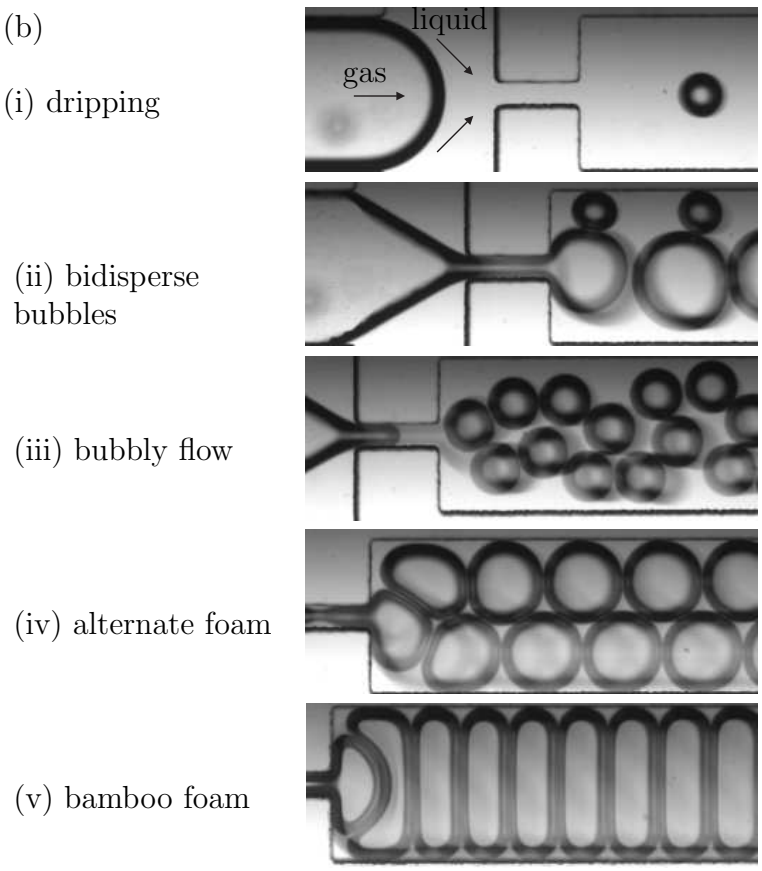

Figure 3.1: From wet to dry microfoams. (a) Bubble volume V_b versus gas pressure P_g. Liquid flow rate is kept constant at $Q_l = 167\ \mu\text{l min}^{-1}$. Numbers identify the different regimes: (i) dripping flow; (ii) bidisperse bubbles (two symbols are plotted for each pressure); (iii) bubbly flow; (iv) alternate foam (2 rows) with filled symbols; (v) bamboo foam (1 row) with gray symbols. (b) Photographs of these regimes. Crossed symbols in (a) correspond to pictures in (b).

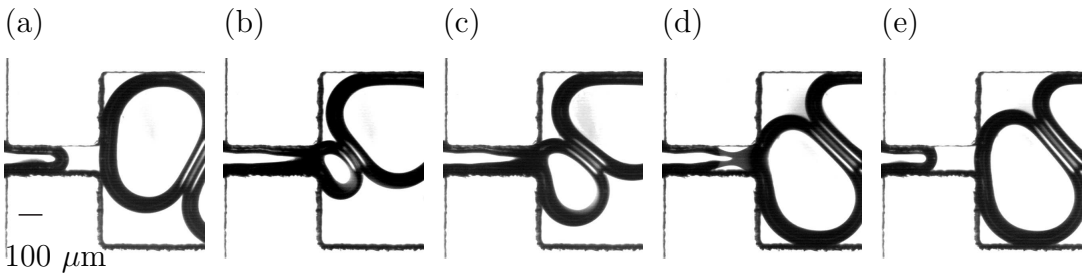

Figure 3.2: Bubble formation in a flow-focusing system. A gas thread is forced into the orifice (a) and fills a bubble after the orifice (b) and (c). The bubble blocks the access for the liquid into the channel. Therefore the liquid pinches the gas thread (d), thereby releasing a bubble in the channel (e).

We observe a minimum pressure P_c for bubble formation, below which the gas-liquid interface does not enter the orifice. At this liquid flow rate, $P_c = 0.9 \pm 0.15$ kPa (Fig. 3.1a). This effect is probably due to the capillary pressure P_σ. In fact, for a curved interface in this orifice at the limit of bubble detachment, the Laplace pressure of a wetting interface is:

$$P_\sigma = \sigma \left(\frac{1}{r_1} + \frac{1}{r_2} \right) = 1.1 \pm 0.2 \quad \text{kPa}, \tag{3.1}$$

where $r_1 = h/2$ and $r_2 = w_{or}/2$ are the principal radii of curvature. This is of the same order as the measured P_c.

Above the initial pressure P_c, a gas thread is forced into the orifice (Fig. 3.2a) and fills a bubble after the orifice (Fig. 3.2b and c). This thread pinches off (d) and releases the bubble (e). At low gas pressures P_g (but still larger than P_c), after break-up, the gas-liquid interface retracts to its initial position, as reported in [29], returning completely into the upstream part. This is the dripping flow regime (Fig. 3.1b (i) dripping).

At higher P_g, we encounter an intermediate situation in which after bubble release the interface stays in the orifice, releases a second, smaller bubble and then retracts upfront of the orifice. So in this regime, there is a coexistence, probably indicating a first-order transition, with a second mechanism, where the interface remains in the orifice instead of retracting after bubble release. For given P_g and Q_l, both mechanisms give different volumes V_1, V_2. This results in a flow of period $T_1 + T_2$ [28], with bidisperse bubbles (ii, Fig. 3.1b).

Further increasing P_g, we only observe the second pinch-off mechanism, for which the interface stays in the orifice after release of a bubble. This regime always results in monodisperse bubbles. For this channel geometry, three possible structures appear, according to the gas flow rate: bubbly flow (iii), and after a jamming transition, an alternate foam with two rows (iv), or bamboo foam with one row only (v).

We do not observe multiple-period or chaotic bubbling like the one reported in [27]. This suggests the absence of inertial non-linearities during the retraction of the gas-liquid interface in contrast to the results in [27] obtained at much higher liquid flow rates and gas pressures.

If we increase P_g even further the gas thread stops breaking up and a stratified liquid-gas flow is observed.

3.1.2 Microbubble volume

In general, bubble volume V_b increases with increasing gas pressure P_g and decreases for increasing liquid flow rate Q_l. To study this dependance on the control parameters in more detail we measure the bubble volume V_b by varying the gas pressure P_g at fixed liquid flow rate Q_l in the monodisperse bubbling regime. We repeated this for several different liquid flow rates: $Q_l = 4$, 15, 20, 30 and 40 μl min^{-1}. We find that the bubble volume correlates well with the inverse liquid fraction α^{-1}:

$$\frac{V_b}{w_{or}h_{or}^2} \sim \alpha_l^{-0.95\pm0.02}, \tag{3.2}$$

see Fig. 3.3, except for the lowest Q_l. The deviation at low liquid flow rate will be discussed in section 3.2.2. We rescale the bubble volume V_b by $w_{or}h^2$. It represents the volume, initially occupied by the gas thread (Fig. 3.2c) that is pinched off by the liquid (Fig. 3.2d and e) during bubble formation. This volume will be treated in more detail in sections 3.1.3 and 3.2.1.

At very low liquid content $\alpha_l \simeq Q_l/Q_g \ll 1$. Therefore, for dry foams, the bubble volumes are approximately proportional to (Q_g/Q_l).

When we compare this with the results reported on similar systems we find this correlation to be similar to the one observed in axisymmetric conditions by [31, 30] who measured $V_b/w_{or}^3 \sim (Q_l/Q_g)^{-1.11\pm0.02}$, *in the opposite case* of a high liquid fraction with $Q_l/Q_g > 5$, with separated bubbles, while here bubbles are in contact or in short spacing after formation. It seems to differ from the $V_b \sim P_g/Q_l$ scaling observed by Garstecki et al. [28]. We will see below that the gas flow rate and applied pressure are not proportional for our case of a low liquid fraction microfoam. So we cannot simply state $V_b \sim P_g/Q_l \sim Q_g/Q_l$, for our case. On the other hand, ref. [28] investigates high liquid fraction flows where the linear relation between the gas flow rate and applied pressure can be justified by assuming a negligeable amount of bubbles in the outlet channel (a very diluted bubbly flow and certainly not a foam flow). In that case, we both find the same scaling: $V_b \sim Q_g/Q_l$.

In this geometry, one or two rows of bubbles are observed. The jamming transition from bubbly flow to a foam in which bubbles form a connected network is governed by the volume liquid fraction Φ_l, which is related to α_l through equation 2.13. Therefore increasing the number of bubble rows when a foam

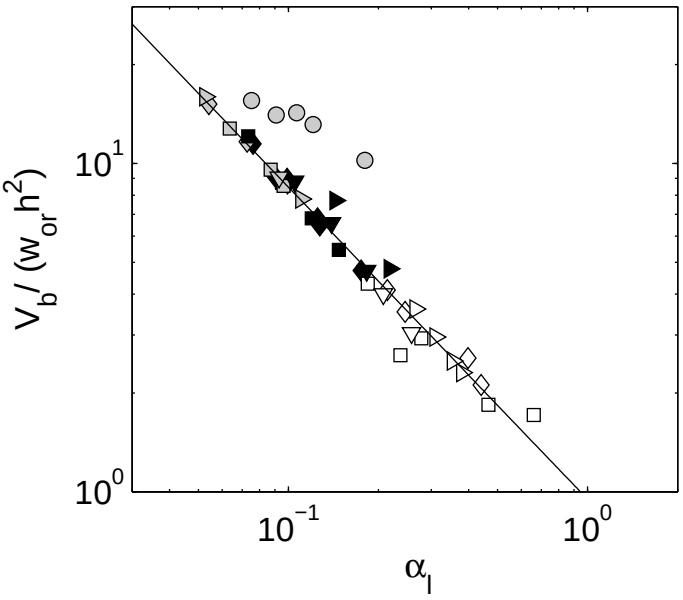

Figure 3.3: The bubble volume V_b, in units of $w_{or}h^2 \simeq 5$ nl, depends only on the injected liquid fraction α_l. The solid line is a linear fit to all data except the lowest Q_l: $\log(V/w_{or}h^2) = (-0.95 \pm 0.02) \log \alpha_l + (-0.05 \pm 0.05)$. Symbols correspond to different values for the liquid flow rate $Q_l =$ (o) 4, ($\diamond$) 15, ($\square$) 20, ($\triangleright$) 30 and ($\triangledown$) 40 μl min^{-1}, for bubbly flows (open symbols), alternate foams (filled symbols), bamboo foams (gray symbols). The data for $Q_l = 4$ μl min^{-1} diverges. A possible cause will be treated in section 3.2.2.

appears would either require decreasing V_b at given Φ_l or enlarge the channel space for newly formed bubbles. In section 3.4 we will precise this in more detail.

3.1.3 Bubbling frequency

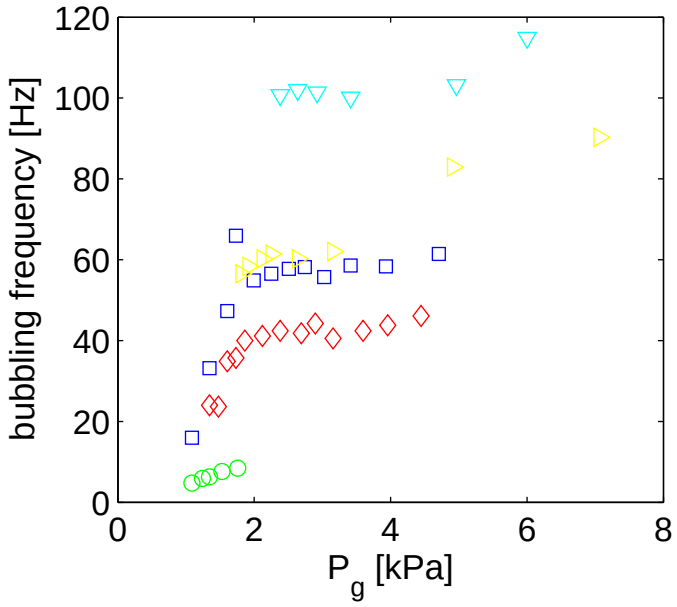

Figure 3.4: The bubble formation frequency f *vs.* gas pressure P_g. Colored symbols correspond to different liquid flow rates: Q_l = (o) 4, ($\diamond$) 15, ($\square$) 20, ($\triangleright$) 30 and ($\triangledown$) 40 μl min^{-1}. The bubbling frequency increases with the liquid flow rate Q_l. For a fixed Q_l it grows at low P_g to reach a plateau for higher P_g.

For the same set of image sequences that we use to analyse the bubble volume, we can also extract the bubbling frequency f. As can be seen in Fig. 3.4, the bubbling frequency increases with the liquid flow rate Q_l. For a fixed Q_l it grows at low P_g to reach a plateau for higher P_g.

We can non-dimensionalize the bubbling frequency by introducing a typical time related to the liquid flow:

$$\tau_l = \frac{1}{f_l} = \frac{w_{or}h^2}{Q_l}. \tag{3.3}$$

This time can be used to define a non-dimensional frequency, known as the Strouhal number,

$$St = \frac{f}{f_l} = \frac{f w_{or} h_{or}^2}{Q_l}. \tag{3.4}$$

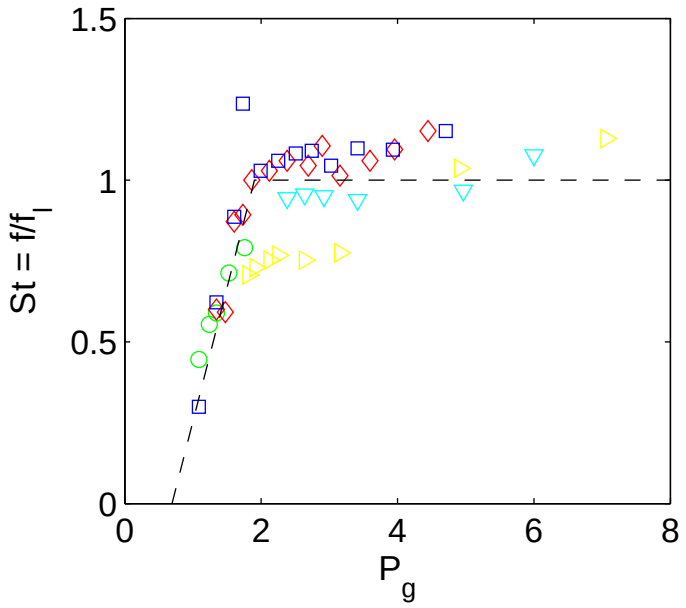

Figure 3.5: The bubble formation frequency f in units of $f_l = Q_l/w_{or}h^2$ *vs.* gas pressure P_g. It shows a plateau for high P_g: the dotted line is a piecewise linear fit. Symbols correspond to the same flow rates as in Figures 3.3 and 3.4.

After rescaling by f_l all data collapse on a single curve where St is a function of gas pressure only (Fig. 3.5). Two regimes are observed: for low gas pressures in the case of bubbly flow we find $St \simeq 0.8(P_g - P_c)$, while for higher P_g, the Strouhal number saturates to a constant value of $St = 1.0$.

We infer that these two regimes are the consequence of two stages during the bubble formation. The two stages take place in both regimes but in each regime one of the two stages is slower in time than the other and therefore dominant:

1. Gas filling of the orifice: At low P_g the frequency varies like $f \sim f_l(P_g - P_c) \sim Q_l(P_g - P_c)$. In other words, the period is proportional to a characteristic time that varies as

$$T \simeq \tau_g \sim [Q_l(P_g - P_c)]^{-1}. \tag{3.5}$$

   We interpret this time as the time necessary for the gas to fill the orifice, prior to break-up. It decreases with increasing $P_g - P_c$, since the gas pushes the fluid with a velocity increasing with pressure. τ_g also decreases for increasing Q_l with the flow-focusing confining more and more the available space for the gas thread. Note that the relation $f \sim Q_l P_g$ was proposed by [28], who checked it for varying Q_l but with a constant P_g or by keeping their product constant: here we also investigate separately the effect of gas pressure.

2. Liquid mediated thread pinch-off: For high P_g the bubble formation frequency is proportional to $f \sim Q_l$. The period only depends on

$$T \simeq \tau_l = \frac{w_{or} h_{or}^2}{Q_l}, \tag{3.6}$$

   the time to pinch off the gaseous thread when the liquid flow is blocked by the bubble at the outlet [29]. The physical meaning of $w_{or} h_{or}^2$ is the volume initially occupied by the gas and then contracted by the liquid flow. In Figure 3.2 this corresponds for a large part to the volume being filled with liquid in time elapsed between image (c) and (e). Besides this part of the orifice the volume also includes a hard to quantify region upstream where the gas and liquid interface can also slightly move. The extent of this region decreases for more efficient restraining by the channel geometry of the gas flow before the orifice, and for large ratios of liquid to gas flow Q_l/Q_g. In section 3.2.2 this dependence will be discussed in more detail, both for different channel geometries and Q_l/Q_g ratios. Postponing discussions on the exact origin and localisation of this pinch-off volume, the scaling in Fig. (3.4) shows that $w_{or} h_{or}^2$ is an appropriate combination of length scales to represent this volume.

As a conclusion, there are two stages during formation: the first associated with the filling of the orifice by the gas (τ_g) and the second reflecting the pinch-off

of the gas thread (τ_l). They have different gas pressure dependency (τ_g depends on gas pressure while τ_l does not). This creates a cross-over apparent in the bubbling period $1/f$ that depends on τ_g and τ_l: the bubbling period at low pressure is limited by the gas filling, while it is limited by the liquid driven thread contraction in the high gas pressure regime.

3.2 Gas thread break-up regimes

In this section, we will show that the standard case of dry foam formation critically depends on confinement of the gas thread break-up to the orifice (section 3.2.1). We will show how this confinement can be influenced both by the channel geometry and by the value of the liquid flow rate Q_l (section 3.2.2).

To investigate this influence of the geometry we will vary the channel design. We will use four geometries (Fig. 3.6 and A.2.1 to A.2.4 in appendix A) differing from the classical one, used until now, in the following points:

- A channel height $h = 100$ μm, instead of 250 μm. This leads to orifices with a square section of 100×100 μm^2.
- Very small water inlet channels with a width $w = 50$ μm. We made this length so small to make it harder for the gas thread to enter the liquid channels instead of the outlet channel. That happened sometimes in the transient phase following a sudden gas pressure increase, due to compressibility of the channel walls and the finite time needed by the syringe pump to adapt to the change in gas pressure.
- A gas inlet decreasing in width. At the junction with the liquid inlets, the gas channel has the same width as the orifice: 100 μm. We will see in the following that this design restrains possible movements of the gas-liquid interface.
- Rounded edges. The corners of the outlet channel presented stagnation points for the liquid flow. It happened that small bubbles became immobilized in these corners. By rounding them we impede this.
- Increased channel width: $w = 1000$ μm instead of 700 μm.

In addition to the modifications described above, the four geometries all have different orifice lengths varying from $l_{or} = 800$ μm to $l_{or} \simeq 50$ μm (Fig. 3.6b to e).

3.2.1 Break-up confined to orifice: effect of orifice length

We will repeat the same type of measurement as described before: for a given liquid flow rate Q_l, vary the gas pressure P_g and measure the bubbling frequency

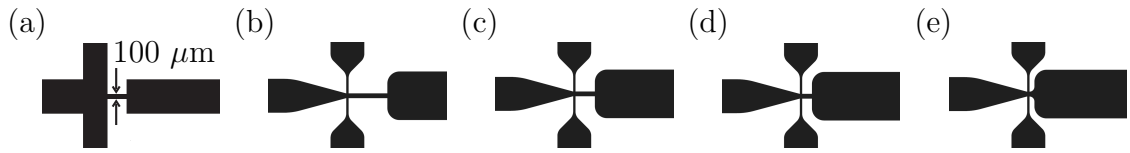

Figure 3.6: Different channel designs. The principal difference with the classic design (a) consists of the variation of the orifice length: (b) $l_{or} = 800$, (c) $l_{or} = 400$, (d) $l_{or} = 200$, (e) $l_{or} \simeq 50$ μm, instead of (a) $l_{or} = 400$ μm (together with larger input channels before the orifice).

f, volume V_b and gas flow rate $Q_g = V_b f$. The channel design, however, has not only profoundly changed, we will also vary the orifice length from $l_{or} = 200$ μm to 800 μm (Fig. 3.6b to d). The very short orifice (e) will be discussed in section 3.2.2, as it will present an exception to what we will show now.

Bubbling regimes

A first thing that can be noticed about the bubbling in these modified geometries, is the absence of both the dripping and the bidisperse regime (see images in Fig. 3.7). The only bubbling we observe is in the monodisperse regime for which the gas thread after release of a bubble does not significantly move upstream of the orifice. We think this to be related to the change of the channel shape upstream of the orifice. Because of the shape of the gas inlet and the small width of the liquid inlets the length of the gas-liquid interface upstream of the orifice has been reduced from $\simeq 600$ in the classic design (Fig. 3.8a) to 50 μm (Fig. 3.8b). We believe the gas-liquid interface to be much more restrained, thereby favoring the monodisperse bubbling regime. This also seems to indicate that if one wants to use a flow-focusing device in the dripping regime, *e.g.* to produce single, monodisperse small bubbles (with $d_b \simeq w_{or}$) at a large inter-bubble distance, it is a good idea to use a design with a long gas-liquid interface upstream of the orifice.

Pinch off volume

The data points for different orifice lengths in Fig. 3.7 show a remarkable overlap. Both bubbling frequency and volume seem to be independent of orifice length. When we take a look at the final stage of bubble pinch-off (Fig. 3.9), we see that the volume pinched by the liquid does not depend on the orifice length. For a given liquid flow rate and gas pressure, pinch-off takes place at a fixed distance from the orifice, independent of orifice length. This distance increases with the liquid flow rate (as can be seen by comparing Fig. 3.9 and Fig. 3.12), and also

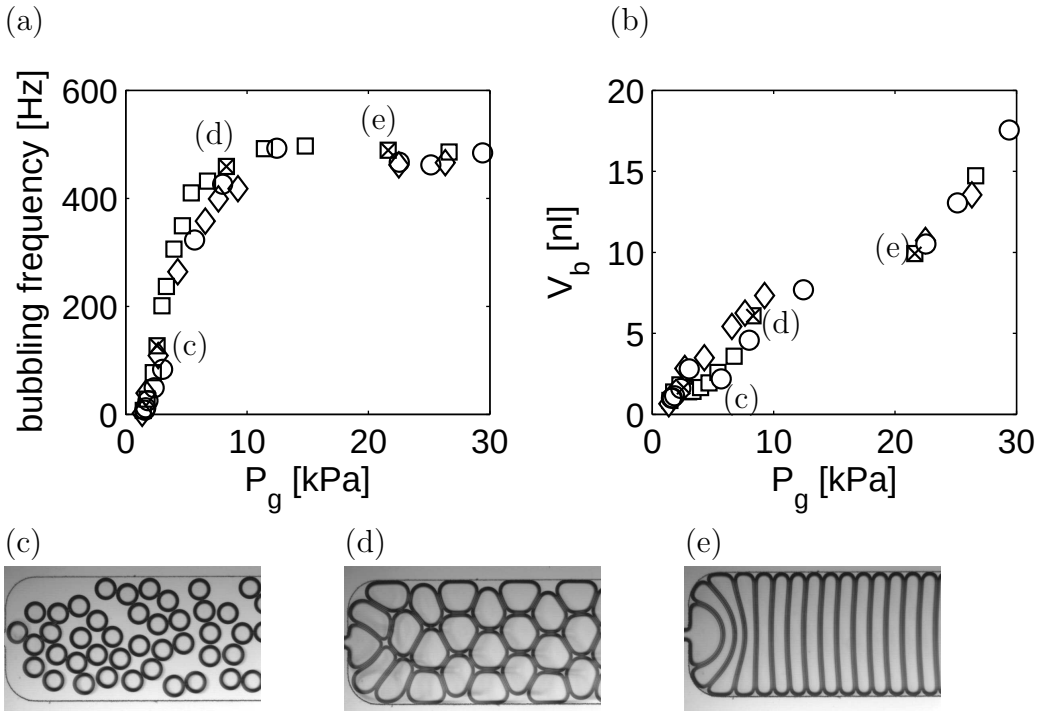

Figure 3.7: Bubbling is independent of orifice length. Bubble frequency (a) and volume (b) for a fixed liquid flow rate $Q_l = 30$ μl/min and $l_{or} = (\diamond)$ 200, $(\square)$ 400 and (o) 800 μm. Still images (c), (d) and (e) correspond to crossed symbols in (a) and (b).

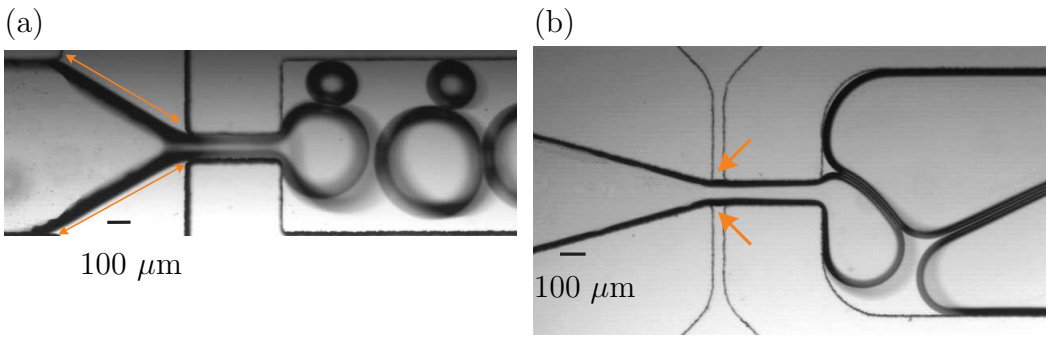

Figure 3.8: The gas-liquid interface (indicated by the orange arrows) upstream of the orifice is much longer in (a) ($l \simeq 600$ μm), than in (b) ($l = 50$ μm). A long interface length favors the existence of the dripping and bidisperse bubbling regime.

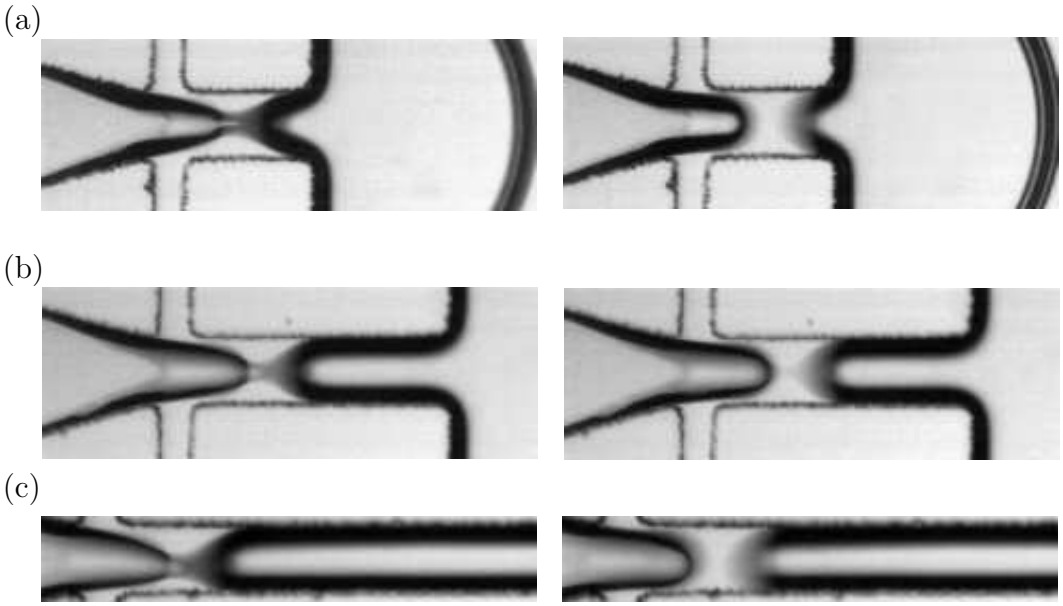

Figure 3.9: The bubble pinch off does not depend on the orifice length. Pictures represent three different orifice lengths: l_{or} = (a) 200, (b) 400 and (c) 800 μm. The left column shows the final stage of gas thread break-up. Note that the gas thread stays in the orifice after break-up (right column). The liquid flow rate is kept constant at Q_l= 30 μl/min, the gas pressure is approximately constant with $P_g = 26.0 \pm 0.9$ kPa.

with the gas pressure P_g (Fig. 3.10), it does not depend however on the orifice length.

Here we will discuss the case for which the gas thread stays in the orifice after release of a bubble (Fig. 3.9), so for both P_g and Q_l sufficiently high. For this case, the total volume pinched by the liquid can by approximated by:

$$V_{\text{pinch-off}} = w_{or} h l_{\text{pinch-off}}, \tag{3.7}$$

with $l_{\text{pinch-off}}$ the length over which the gas thread is pinched. We find this length to be the largest of the two that make the orifice section: h and w_{or}. This can be justified by assuming the shape of the gas-liquid interface to be close to a minimal surface between two rectangles with section $h \times w_{or}$. The maximum distance between the two rectangles before the interface becomes instable depends on the largest of the two lengths making the orifice section.

$V_{\text{pinch-off}}$ is equal to V_l, used in sections 3.1.2 and 3.1.3. It will now allow us to make a comparison with the results obtained in the classical channel for both the frequency and the volume data.

Bubbling frequency and bubble volume

At the high liquid flow rate of $Q_l = 30$ μl/min (Fig. 3.7), gas-thread break up is confined to the orifice. For this case the frequency shows the same qualitative behaviour as in Fig. 3.4: a linear part where $f \sim (P_g - P_c)Q_l$, and a plateau only depending on Q_l.

We can compare the frequency data with the one obtained for the classical channel by rescaling with $f_l = Q_l/V_l$. The most notable difference, affecting the frequency, between these two geometries is in the lower channel height h leading in the classic case to $V_l = w_{or}h^2 = 5.1$ nl and for the actual geometries to $V_l = w_{or}h^2 = 1.0$ nl, hence to a higher saturation frequency $f_l = Q_l/V_l$. As can be seen in Fig. 3.11, for high Q_l the frequency collapses to the fit of the classic data. Note that to compare the frequency in different geometries the appropriate physical property is not the experimental control parameter gas pressure P_g, but the related gas flow rate Q_g.

For the microbubble volume too (after rescaling by V_l) we find a good overlap for the data at different l_{or}, except at very low injected liquid fraction α_l.

We conclude from this: that bubble formation is independent of orifice length; and that $V_{\text{pinch-off}} = w_{or} h l_{\text{pinch-off}}$ is the correct volume to rescale both the bubbling frequency and bubble volume, for the case of gas-thread break up confined to the orifice. Note that a similar volume has been found in the case of axisymmetric flow-focusing devices by Lorenceau and co-workers [43]. In that case, for which the orifice width is continuously varying, V_l was found to be the volume contained in the part of the orifice where $w_{or} < 1.5\, b$, with b the minimum orifice width. After rescaling the bubble volume by V_l, data obtained in devices with different lengths collapse on the same master curve.

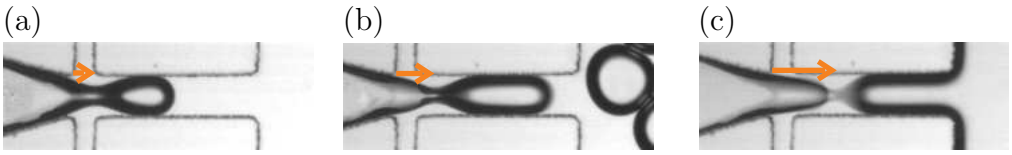

Figure 3.10: Bubble pinch-off. For increasing gas pressure (P_g= (a) 1.45, (b) 3.36 and (c) 26.7 kPa) the thread pinches further away from the orifice entrance. All data for l_{or} = 400 μm, and Q_l = 30 μl/min. Arrows indicate the increasing distance between the end of the gas inlet and the center of the pinch-off area.

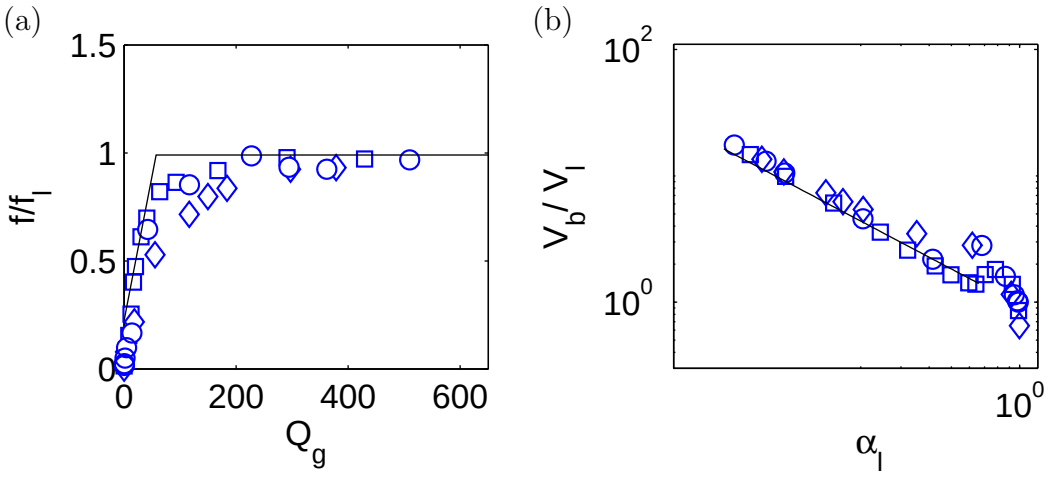

Figure 3.11: Bubble generation in modified channels. (a) The normalized bubbling frequency f and (b) the bubble volume V_b for Q_l= 30 μl/min *vs.* the gas flow rate Q_g. Symbols correspond to different orifice lengths: l_{or} = ($\diamond$) 200, ($\square$) 400 and (o) 800 μm. The continuous line represents a piecewise linear fit to the bubbling frequencies obtained in the classical channel (Fig. 3.3 and 3.5).

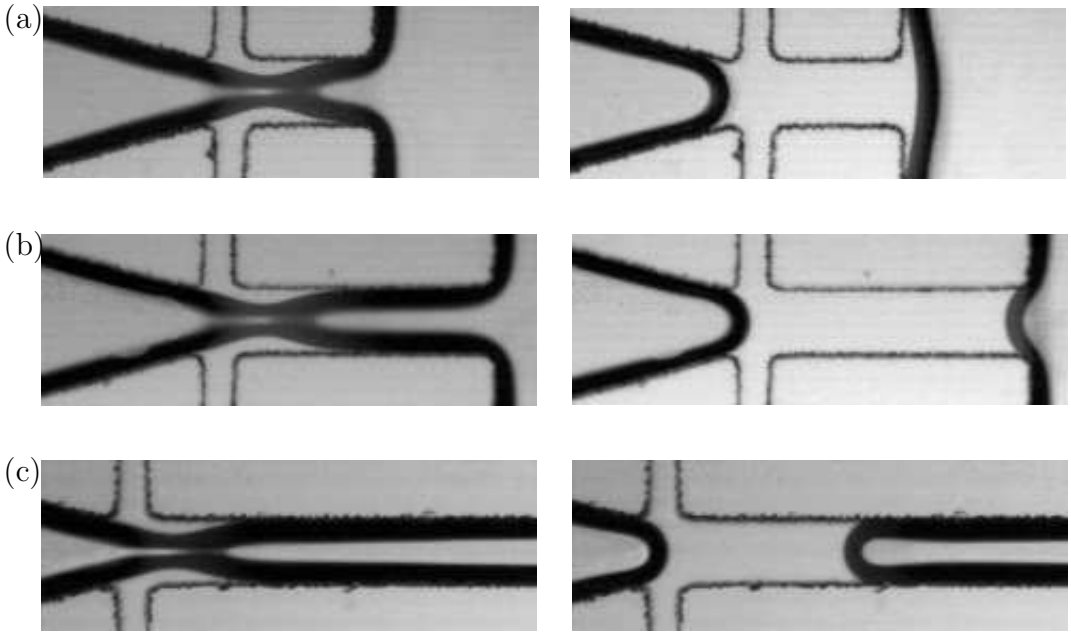

Figure 3.12: Final stage of bubble pinch off for the low liquid flow rate $Q_l = 3$ μl/min. Pictures represent three different orifice lengths: l_{or} = (a) 200, (b) 400 and (c) 800 μm. Gas pressure is approximately constant at $P_g = 3.1 \pm 0.1$ kPa. Pinch off takes partially place upstream of the orifice (left column). After break up, the interface retracts upstream of the orifice (right column).

3.2.2 Partial confinement of the break-up

In the following we will discuss two cases for which, upon rescaling, the frequency and volume data do not all fall on the same mastercurve: the case of low Q_l, and the channel geometry with an orifice volume smaller than V_l.

1) Interface retraction at low Q_l

Bubble pinch-off at low liquid flow rate Q_l is located further upstream than for high Q_l, as can be verified by comparing Fig. 3.9 and Fig. 3.12. As a result the gas thread retracts upstream after releasing a bubble (Fig. 3.12, right column of images). In the following, we will show how this influences the bubbling frequency and the bubble volume. Note that break-up is again independent of the orifice length.

For this low liquid flow rate, the frequency and the bubble volume grow with the gas pressure (Fig. 3.13). The frequency does not saturate however, for increasing gas pressure, because the transition from foam to stratified flow takes place before. Both the frequency and the bubble volume show a discontinuity

around $P_g = 2.2$ kPa: for increasing P_g the frequency and bubble volume show a temporary drop. We will discuss this effect in detail in chapter 4. It is related to the topology change in the outlet channel from an F2 to an F1 foam, inducing an increase in the system's resistance to flow. We did not see this discontinuity in the frequency in Fig. 3.4 and 3.5, because in that case the topology transition took place in the saturated regime for which the liquid flow rate is the only factor determining f.

We will now rescale again the bubbling frequency and the bubble volume for comparison with the master curves (Fig. 3.14). We see that, in contrast to the case in which bubble break up is completely confined to the orifice, both f and V_b do not fall on their respective mastercurves. The bubbling frequency is systematically lower and the bubble volume larger. We have two possible explanations:

1. The blocking of the outlet channel by the gas thread is less efficient. At high Q_l the gas thread remains permanently in the orifice, thereby restraining liquid flow to the corners. For low Q_l, just after bubble pinch off, the liquid can flow unobstructedly through the orifice. One can interpret this as "leaking" leading to smaller frequencies: $f_l = V_l Q_{l,eff}$, with the effective liquid flow rate $Q_{l,eff} < Q_l$.

2. The pinch off does not completely take place in the orifice, but also upstream. This can increase the gas volume to be contracted, thereby decreasing the frequency.

A lower frequency automatically leads to a larger bubble volume: for a given α_l we find a larger V_b and smaller f. $\alpha_l = Q_l/(Q_g + Q_l)$, so fixing α_l (at constant Q_l) means fixing $Q_g = V_b f$. Thus if, for some reason, f decreases, in this case due to pinch off at the orifice entrance, then, for a given α_l, V_b will increase, to keep the product constant.

Note that both effects should be less pronounced for higher gas pressures because they tend to confine the pinch off more and more into the orifice. We do not observe this at this low liquid flow rate because the transition to stratified flow takes place before P_g becomes high enough for effective restriction.

In section 3.1 we have seen that the bubble volume V_b only depends on the injected liquid fraction α_l. It was found to be independent of the liquid flow rate Q_l. To this we have now added the exception of very low liquid flow rates, leading to less efficient restriction of the liquid flow by the gas thread; and thereby to lower frequencies and larger bubble volumes for a fixed liquid fraction. Unfortunately we have only showed this behaviour at low Q_l for one particular value ($Q_l = 3$ μl/min). It would be very interesting to see what happens for intermediate flow rates. It would allow to determine the critical flow rate $Q_{l,cr}$ for which V_b becomes independant of Q_l. It would also clarify the relation between V_b and Q_l for liquid

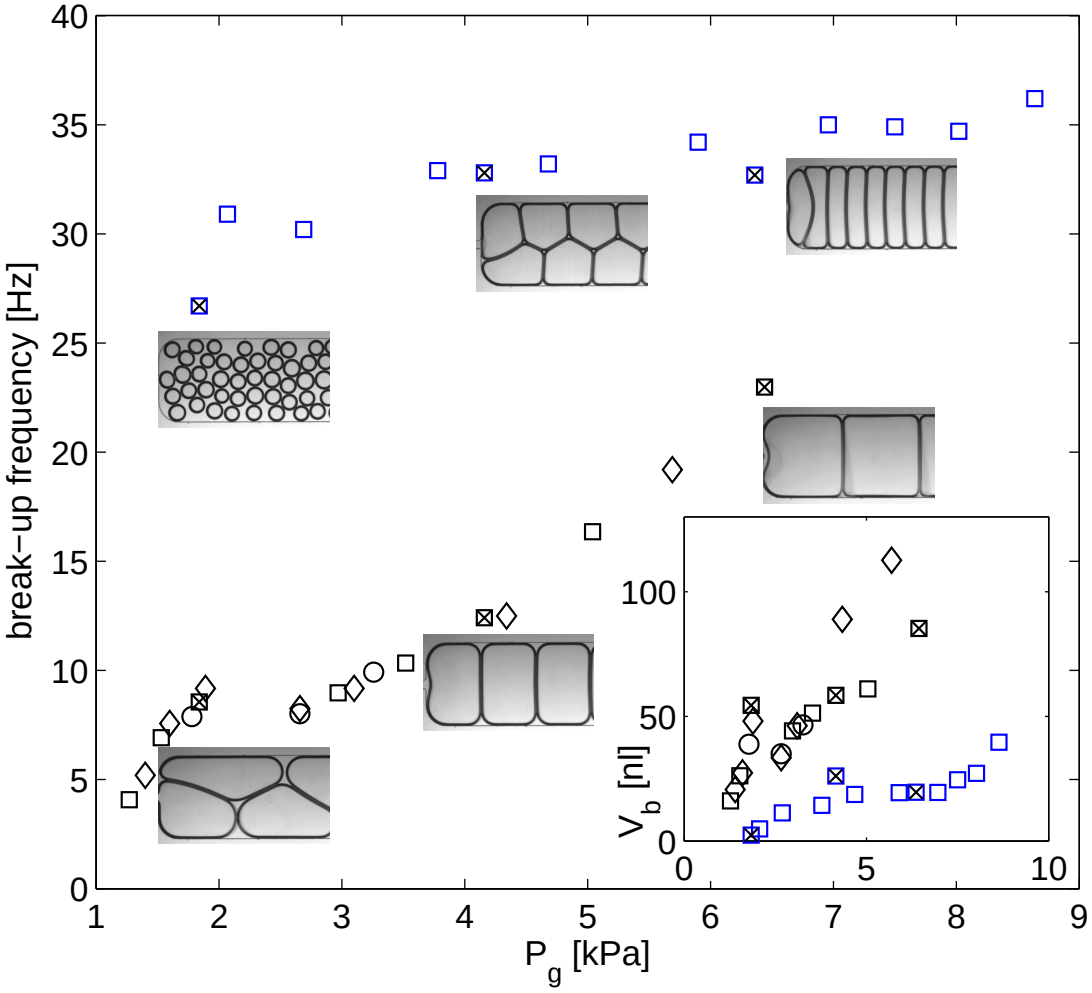

Figure 3.13: Bubbling at low liquid flow rate Q_l. Bubble frequency and volume (insert) for a fixed liquid flow rate $Q_l = 3$ μl/min and $l_{or} =$ ($\diamond$) 200, ($\square$) 400 and (o) 800 μm. Blue symbols correspond to a transient situation caused by partial dewetting of the orifice region that will be discussed in section 3.2.2

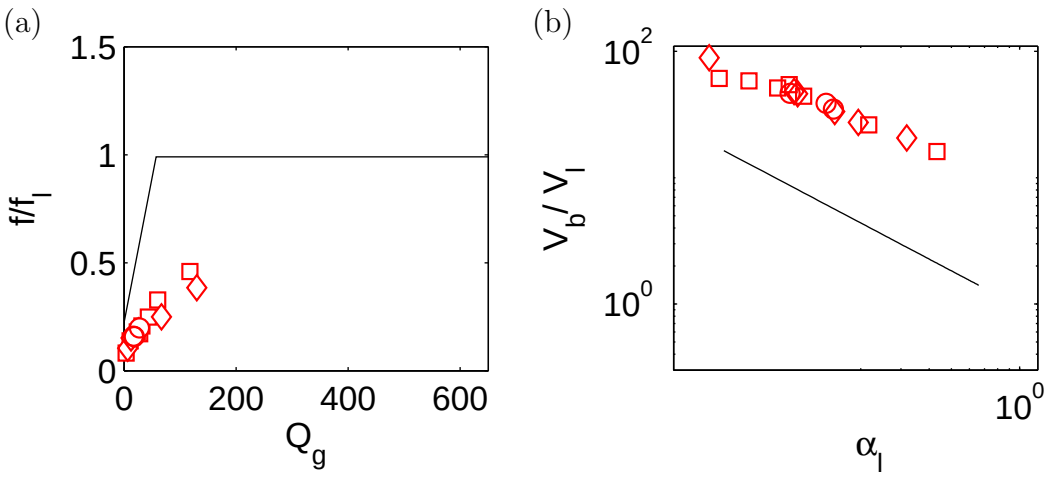

Figure 3.14: Bubble generation at low liquid flow rate Q_l. (a) The bubbling frequency f *vs.* the gas flow rate Q_g and (b) the bubble volume V_b *vs* the liquid fraction α_l. Symbols correspond to the same orifice lengths as in Fig. 3.13. The continuous line is the piecewise linear fit to the bubbling frequencies (Fig. 3.5) and volumes (Fig. 3.3) obtained in the classical channel.

flow rates below $Q_{l,cr}$. With respect to this, we can say that for geometry A.1 in section 3.1, from $Q_l = 15$ μl/min and upwards, V_b is independent of Q_l. We conjecture that the actual physical property on which the transition from partial to completely orifice confined gas thread break-up depends, scales with the ratio of the orifice sections $h_1/h_2 = 0.4$. In that case, $Q_{l,cr}$ should be smaller than $Q_l = 0.4 \times 15 = 6$ μl/min.

Exception: dewetting maintains confinement to orifice We will now present an experimental situation where due to a dewetting effect that we will describe below, the bubble pinch-off is confined to the orifice, even at low Q_l. This will allow us to validate our claim about the influence of the confinement by the orifice.

The gas bubbles in our system are surrounded by a continuous liquid film. The same is true for the gas thread in the orifice. In the gas inlet, however, gas is in direct contact with the channel walls. This means that somewhere, ususally just before the junction between gas and liquid inlets, a triple contact line (gas, liquid and PDMS) is created (Fig. 3.15a). This line indicates the start of the continuous liquid film.

We do not believe that this inevitable triple contact line influences the bubble formation and flow as it is located upstream of the area where bubbles are formed. A different situation can occur, when a freshly produced channel is taken into

use. As explained in section 2.2.3, the channel walls are initially hydrophobic, but rapidly become hydrophilic. There is a transient regime, where the walls are sufficiently wetting to allow bubble generation, but not enough to prevent dewetting of the gas thread after the junction with liquid inlets. This leads to a different location of the contact line, more downstream (Fig. 3.15b).

(b)

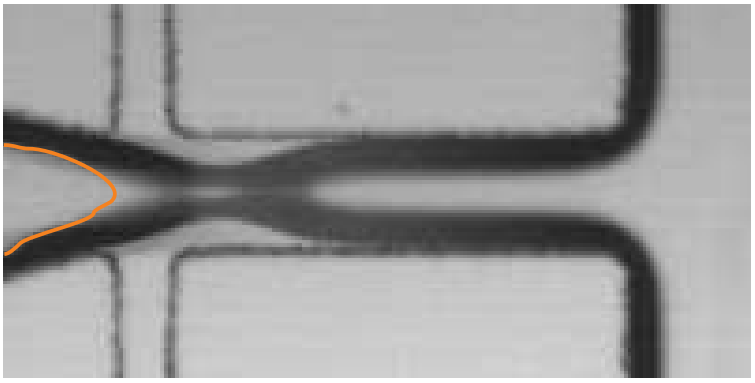

(a)

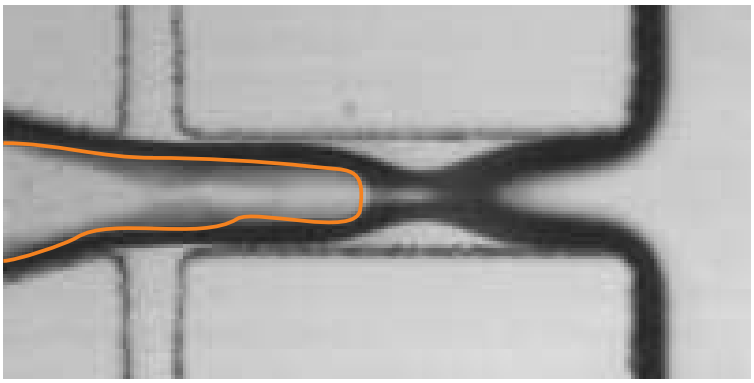

Figure 3.15: Triple line (indicated in orange) between gas, liquid and PDMS for totally wetting walls (a) and partially wetting walls (b). In the partially wetting case, the contact line confines the bubble pinch-off to the orifice, thereby modifying the bubble generation.

For channel walls that preferentially wet the liquid, the pinch off position can vary. As we have seen before, it depends on the liquid flow rate (Fig. 3.9 and Fig. 3.12) and the gas pressure (Fig. 3.10). For the case with only partial wetting, the pinch off is confined further downstream, in the orifice (Fig. 3.15).

For channel A.2.2 we measured the bubbling frequency f and volume V_b shortly after the first time use of this channel. We repeated the same measurement later in time, with wetting walls. This leads to very different values: V_b is smaller and f higher, as can be seen in Fig. 3.13, which represents the influence of the channel geometry on the bubble formation. By slightly displacing the pinch off location (by 1.5 w_{or} in Fig. 3.15), bubble size and thereby topology

vary considerably for constant input parameters. We can compare the frequency and bubble volume with their respective master curves (Fig. 3.16). The data for pinch off confined to the orifice is much closer to these curves than for the wetting case. This again confirmes our conclusions on the role of confinement by the orifice on bubble generation.

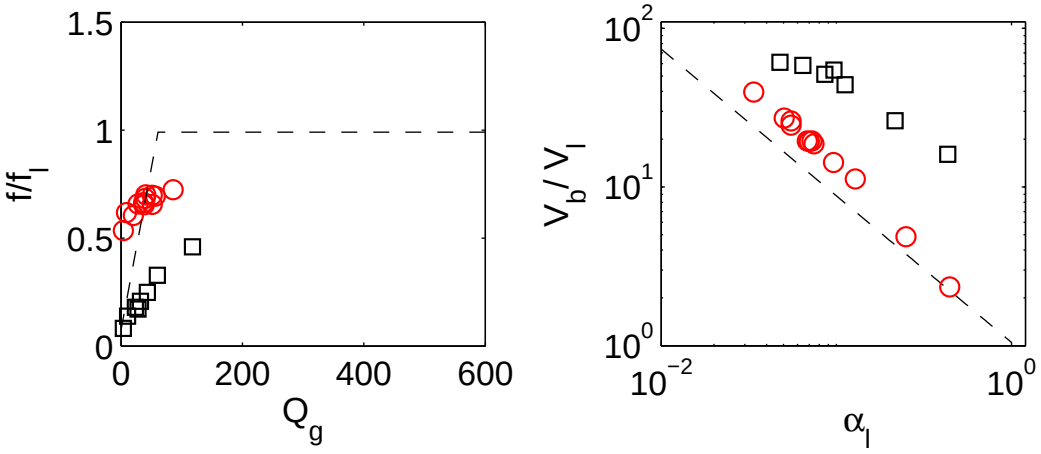

Figure 3.16: Dewetting: comparison of the bubbling frequency (a) and the bubble volume (b) between the wetting (black symbols) and partially wetting (red symbols) case and the master curves of Figs. 3.3 and3.5, in channel A.2.2 with $Q_l = 3$ μl/min.

In our case, this bubble regime is just a consequence of uncontrolled, temporary dewetting. It indicates a possible way though to extend the range of gas pressures and liquid flow rates for which our master curves for bubble generation are applicable. To make this possible, one should permanently pin the contact line shown in Fig. 3.15b to a position where it confines the pinch off to the orifice. This might for example be done by surface treatment of only a part of the channel walls.

2) Ultrashort orifice

A second situation in wich the orifice can not completely confine the gas thread pinch-off is for orifice lengths smaller than the pinch off length: $l_{or} < V_l^{1/3}$, as is the case for the channel design in Fig. 3.6e. For this geometry V_b (resp. f) doubles (resp: is divided by two) compared with the $l_{or} > V_l^{1/3}$ case (Fig. 3.17).

At low liquid flow rate, we can also note the absence of the discontinuity in the pressure and the frequency. This is due to the absence of the transition from F2 to F1. Bubbles are so big that they arrange in the F1 topology, even for low P_g.

At high liquid flow rate the frequency does not reach saturation; V_b is larger than for the long orifices, whatever P_g.

Comparison (Fig. 3.19) with the mastercurves from Figs. 3.3 and 3.5 shows a deviation, that we explain, like in section 3.2.1, by a partial blocking of the liquid flow by the gas thread in the orifice for two reasons:

1. At low Q_l, the pinch off takes place partially in the orifice and partially upstream (Fig. 3.18 a). At high Q_l, the pinch off takes place partially in the orifice and partially downstream (Fig. 3.18 b). Both cases lead to the same situation: a possible increase in the gas volume to be contracted, thereby decreasing the frequency.

2. The blocking of the outlet channel by the gas thread is less efficient. At both low and high Q_l the gas thread retracts upstream after pinch-off (Fig. 3.18 b and d). In the time between this retraction and the start of the filling of a new bubble, the liquid can flow unobstructedly through the orifice. One can interpret this as "leaking", leading to smaller frequencies: $f_l = V_l Q_{l,eff}$, with the effective liquid flow rate $Q_{l,eff} < Q_l$.

3.2.3 Foam liquid content

One of the most important properties of a foam is its liquid content. It is an essential parameter in foam structure (bubble shape), rheology (elasticity, yielding), coarsening (gas flow from small to big bubbles) or drainage (a liquid flow in a foam, in general due to gravity).

As we saw in section 3.1, in the standard case of foam generation with bubble break-up confined to the orifice, we cannot independently vary the bubble volume and the liquid fraction. This case corresponds to a gas thread break-up that is completely confined to the orifice, and leads to the driest foams we succeed to produce.

We can obtain wetter foams however, by employing the effects described in this section (Sec. 3.2), that lead to a less efficient confinement of the gas thread break-up in the orifice. A first method uses low liquid flow rates, to let break-up take place at the entrance of the orifice. A second method changes the orifice length below a critical length that is related to V_l. It allows to change α_l by a factor four, at a given bubble volume, or even a factor five if both methods are combined.

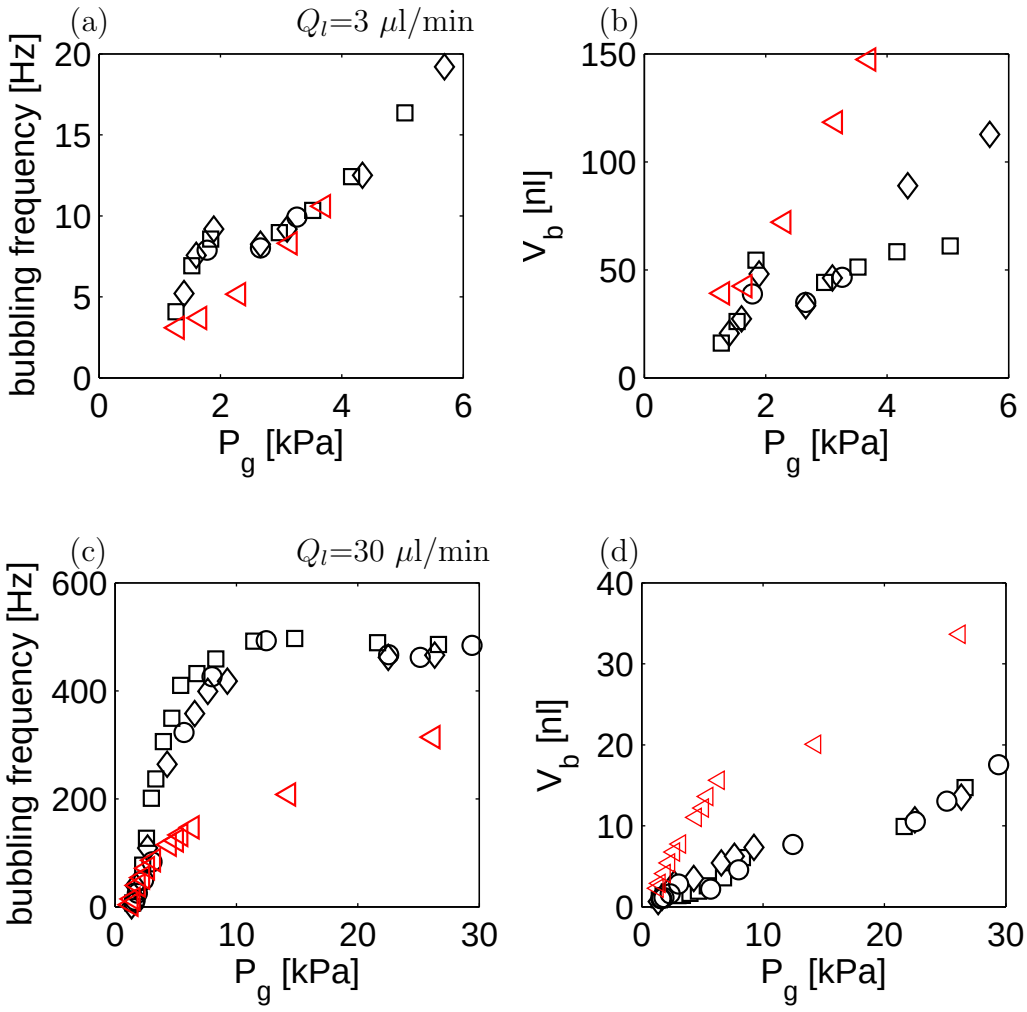

Figure 3.17: Ultrashort orifice, $l_{or} \simeq 50$ μm, (red symbols). Frequency and bubble volume *vs.* the gas pressure at low (a, b) and high (c, d) liquid flow rate. Black symbols correspond to the same orifice lengths as in Fig. 3.13.

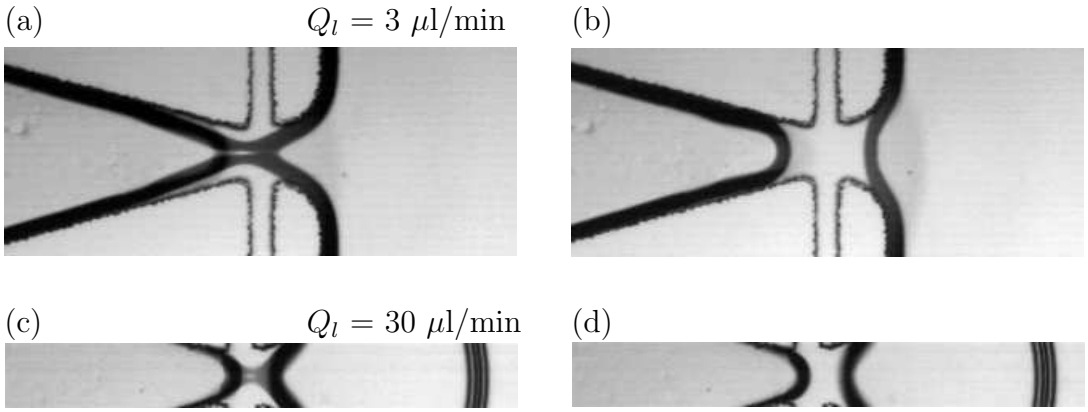

Figure 3.18: Bubble formation in the ultra short orifice ($l_{or} \simeq 50$ μm). For low liquid flow rates, bubble pinch off takes place upstream of the orifice (a). After releasing a bubble, the gas interface retracts upstream of the liquid inlets (b). At high liquid flow rates, pinch-off takes partially place in the outlet channel (c). After releasing a bubble, the gas interface retracts upstream of the orifice (d).

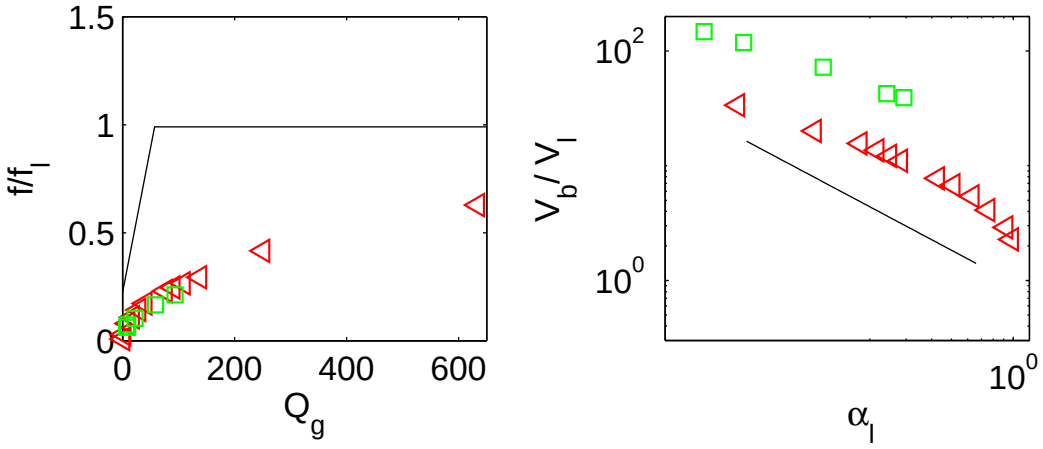

Figure 3.19: Ultrashort orifice: comparison of the bubbling frequency (a) and the bubble volume (b) for two different flow rates: $Ql = 3$ μl/min (green symbols) and $Ql = 30$ μl/min (red symbols).

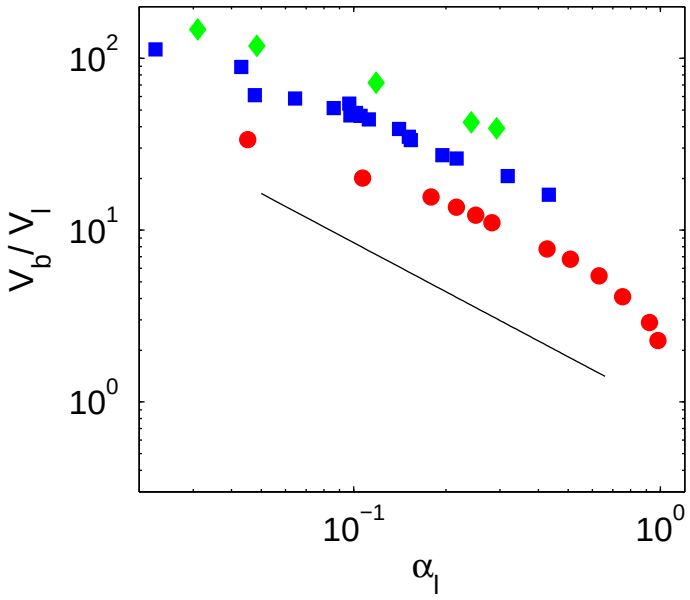

Figure 3.20: Bubble volume *vs.* the liquid fraction for different break-up regimes: confined to the orifice (continuous line), partial confinement at low Q_l (blue symbols) and partial confinement in a very short orifice at low (green symbols) and high Q_l (red symbols).

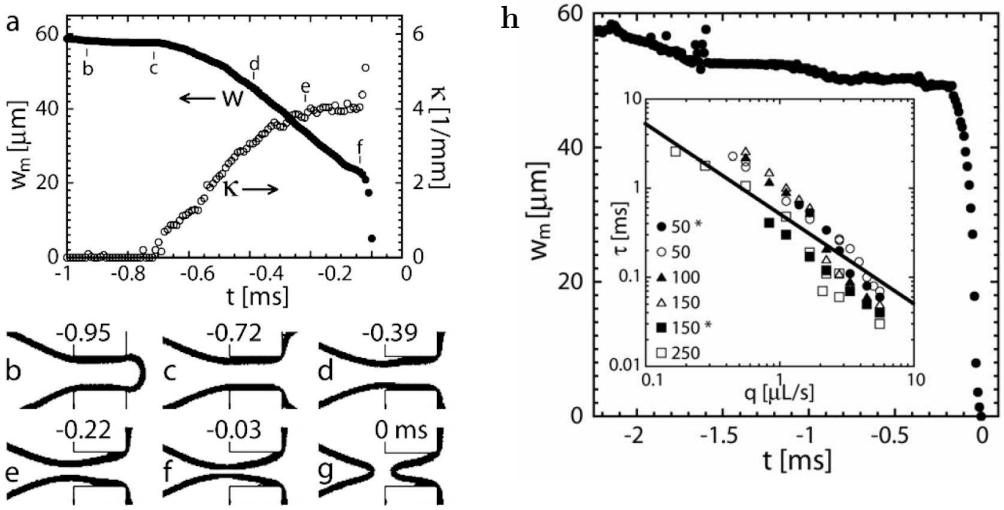

Figure 3.21: After Garstecki *et. al.* [29]. (a) Break-up in an elongated orifice: evolution of the minimal width w_m, and the axial curvature κ of the gas-liquid interface in a typical break-up event ($w_{or} = 60$ μm, $h = 36$ μm, $Q_l = 0.56$ μl/s, $P_g = 34.5$ kPa). (b)-(g) Optical micrographs of the gas-liquid interface along the break-up trajectory. Numbers indicate time in ms.
(h) After Garstecki *et. al.* [26]. Evolution of w_m in an orifice of an almost square cross-section ($h = 64$ μm and $w_{or} = 60$ μm). Inset shows the variation of the time interval τ between the entrance of the thread into the orifice and final break-up, as a function of the flow rate of the continuous fluid. The numbers in the legend give the length l_{or} of the orifice in each series. The flow parameters were set to the following values: $P_g = 34.5$ kPa (no star) or $P_g = 69$ kPa (star). The solid line is a fit $\tau \propto Q_l^{-1}$.

3.3 Orifice aspect ratio

Our interpretation of bubble generation in terms of V_l and the related typical time $\tau_l = V_l/Q_l$ (eq. (3.3)) allowed for rescaling to the same master curve of bubble volumes obtained in both square and elongated orifices. In collaboration with B. Dollet, W. van Hoeve and M. Versluis, we have shown however that break-up in elongated and square orifices does not follow the same mechanism [16]. In the following we will discuss this paradox. Therefore we will first briefly present the work on gas thread pinch-off by Garstecki and co-workers [29, 26]. Then we will show the results of our collaboration with *Dollet et. al.*. This will be followed by a discussion.

3.3.1 Bubble break-up by Garstecki *et. al.*

To study bubble formation in flow focusing devices, Garstecki *et. al.* measured the evolution of the minimal width w_m of the gas thread in the orifice during break-up [29]. In a rectangular orifice, break-up was measured to be linear in time over a large part of the bubble collapse (see Fig. 3.21a, linear break-up from (c) to (f)). Furthermore during this phase, w_m was found to scale with the liquid flow rate: $\mathrm{d}w_m/\mathrm{d}t \propto Q_l$. This linear gas thread thining is followed by a fast final collaps ((f) and (g)). Varying the surface tension σ did not modify $\mathrm{d}w_m/\mathrm{d}t$.

The observation that the break-up speed scales with Q_l and is independent of σ, leads the authors to propose that the gas-liquid interface is stable during the linear part of break-up and that it proceeds through a series of equilibria of the position of the gas-liquid interface. This was justified on one example, by proving the agreement between one experiment and the corresponding computation with surface energy minimization.

For square orifices (Fig. 3.21h), Garstecki does not find a linear time dependance for w_m. A phase in which w_m hardly changes is followed by a fast non-linear collapse. Break-up time, however, is found to scale with Q_l.

3.3.2 Results from [16]

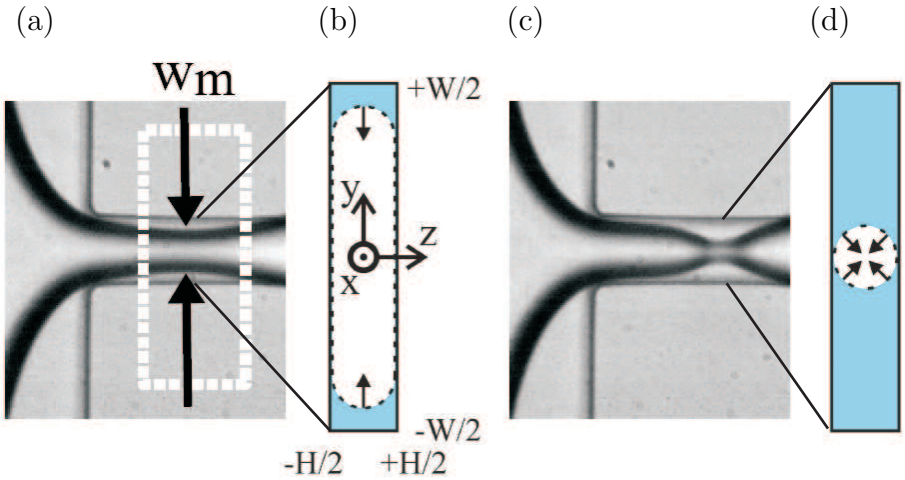

Figure 3.22: Snapshots of the gas thread in the 2D and 3D regime of break-up in a rectangular orifice. (a) The gas thread is first squeezed inwards from the sides by the surrounding liquid: w_m is its minimal width. A cross section of the orifice at w_m is sketched in (b). The gas thread experiences finally a fast pinch-off (c), where it is squeezed radially in the cross-section (d). Figure taken from [16].

The experimental part of [16] is again based on the measurement of w_m, the minimum width of the gas thread in the orifice, during bubble break-up. This

measurement identifies two different regimes during bubble break-up: a 2D phase and a 3D phase. In the 2D phase the shape of the gas-liquid interface only varies in the x and y direction, hence the name (Fig. 3.22a and b). The minimum width w_m of the gas thread is measured to decrease linearly with time, in agreement with the $\mathrm{d}w_m/\mathrm{d}t \propto Q_l$ relation measured by Garstecki.

For $w_m \leq h$ (the final stage of bubble break-up), the shape of the gas-liquid interface can also vary in the z direction, therefore we will name this phase the 3D collapse (Fig. 3.22c and d). In this phase the minimum width is measured to vary like $w_m \propto t^{1/3}$, also independent of P_g. The transition from a 2D to a 3D collapse takes place for $w_m = h$, implying that in square orifices only the 3D regime can exist and explaining the absence of a linear regime in Fig. 3.21h. Note that the above description of bubble formation, neglects the phase preceding break-up in which the gas thread penetrates and fills the orifice that does show a pressure dependence.

In addition to these experimental results, the paper includes a stability analysis showing that the gas-liquid interface during the 2D part of the collapse is always stable, while it becomes unstable during the 3D part. The stability during 2D collapse is supposed to explain the high reproducibility of the break-up event that leads to the monodispersity of the bubbles. The above confirms in a more general way the earlier work by Garstecki [29] in which he proposes that bubble break-up proceeds through a series of equilibria of the gas position of the gas liquid-interface.

The 3D collapse is unstable and scales to $w_m \propto \tau^{1/3}$. The value of the exponent shows that the collapse is independent of surface tension [16]. Together with the results of Garstecki *et. al.* who showed experimentally that the 2D collapse proceeds at a speed independent of surface tension, shows that the *entire* collapse does not depend on surface tension but solely on the inertias of both liquid and gas.

3.3.3 Discussion

Here, we will try to make it plausible that the above (section 3.3.2) is *not* in disagreement with our analysis of gas thread break-up in terms of a typical volume V_l, initially occupied by the gas, that is gradually filled with the liquid arriving at a pace $\tau_l = V_l/Q_l$ (eq. (3.3)).

First, the scaling found in [16] for both time dependancy of the 2D collapse: $w_m \propto \tau Q_l$, and the 3D: $w_m \propto \tau^{1/3}$, are in agreement with eq. (3.3). Indeed during the 2D collapse essentially only one from the three dimensions in V_l, is free to move leading to a linear relation. For the 3D collapse, all three dimensions can move, giving exponent 1/3.

To validate our approach, we will now compare the typical time $\tau_l = V_l/Q_l$ with the data presented above, by Garstecki for gas thread break-up in elongated (2D and 3D collapse) and square (only 3D) orifices. The one example shown

for break-up in an elongated orifice (Fig. 3.21a) belongs unfortunately to the case of partially confined break-up, as shown by the position of w_m at the orifice entrance. This means that during break-up also a hard to define part of the region upstream of the orifice changes shape (images (b) to (e)), that we do not take into account in V_l. τ_l will therefore only by applicable to the last part of break-up. We calculate τ_l for this geometry and control parameters to be $\tau_l = V_l/Q_l = 0.23$ ms. And indeed this corresponds to the time elapsed between image (e) and (g). For the square orifice (Fig. 3.21h) the liquid flow rate is varied from $Q_l = 0.2$ μl/s to 5 μl/s, leading to a typical break-up time between $\tau_l = 0.05$ ms and 1.2 ms, in good agreement with the experimentally measured values. This seems to indicate two possible scenarios:

1. although the final 3D collapse is unstable, it is limited by the arrival speed of the liquid. Leading to a situation in which it cannot develop faster than allowed by Q_l. This would be in agreement with [16].

2. the stability analysis for the 3D collapse assumes a geometry with a cylindrical channel and a concentric gas thread with a constant radius. The actual geometry and shape of the gas thread are more complicated, perhaps leading to stability of the gas-liquid interface during an initial part of the 3D collapse as also seems to be indicated by the simulations in [29]. This scenario would lead to a final phase of the 3D collapse that is in agreement with [16]

The above shows, that bubble break-up is still an open subject. Some details of the final break-up are as yet unclear and the pressure dependent initial phase in which the gas thread enters the orifice remains largely unexplored. In this context we would like to propose that a model to describe every step of bubble formation should consist of three parts:

- A part to describe the time needed for the gas to enter and fill the orifice following release of a bubble. As we showed in section 3.1.3, this regime is dominated by the gas pressure.

- A part characterized by thinning of the gas stream upstream mostly upstream giving $\tau_l = V_{upstream}/Q_l$. This part will be more dominant for partially confined gas thread break-up, and for geometries with a large width of the gas inlet (see section 3.2.1). It is a 2D collapse as only one length-scale is changing upon thread thining. For bubble formation confined to the orifice this phase will be absent.

- The final gas thread break-up characterized by $\tau_l = V_l/Q_l$. This collapse is only 3D in a square orifice and both 2D and 3D in a rectangular orifice. Dry foam formation (break-up confined to the orifice and high gas pressure) is completely dominated by this regime.

3.4 Foam topology: number of bubble rows

3.4.1 Simple model

In section 3.1.2 we stated that the number of rows of bubbles that fit into the outlet channel width (foam topology), depends on the bubble volume for given liquid fraction and the amount of space (channel width) available for this foam. Now, with the information in Fig. 3.11, we can become more precise. Knowing the bubble volume V_b and the channel width w, we can approximate the topology To by the ratio:

$$To = \frac{w}{\sqrt{V_b/h}}, \tag{3.8}$$

giving the number of bubble diameters $d \simeq \sqrt{V_b/h}$ that fit into the channel width w. For simplicity, the value for To will be rounded to the nearest integer: *e.g.* $To = 1.2$ means an F1 foam. The use of $d \simeq \sqrt{V_b/h}$ assumes isotropical bubbles. So this relation cannot be applied for foams far from equilibrium with very elongated bubbles.

We saw in section 3.1, that bubble volume is a function of liquid fraction only (in the standard case for foam generation, with gas thread break-up confined inside the orifice):

$$\frac{V_b}{V_l} = f(\alpha), \tag{3.9}$$

with $V_l = w_{or}h^2$ and $f(\alpha)$ the power law fit to the volume data in Fig. 3.3. Equations (3.8) and (3.9) can be combined to give the topology as a function of gas and liquid flow rates and geometry:

$$To = \frac{w}{\sqrt{w_{or}h}} f(\alpha)^{-1/2}, \tag{3.10}$$

3.4.2 Comparison with experiments

We can compare the actual foam topology with the predictions by equation 3.10. In Fig. 3.23 we see a good agreement between model and experiment for the classical geometry. The transition between F1 and F2 is predicted at $\alpha_l = 0.097$ and experimentally found to be between $\alpha_l = 0.074$ and 0.11. For the transition from F2 to F3 we predict $\alpha_l = 0.22$ and measure a value between 0.19 and 0.22.

For the modified geometries the model predicts values that are one bubble row too high; except at very low liquid fractions, where F3 is predicted instead of F1. This last deviation can be explained because the F1 foams (see for example Fig. 3.7e) are extremely elongated, so the assumption of foams close to a global energy minimum (isotropic bubbles) is invalid. The error at higher liquid fraction is probably due to the neglecting of the liquid content by equation 3.10. In conclusion, we can say that, for the two cases in which we have tested the model,

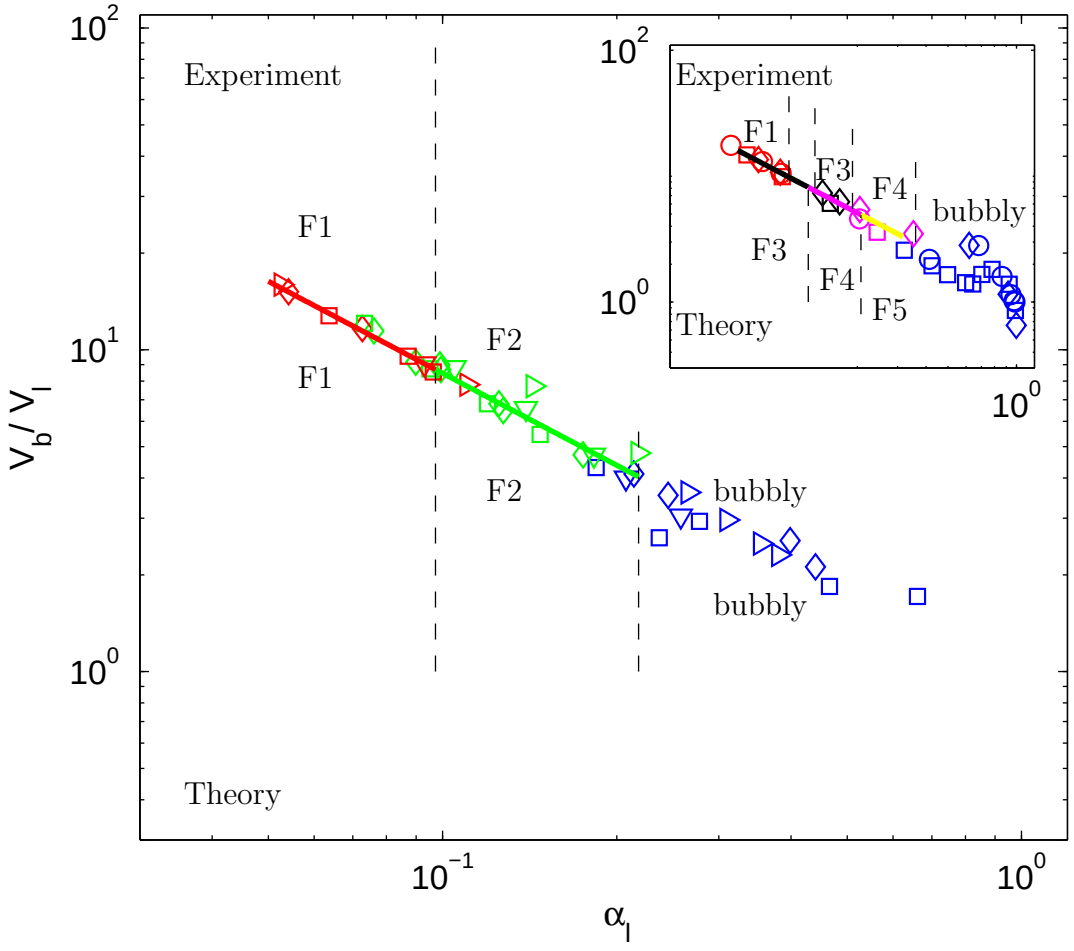

Figure 3.23: Comparison of the actual foam topology with the predictions by the model. Figures show V_b *vs.* α_l for the classical geometry and the modified (insert). Colors indicate the foam topology: F1 (red), F2 (green), F3 (black), F4 (pink), F5 (yellow) and bubbly flow (blue). The color of the continuous line shows the topology predicted by the model.

it gives an approximative prediction, with an uncertainty of 1, of the topologies that can be realised for a given geometry.

3.4.3 Effect of channel width

The prefactor in equation 3.10, $w/\sqrt{w_{or}h}$, gives insight into the dependence of the topology on the geometry. The number of bubbles that fit into the channel width grows for increasing channel width w and decreasing orifice section $w_{or}h$. To verify this claim we will present some, mostly qualitative, results on the influence of channel width w on the foam topology and liquid fraction.

We made three different channels (A.3.1 to A.3.3) with channel width w = 200, 600 and 1000 μm respectively. All other geometrical properties are kept constant. As a consequence, the three different channels have the same natural frequency f_l and bubble volume V_l, allowing for comparison.

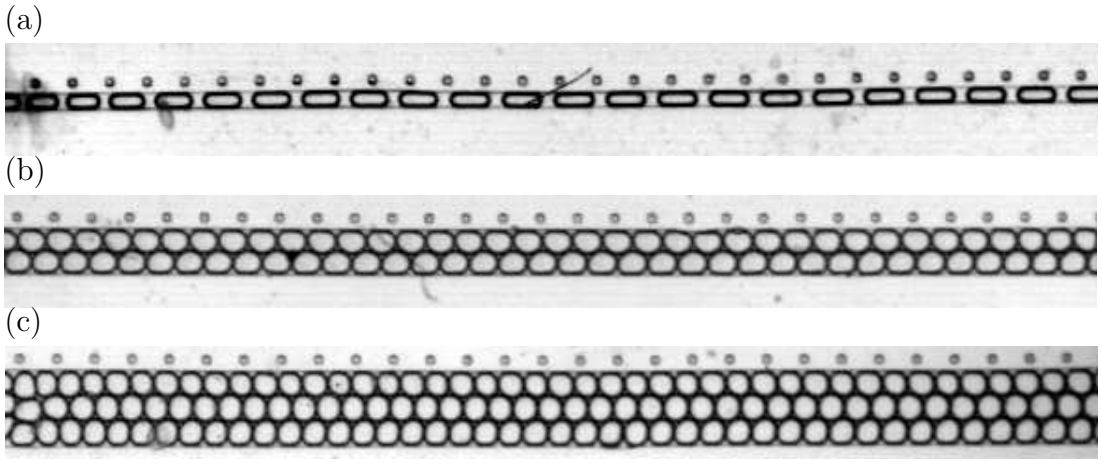

Figure 3.24: Effect of channel width: w = 200 μm (a), w = 600 μm (b) and w = 1000 μm (c). Other geometrical parameters are constant: $h = w_{or}$ = 100 μm and l_{or} = 400 μm.

Following the relation between the gas and liquid flowrate and the bubble volume for confined break-up (Fig. 3.3), equal normalized bubble volume means equal liquid fraction. This can be verified by visual inspection of the pictures in Fig. 3.24, for which bubble volume V_b and liquid fraction are approximately constant. In the above, we have tacitly assumed that we work at sufficiently high liquid flow rate and gas pressure to guarantee a pinch-off confined to the orifice (hence an efficient blocking of the liquid flow by the gas thread).

We can also reason in terms of the topology number *To*. Eq. 3.10 relates foam topology and the gas and liquid flow rates. We claim that the three pictures in Fig. 3.24 have the same α_l. Thus the topology in the different channels should

simply be proportional to the ratio of the different channel widths w:

$$To_n/To_m = \frac{w_n}{w_m}, \tag{3.11}$$

with n and m indicating the two different channel widths under comparison. Note that the $\sqrt{w_{or}h}$ term falls out of the equation because it is constant for the different channels. If we take the widest channel (c) as the reference we find for (b) that $To_b = To_c\frac{w_b}{w_c} = 1.8$, that can be rounded to 2, and for (a) that $To_a = To_c\frac{w_a}{w_c} = 0.6$, rounded to 1. In both cases, these values for To correspond to the actual topology in the channels.

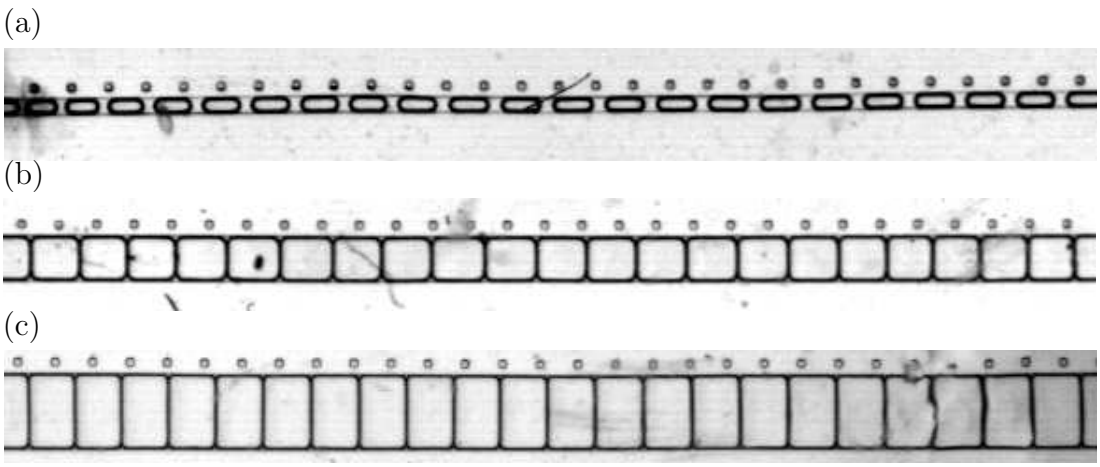

Figure 3.25: For given topology, a foam becomes drier by increasing the channel width. The three channels have a varying channel width: $w = 200$ μm (a), $w = 600$ μm (b) and $w = 1000$ μm (c), and a constant number of bubbles $N_b = 21\pm1$.

Equation 3.10 also implies that for a given topology To, an increase in the channel width w should be accompanied by a decrease in the liquid fraction α_l. This is qualitatively confirmed by the images in Fig. 3.25, where for the same F1 topology ($To = 1$), one can notice a decrease in α_l for wider channels.

The origins of this effect can be understood be assuming that we are in the saturated frequency regime: $f = f_l = Q_l/V_l$. This means that a fixed liquid quantity equal to V_l is dispensed into the channel for every bubble released. Now, if the bubble volume V_b increases, the liquid fraction $\phi_l = V_l/(V_b + V_l)$ will decrease.

3.5 Summary

Here we will give a summary of this chapter that discusses the generation of a microfoam. We have started by presenting the standard case for dry foam formation (section 3.1). For this case we have presented our measurements of

the bubble volume and formation frequency. We have shown that all data for the bubble volume can be normalized by employing a certain volume V_l, related to the orifice geometry. The frequency is found to have two regimes: one at low pressures, where frequencies increase for growing gas pressure, and a high pressure regime where the frequency saturates and only depends on the liquid flow rate.

In section 3.2, we have shown that the dry foam formation regime as shown in section 3.1 critically depends on the position of gas thread pinch-off. The results in section 3.1 correspond to a pinch-off that is completely restricted to the orifice. We have demonstrated two different methods to manipulate this pinch-off position. The first is to work at low liquid flow rates and the second is to employ a channel geometry with an orifice volume smaller than V_l. Both lead to wetter foams for a fixed bubble size, if compared to the standard case.

We devoted section 3.3 to a discussion of the influence of orifice aspect ratio on bubble formation. We have shown (B. Dollet *et. al.* [16]) that bubble break-up does not follow the same mechanism in square and elongated orifices. We have introduced the concepts of 2D and 3D collapse. Both occur in an elongated orifice. In a square orifice only the 3D collapse can take place. We have also discussed why these two different regimes are treated indiscriminately in the preceeding sections of this chapter.

In section 3.4 we have given a rule of thumb for the dependence of the topology that one can generate in the outlet channel as a function of some geometrical parameters. This allowed us to introduce the topology number To, giving the number of bubble rows that fit into the channel width.

They implicit goal of this chapter is to collect enough information so that someone, wanting to build a microfoam generator, will be able to link the channel's geometrical parameters to the desired foam properties (*e.g.* bubble size, liquid fraction, topology).

3.6 Résumé

Ce chapitre est consacré à la génération d'une micro-mousse. Pour commencer, nous avons présenté le cas standard de la formation d'une mousse sèche (paragraphe 3.1). Pour ce cas, nous avons montré nos mesures du volume des bulles V_b et de la fréquence de formation de ces bulles f. Pour des mousses sèches V_b dépend du rapport des débits Q_g/Q_l : la taille des bulles augmente avec le débit de gaz et diminue avec le débit de liquide. Les données pour le volume des bulles peuvent être normalisées avec l'aide du volume de pincement V_l, lié à la géométrie de l'orifice. Pour la fréquence on trouve deux régimes différents : un à basse pression où la fréquence augmente avec la pression du gaz, et un régime à haute pression où la fréquence sature et ne dépend que du débit de liquide.

Dans le paragraphe 3.2, nous avons montré que le regime de formation de

mousse sèche comme on la décrit dans le paragraphe 3.1 dépend de la position du pincement du fil de gaz. Les résultats du paragraphe 3.1 correspondent à un pincement complètement restreint à l'orifice. Nous avons indiqués différentes méthodes pour manipuler cette position de pincement. La première utilise des bas débits de liquide, et la deuxième une géométrie de l'orifice particulière avec un volume plus petit que le volume de pincement V_l. Comparées avec le cas standard, les deux méthodes mènent à des mousses plus humides pour un volume de bulles fixe. Nous avons aussi montré un effet transitoire, ou avec l'aide d'une ligne triple la formation des bulles est restreint à l'orifice, même dans le cas de bas débit de liquide. Nous finissons ce paragraphe avec une comparaison de ces différents régimes de formation de bulles, notamment en comparant la taille des bulles en fonction de la fraction liquide pour les différents régimes.

Paragraphe 3.3 est consacré à une discussion de l'influence du rapport d'aspect de l'orifice sur la génération des bulles. Nous avons montré (B. Dollet *et. al.* [16]) que l'étape de pincement ne suit pas les mêmes mécanismes dans des orifices carrés et dans des orifices rectangulaires élongés. Nous avons introduit les concepts de l'éffondrement 2D et 3D du jet de gaz. Les deux ont lieu dans un orifice rectangulaire. Dans un orifice carré seulement l'éffondrement 3D peut exister. Nous avons aussi discuté pourquoi nous n'avons pas différencié entre ces deux régimes d'éffondrement dans les paragraphes précédents.

Dans le paragraphe 3.4 nous introduisons une relation approximative pour la dépendance de la topologie générée dans le canal d'écoulement en fonction des paramètres de la géométrie. Cela nous a permis d'introduire le nombre de topologie *To*, qui donne le nombre de rang de bulles dans la largeur du canal en fonction de la géométrie de la taille des bulles.

L'objective implicite de ce chapitre est de rassembler suffisamment de données pour que quelqu'un, souhaitant construire un générateur de micro-mousses, puisse faire le lien entre les paramètres de la géométrie et les propriétés désirées de la mousse (par exemple la taille des bulles, la fraction liquide et la topologie).

Chapter 4

Microfoam flow

We now turn to the flow of a foam in the microchannel after formation. To start we will show that its flow is non-linear, with a power law relation between the gas pressure and flow rate. Then we will see that the interplay between bubble generation and flow in the channel creates a multitude of effects including periodic oscillations in the bubble volume, topology separation and bubble break-up. After that we will show an example of a compressible foam and its possible application as a local pressure sensor. Finally we will show some currently only partially understood cases of very deformed foams,

In this chapter, we will occasionally use the terms gas flow rate and foam flow rate indiscriminately. We will only do so for cases with $Q_l << Q_g$ hence the foam flow rate $Q_{foam} = Q_g + Q_l \simeq Q_g$. Furthermore, consistent with literature we will treat the gas pressure as a function of the gas flow rate. In the figures hower, the pressure will be on the x axis as it is the experimental control parameter.

4.1 Flow-rate *vs.* pressure drop

We measure the gas flow rate Q_g as a function of the applied gas pressure drop P_g. A typical example is shown in Fig. 4.1a. We observe a non-linear response in the gas flow rate. We find: a threshold (section 4.1.1), a non-linear slope (section 4.1.2) and a discontinuity upon the transition from an alternate to a bamboo foam (treated in section 4.2). The above effects will be illustrated with the data obtained in channel A.1, already used to discuss the bubble volume and bubbling frequency in sections 3.1.2 and 3.1.3.

4.1.1 Pressure threshold

Fig. 4.1 shows a threshold in pressure for the establishment of bubbly flow. For gas pressures below this value no gas will flow. We determine it in three different ways:

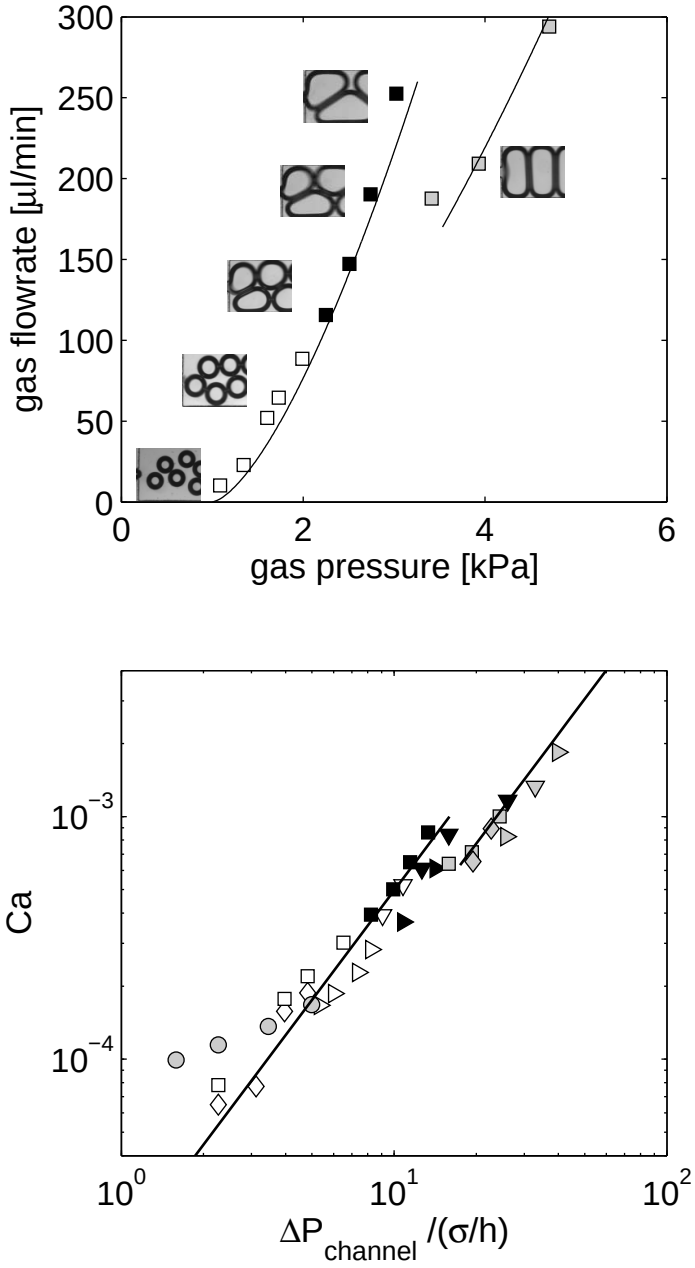

Figure 4.1: (a) Gas flow rate Q_g *vs.* gas pressure P_g for $Q_l = 20\ \mu\text{l min}^{-1}$. Symbol color indicates the topology: bubbly flow (open), two row (black) and bamboo (gray symbols). (b) Same graph with data for different liquid flow rates: $Q_l =$ (o) 4, (□) 20, (▷) 30 and (▽) 40 μl min^{-1}. Axes are logarithmic and rescaled by $Ca = \mu Q_g / S\sigma$ and $\Delta P_{channel} = P_g - P_c$ in units of σ/h. For unknown reasons the data for $Q_l = 4\ \mu\text{l min}^{-1}$ diverges. The solid lines on both plots are fit to data on alternate and bamboo foams at $Q_l = 20\ \mu\text{l min}^{-1}$ with the power law $Ca = \beta^{-1} \left(\Delta P_{channel}/(\sigma/h)\right)^{3/2}$, with $\beta = 1.7 \times 10^3$ (alternate) and $\beta = 2.5 \times 10^3$ (bamboo).

- a power law fit to the data in 4.1b: $P_c = 1.0 \pm 0.1$ kPa
- a calculation of the capillary (Laplace) pressure, eq. (3.1), $P_c = 1.1 \pm 0.2$ kPa
- a visual inspection of Fig. 3.1 (at high Q_l), $P_c = 0.9 \pm 0.15$ kPa

These three values are equal within error bars, indicating a static origin independent of the liquid flow rate.

In presence of a second constriction, consisting of a PDMS lump in the outlet channel (data not shown), we obtain for the bubbly and alternate regimes the same result as in Fig. 4.1b, translated by about 0.45 kPa along the P-axis. The gas pressure increase is compatible with the expected Laplace pressure necessary to overcome the second constriction, 0.6 kPa. This confirms that the threshold is induced by capillary effects.

We cannot compare the bamboo regimes for the case with and without obstacle because the constriction led to bubble break-up (similar to the geometry mediated break-up in [42] and section 5.1) thereby changing the bubble size and topology after the obstacle.

4.1.2 Dissipation in the channel

We write the total pressure drop as the sum of two contributions,

$$P_g = P_c + \Delta P_{channel}\left(Q_g\right), \tag{4.1}$$

where P_c is the static orifice contribution and $\Delta P_{channel}\left(Q_g\right)$ is due to dynamic dissipation in the channel.

Compared to a Newtonian flow whose drag pressure grows proportionally to the flow rate, here the drag pressure grows with a lower exponent of the flow rate. It can be interpreted by assuming that dissipation mainly occurs in the liquid films, close to the walls (wall films and wall Plateau borders). These lubrication films thicken when flow rates increase, a phenomenon described first by Bretherton in [7], for the motion of a single bubble in a capillary tube establishing a relation of the form

$$\Delta P_{channel} \sim Ca^{2/3}. \tag{4.2}$$

The capillary number is defined as:

$$Ca = \mu v/\sigma. \tag{4.3}$$

containing the bubble velocity v (estimated as $v \simeq Q_g/S$ in the dry foam state) and liquid (soap solution) viscosity μ. In our case Ca is of order $10^{-4} - 10^{-3}$.

Plug flow model for foams

Cantat and co-workers extended the Bretherton result for a single bubble or bubble train to more complicated foam structures:

$$\Delta P_{channel} = \overline{\lambda}\frac{nL^p}{S}\sigma Ca^{2/3}, \tag{4.4}$$

with n the total number of bubbles in the channel, L^p the projection on the cross section of the wetting perimeter per bubble (length of the wall Plateau border, projected on a section of the channel, Fig. 4.2), S the channel cross section area, and $\overline{\lambda}$ a dimensionless numerical constant [9]. The model has the same exponent as the classical Bretherton case: $\Delta P_{channel} \sim Ca^{2/3}$, but with a prefactor $\overline{\lambda}\frac{nL^p}{S}\sigma$.

In this model, $\overline{\lambda}$ decreases with the liquid fraction [9]: a dry foam resists more to flow than a wet foam, because the liquid films are thinner; this implies higher velocity gradients in these films, and thereby higher dissipation.

The nL^p term in the prefactor is related to the foam structure. One of the main assumptions of this model is that the principal source of dissipation for foam flow in a channel is the sliding of the liquid films between bubbles over the channel walls (see section 1.2.2) (films indicated in red in Fig. 4.2). Channel resistance scales with the total length of these films in the channel. Orientation plays an important role. For a film of length L the relevant length scale is the projected length $L^p = L\cos\alpha$ with α the angle between the normal vector of the film and the flow direction (Fig. 4.2 blue lines). nL^p now represents the total film length in the channel over which dissipation takes place. We shall see in section 4.2 that this concept of dissipation length is usefull to explain observed instabilities in the foam flow.

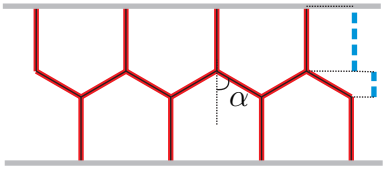

Figure 4.2: F2 foam. Red lines indicate the films between bubbles and the wall Plateau borders where these films touch the channel walls. According to the plug flow model, sliding of these wall Plateau borders over the channel walls is the dominant source of dissipation in foam flow. Blue lines show the projection of these films on the channel cross section.

Application to our experiments Equation 4.4 was introduced for the case of a foam with constant properties (liquid fraction, bubble size and topology) that can be moved at different velocities by varying the pressure exerted on it.

Our case is more complicated because we cannot dissociate foam formation from flow.

- As the gas pressure increases, not only the foam flow rate but also the bubble volume increases (see *e.g.* Fig. 4.1). This effect will modify equation 4.4. An increase in bubble size will diminish the number of bubbles n in the channel. As we will see in section 4.2, a change in bubble size will also change L^p.

- Increasing bubble volume can lead to a topology transition, in the case of Fig. 4.1 from bubbly to alternate to bamboo. A topology transition will also induce a variation in L^p.

- An increasing foam flow rate Q_g will lead to drier foams and thereby to an increasing $\overline{\lambda}$.

- The model assumes a flow of bubbles in an otherwise static liquid (see Fig. 1.8). This leads to the central assumption that dissiption is confined to the wall Plateau borders, where liquid is entrained by the sliding of foam films over the channel walls. The liquid in wall films is supposed to be static. Our system has the particularity that the liquid is not static or only entrained by the bubble motion but actively pushed at a fixed flow rate.

It is beyond the scope of this work to develop a model especially adapted for foam flows in flow-focusing systems. We will use equation 4.4, while aware of its limits.

We fit equation 4.4 to both the alternate and the bamboo regime in Fig. 4.1b, $\Delta P_{channel}/(\sigma/h) = \beta\, Ca^{2/3}$ with $\beta = 1.7 \times 10^3$ (alternate) and $\beta = 2.5 \times 10^3$ (bamboo). With the value of β and L^p (that depend both on bubble size and topology), we deduce for the numerical constant the value $\overline{\lambda} = 22 \pm 5$. That is comparable to the value $\overline{\lambda} = 38 \pm 4$ found in the millimetric channels with a comparable aspect ratio studied by [9].

Value of the exponent A second *caveat* should be mentioned with respect to the exponent in the relation $\Delta P_{channel} \sim Ca^{2/3}$. The value of this exponent is currently a subject of hot debate [9, 60, 12, 13, 14, 52]. Values between 1/2 and 2/3 have been reported for various experiments. The value of the exponent seems to be closely related to the area where dissipation takes place. Theoretical predictions indicate an exponent 1/2 in the case of dominant dissipation in the wall films. An exponent 2/3 is found, if dissipation in the wall Plateau borders is dominant. The region where dissipation takes place is related (but **not** completely determined [13]) by the choice of the surfactant: a rigid monolayer of surfactant favors dissipation in the films while a mobile layer leads to dissipation in the Plateau borders [12]. Application of these results on experiments stays

cumbersome. Some experiments even seem to discard the capillary number $Ca = \mu v/\sigma$ as the proper physical quantity. Dollet found a different exponent for v and μ in the case of foam flowing in a 2D configuration between a glass plate and a liquid pool [14].

We vary the pressure P_g and Ca both over approximately one decade (Fig. 4.1b). This is enough to observe a power law, but not to determine the exponent. The 2/3 exponent seems compatible with our experiments. Furthermore, we will see, in section 4.2, a multitude of effects that can be explained by assuming a scaling of the dissipation by L^p and not by wall films. This suggests that dissipation in the Plateau borders dominates, thus justifies the choice of 2/3 for the exponent. We have not measured the surface viscoelastic properties of our liquid solution to discern between liquid or solid surfactant layers.

Note that in our case the value of the exponent is not of decisive importance for the rest of this chapter. Because we only vary pressure over one decade, the different exponents give comparable results.

Influence of the liquid fraction and of the bubble size In a follow-up article to [9] (in which equation (4.4) was introduced), Cantat and co-workers investigated the influence of the liquid fraction and the bubble size on the viscous force, that opposes the pressure drop, for a bamboo foam [60]. They introduce the dimensionless parameter r/L giving the ratio between wall Plateau border thickness and distance between wall Plateau borders (see Fig. 4.3 for their definition).

A theoretical analysis for the flow of a bamboo foam in an axisymmetric channel using the lubrication approximation, leads to the following relation for the viscous force per unit Plateau border length:

$$f_v = \sigma \left(\frac{r}{L}\right)^{-2} F\left(\left(\frac{r}{L}\right)^3 Ca\right), \tag{4.5}$$

with $F(\xi)$ an unknown function of $\xi = (r/L)^3 Ca$. For their experiments in millimetric channels and with foam speeds around 1 mm/s they find the phenomenological scaling $F(\xi) = (3.8 \pm 0.2)\xi^{0.56\pm0.02}$, indicating an increase of f_v for larger bubbles (larger L) and for drier foams (smaller r). In general F is supposed to depend on the parameter range for ξ (related to the foam speed by Ca and structure by r/L) and the boundary condition at the gas-liquid interface (fluid or rigid).

In general, for exponents between the extremes of 1/2 and 2/3, there will be a dependence on r/L with the viscous force increasing for larger bubbles and drier foams. For $F(\xi) = \lambda\xi^{2/3}$ equation 4.5 becomes $f_v = \lambda\sigma Ca^{2/3}$, that corresponds to equation 4.4 for a bamboo foam. Note that it indicates that in this case f_v should be independent of the liquid fraction. For the other extreme of $F(\xi) \propto \xi^{1/2}$, we find $f_v \propto \sigma(LCa/r)^{1/2}$. This implies that in general, for intermediate values of

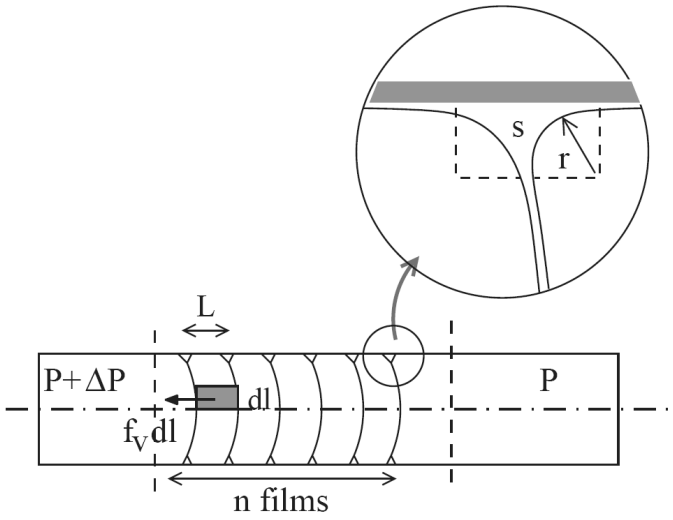

Figure 4.3: Axysymmetric bamboo bubble train: schematic view and definition of the parameters. The bubble train is submitted to a pressure drop ΔP that is balanced by a total viscous force $F_v = n \oint f_v \mathrm{d}l$. Liquid films between bubbles are a distance L apart. All liquid is supposed to be in the Plateau borders where films between bubbles touch the wall that can be characterized by its radius r. From Terriac *et. al.* [60].

the exponent, dissipation is not completely restricted to Plateau borders but does also take place in the films between a bubble and the channel wall.

A direct comparison of our experimental results with equation 4.5 is impossible, even for bamboo foams for two reasons.

- First, in the axisymmetric case studied in [60], all the liquid is contained in wall Plateau borders with radius r. In our case, most of the liquid rather flows in the corner section of the channel.

- Second, the theoretical model in 4.5 predicts a small backflow of liquid in the films surrounding bubbles, with a direction opposite to the foam flow. In our case, we force a liquid flow in the same direction as the foam flow.

We will show that the discontinuities in the viscous force, that we will discuss in section 4.2, occur upon discontinuities in the Plateau border length, and this for unchanged film area between bubbles and the wall. This is not enough to state that in our case dissipation is completely restricted to Plateau borders, but we can say that it is dominant.

4.2 Discrete effects: topology transitions

The structure transition from an alternate to a bamboo foam induces a discontinuous decrease of the gas flow rate (Fig. 4.1). This is a signature of the discrete character of the foam: we find by image analysis that the transition to the bamboo structure is associated with an increase of the projected length L^p of 50 %. This is consistent with the observed increase of $\Delta P_{channel}$ by 50 %, considering equation 4.4 that states that $\Delta P_{channel}$ is proportional to nL^p. We conclude that the rearrangement of bubbles induces the discontinuity in the pressure drop.

The present discontinuity is a manifestation of a much wider range of phenomena related to a topology transition and the accompanied discrete change in L^p. We will devote this section to these phenomena.

In the following we will approach the influence of L^p in a more quantitative way. We shall also discuss the link between bubble volume and topology transitions (section 4.2.1). The combination of both elements, L^p and topology transitions, will help us to explain a series of instabilities where, although the control parameters P_g and Q_l are constant, bubble volume, speed and topology can vary (section 4.2.2).

4.2.1 Energy and drag length for different topologies

So far we obtained L^p by image analysis, by measuring the wall Plateau border length between vertices. For a known bubble volume and topology, L^p can also be derived analytically, for an ideally dry foam, using geometrical considerations and Plateau's law stating that three films will meet under an 120 °C angle:

$$L^p_{F1} = 2w, \tag{4.6}$$

$$L^p_{F2} = \left(1 + \frac{1}{\sqrt{3}}\frac{V_b}{hw^2}\right) w, \tag{4.7}$$

$$L^p_{F3} = \left(\frac{2}{3} + \frac{2}{3}\sqrt{3}\frac{V_b}{hw^2}\right) w, \tag{4.8}$$

$$L^p_{F4} = \left(\frac{1}{2} + \sqrt{3}\frac{V_b}{hw^2}\right) w. \tag{4.9}$$

L^p_{F1} is simply twice the channel width (see Fig. 4.4a), for topologies F2, F3 and F4, the projected film length increases with bubble volume (Fig. 4.4b). Note that we assume perfectly dry foams. For wetter foams, wall vertices, where one Plateau border and two wall Plateau borders meet, swell, thereby reducing the film length that should be taken into account [9].

The dominant force in a foam is surface tension, tending to minimize bubble surface for given bubble volume. In a 2D geometry like ours, we can represent bubbles by their area $A = V_b/h$ as we see it appear on our images. Minimization

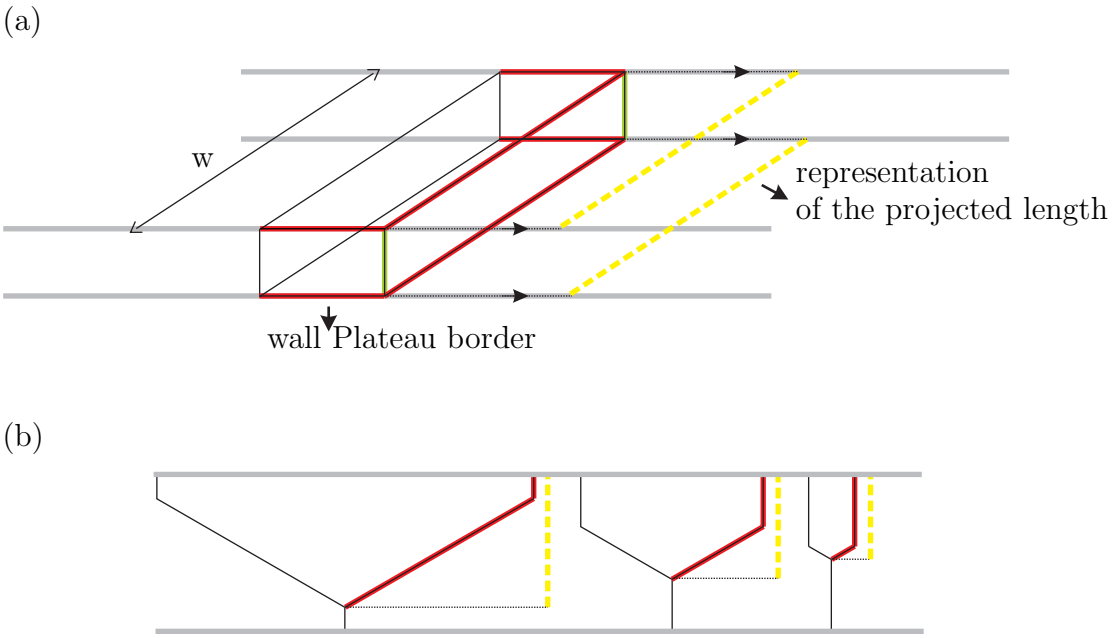

Figure 4.4: Film length per bubble projected on the direction normal to flow. (a) An F1 bubble. $L^p = 2w$ (yellow lines). We neglect the Plateau borders on the channel's side walls (green lines) because of our very low aspect ratios ($h << w$). (b) F2 structure (top view). L^p depends not only on topology but also on V_b. Note that nL^p should give the total projected film length in the channel. Therefore for films that are shared between two bubbles only half the number of films should be taken into account (red lines).

of the interfacial energy now reduces to minimizing the bubble perimeter for given projected surface area. The bubble perimeter L is also a function of bubble volume and topology. It is proportional to the interfacial energy, $L \propto E$, and can be determined analytically:

$$L_{F1} = 1 + 2\frac{V_b}{hw^2}, \tag{4.10}$$

$$L_{F2} = \frac{1}{2} + (2 + \frac{1}{2}\sqrt{3})\frac{V_b}{hw^2}, \tag{4.11}$$

$$L_{F3} = \frac{1}{3} + (2 + \sqrt{3})\frac{V_b}{hw^2}, \tag{4.12}$$

$$L_{F4} = \frac{1}{4} + (2 + \frac{3}{2}\sqrt{3})\frac{V_b}{hw^2}. \tag{4.13}$$

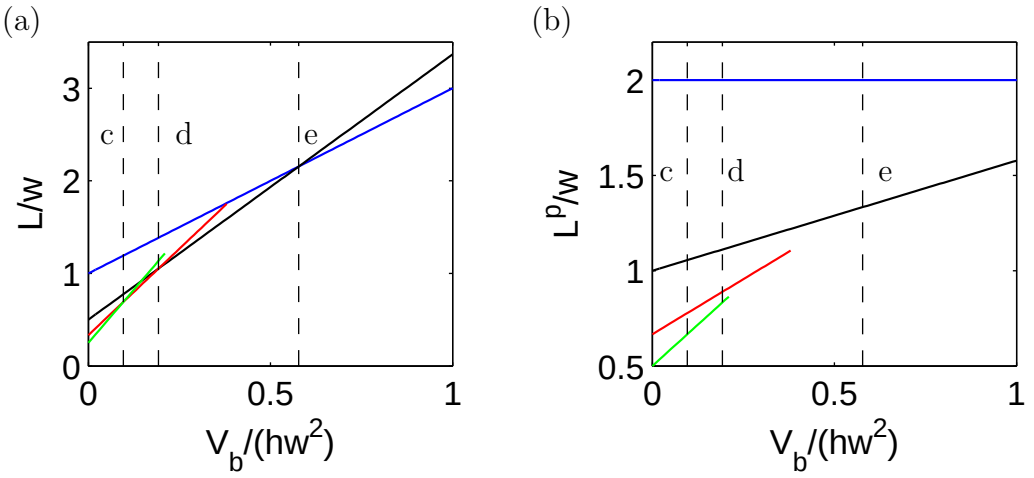

Figure 4.5: Bubble perimeter L (a) and projected film length L^p (b), *vs.* the bubble volume. For increasing bubble volume, the energetically most favorable topology changes from F4 (green), to F3 (red) to F2 (black) F1 (blue). The dashed lines indicate the bubble volume for which this crossover takes place: (c) F4 to F3, $V_b/hw^2 = \sqrt{3}/18 \approx 0.10$, (c) F3 to F2, $V_b/hw^2 = \sqrt{3}/9 \approx 0.19$, (c) F2 to F1, $V_b/hw^2 = \sqrt{3}/3 \approx 0.58$. At every crossover the channel resistance, represented by L^p, increases discontinuously.

In Fig. 4.5 we plot both the bubble perimeter L and the projected film length L^p *vs.* the bubble volume V_b. For increasing bubble volume, a configuration with less and less bubble rows becomes favorable. This leads every time to a discontinuous increase in L^p and thereby in the channel resistance. Each topology can be realised up to a maximum bubble volume: $V_{b,max}^{F2} = \sqrt{3}hw^2$, $V_{b,max}^{F3} = \frac{2}{9}\sqrt{3}hw^2$ and $V_{b,max}^{F4} = \frac{1}{8}\sqrt{3}hw^2$. Larger volumes would violate Plateau's law.

Therefore we can state that for all possible bubble volumes $L^p_{F1} > L^p_{F2} > L^p_{F3} > L^p_{F4}$. The ratio in channel resistance L^p_{Fi}/L^p_{Fi+1} decays with the number of bubble rows in the channel: at the cross over for which Fi and Fi+1 represent an equal bubble perimeter, the ratio of projected film lengths is $L^p_{F1}/L^p_{F2} = 1.5$, $L^p_{F2}/L^p_{F3} = 1.25$ and $L^p_{F3}/L^p_{F4} = 1.17$. So we expect the discontinuity to be the most pronounced at the F1-F2 transition.

4.2.2 Transition from alternate (F2) to bamboo (F1) foam

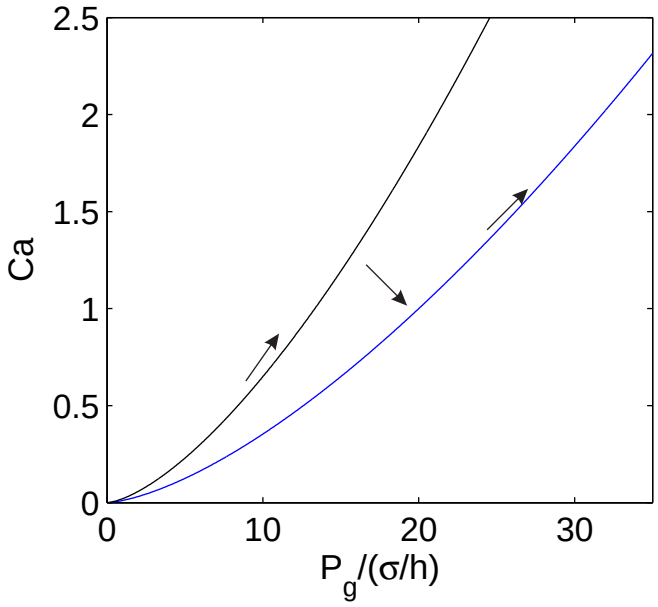

Figure 4.6: Pressure *vs.* flow rate following equation 4.4 (Cantat theory) for the F2 (black) and F1 (blue) structure. The bubble volume $V_b = \sqrt{3}/3hw^2$, the volume at which F1 and F2 are energetically equally favorable. We take $n = 10$ bubbles in the channel and $\overline{\lambda} = 1$. In our system, the bubble volume grows for increasing gas pressure. To minimize its interfacial energy the foam will transit from the F2 curve to the F1 (arrows indicate a possible trajectory).

For a given bubble volume, the bubble arrangement in the bamboo structure will always lead to a higher friction than in the alternate structure. As the bubble volume grows, the system will transit from F2 to F1. This means bridging the gap between both P_g-Q_g curves in Fig. 4.6. We will show the existence of three different transition mechanisms: (A) periodic oscillations between the two topologies, (B) topology coexistence for which the channel is divided in two parts, each with a distinct structure, and (C) a third regime showing a mix of oscillation

and separation. In the following we will present these three mechanisms and the conditions for which they occur.

A) Periodic topology oscillations

Here we present a case (for channel A.3.3) where for constant Q_l there is a range of P_g's in the transition region from F2 to F1, for which the topology will oscillate. This is accompanied by an oscillation in the bubble volume and gas flow rate over more than a factor 2 in the present example. We will first describe this phenomenon, by detailing one example at fixed Q_l and P_g. Then we will model it using equation 4.4 to link the volume of a newly formed bubble at the channel entrance to the structure of the foam still present downstream. Finally we will try to understand these oscillations in the framework of the instability caused by a discontinuity in L^p.

A typical cycle (Fig. 4.7a) starts with an F2 foam. See Fig. 4.7b. The flow rate grows, and at the same time the bubble volume V_b of newly formed bubbles at the orifice increases. This increase is followed by a transition of the foam topology in the channel from two rows to one row of bubbles (F2 to F1 foam, see Fig. 4.7c. Then the foam slows down while the bubble volume at the entrance is shrinking (Fig. 4.7d. This is followed by another transition, this time from F1 to F2 (Fig. 4.7e. When the last F1 bubbles are evacuated from the channel a new cycle starts. Over the whole cycle the bubble formation frequency $f = 1/T$ stays constant: we are in the saturated frequency regime described in section 3.1.3 for which f only depends on the liquid flow rate Q_l. Therefore there is a linear relation between the volume of a newly formed bubble and the velocity v at which the foam flows: $V_b = Q_g\, T = v\, S\, T$. Velocity is homogeneous over the channel. Image analysis shows no compressibility effects for the gas bubbles, in agreement with the small values of the pressure (typically a few kPa). The foam behaves like a plug flow.

The oscillating behaviour occurs only in an intermediate range of driving pressure P_g around the transition from F2 to F1. For a slightly lower driving pressure, we observe a monodisperse F2 foam. A slightly higher pressure leads to a monodisperse F1 foam (see Fig. 4.8). We stress that the bubble formation process itself is stable while the flow is not. We are in the high-pressure regime where the gas-water interface stays in the orifice after pinching off. Non-linearities due to rapid gas-water interface retraction upstream of the orifice after bubble pinch-off like in [27] do not play a role. Pinch-off is stable, both in periodicity and spatial position.

A key element for the understanding of the oscillation is the topological transition from F1 to F2, and *vice versa*. As we have said already, the dominant force in a foam is surface tension, tending to minimize bubble surface for a given bubble volume. It is known that a foam is usually stuck in a local energy minimum an does not reach the global minimum [66]. The method used for the preparation

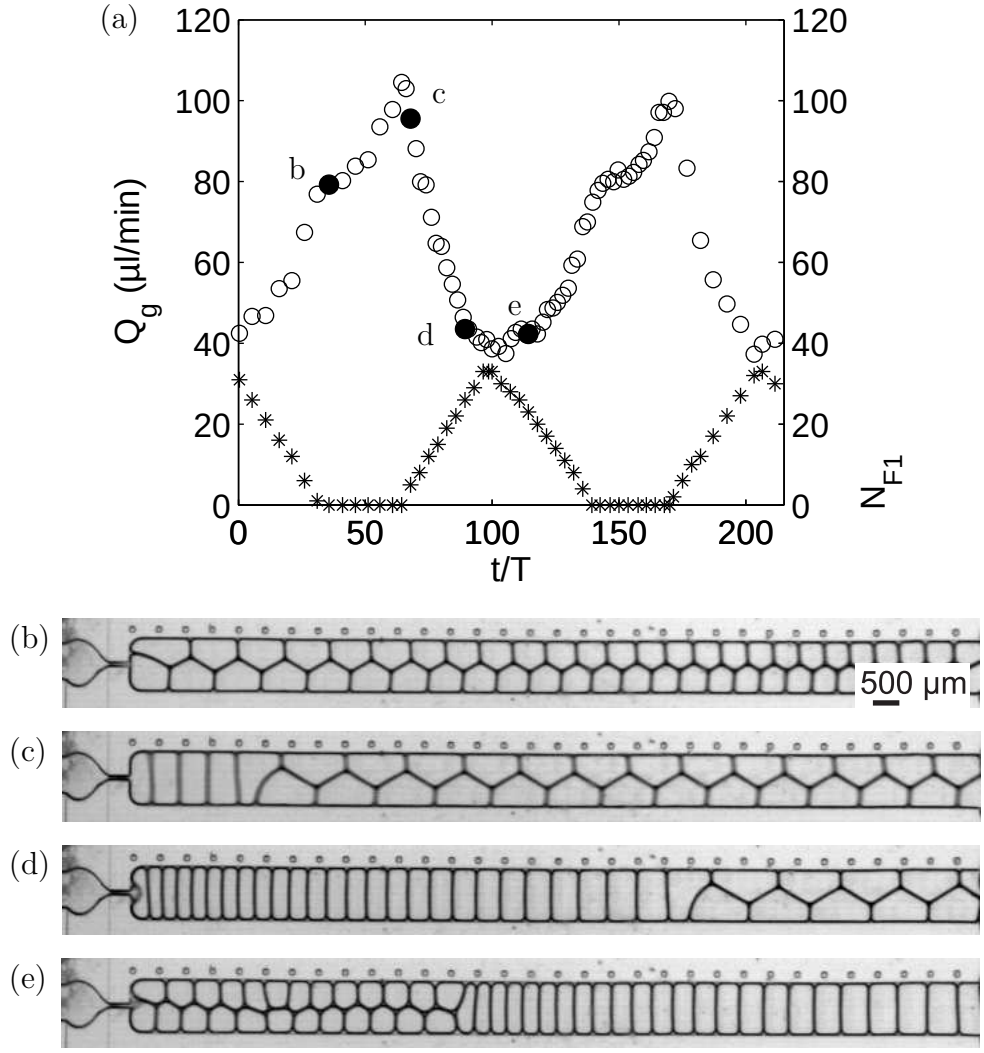

Figure 4.7: Case A: spontaneous periodically oscillating foam, with $Q_l = 4$ μl/min and $P_g = 2.90$ kPa. (a) Gas flow rate Q_g (circles) (μl/min) oscillates over a factor 2.8 in time t (non-dimensionalised using the bubbling period T). Foam topology oscillates between two states: F2 and F1. The number n_{F1} of F1 bubbles (stars in a) is inversely correlated with Q_g. (b) F2 topology. Increasing bubble size. (c) Transition from F2 to F1 topology. (d) During F1 formation bubble size decreases. (e) Transition from F1 to F2.

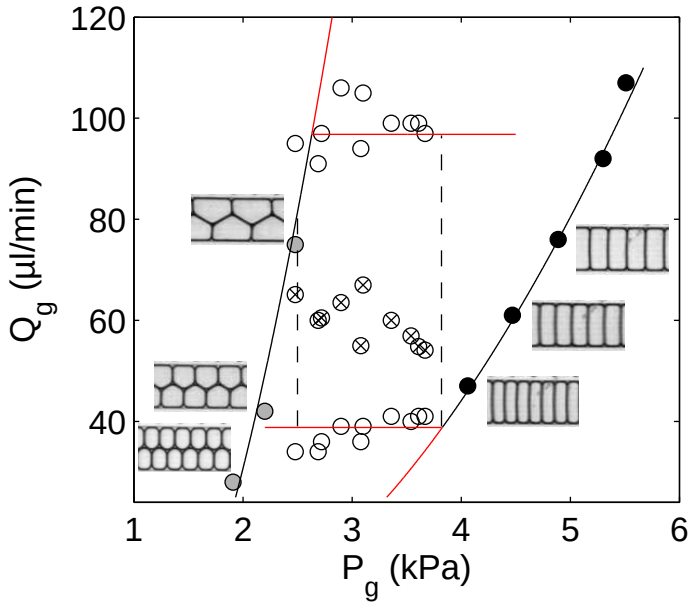

Figure 4.8: Case A: foam flow rate and type (stable or oscillating) as a function of the applied pressure. For increasing pressure the foam topology changes from stable F2 (gray symbols) to an oscillation between F2 and F1 (open symbols). Increasing even more the pressure leads to stable F1 foams (black symbols). In the intermediate oscillating region open symbols indicate maximum and minimum foam flow rates, crossed symbols indicate the average flow rate. The liquid flow rate was kept constant at $Q_l = 4$ μl/min. The continuous lines are guides for the eye.

of the foam is the determinant factor. This also holds in our case where the same bubble volume V_b can be arranged in an F2 and an F1 foam. Furthermore the very elongated F1 bubbles are obviously far from minimising their surface to volume ratio. The formation process in this confined geometry plays an important role.

We explain the topology selection mechanism by the interplay between bubble formation at the orifice and the shape of the preceding bubbles. We will discuss first F1 and F2 formation, before describing transitions. In the case of the bubble formation for an F1 foam, the new bubble will first form a circular shape centered around the orifice (see pictures in Fig. 4.10 a). Two three-fold wall vertices form at the points where the wall, the new bubble and the preceeding one meet. These vertices slide over the channel walls. The F2 formation is a bit more complex (see Fig. 4.10 b). Here again formation of a bubble starts with a circular cap, with a wall vertex on each side. Because of the inherent asymmetry of an F2-foam the distance between these two wall vertices and the preceding ones is not the same on either side of the channel. Between the two wall vertices at shortest distance a wall T1-transition (bubble neighbour switching [48], see Fig. 4.9) takes place allowing the newly formed foam to relax to the F2 state.

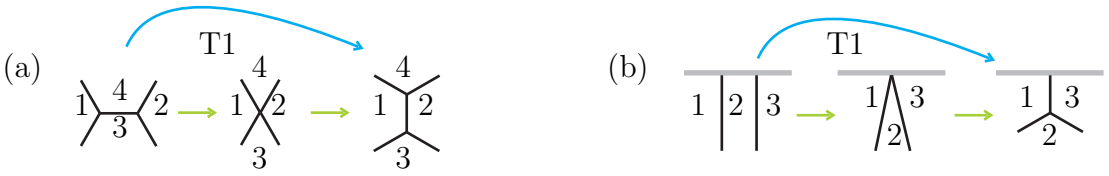

Figure 4.9: Bubble neighbour switching ("T1"). (a) Bulk (normal) T1. Initially 1 and 2 are neighbours, after an instable intermediate state in which four films meet, 3 and 4 become neighbours. (b) Wall T1. Bubble 2 is initially touching the wall. After the T1, 1 and 3 become neighbours.

The transition from F2 to F1 takes place when the volume V_b of the new bubble becomes that large that the inter-vertex distance is too large to allow a T1 (see Fig. 4.10c). We will call this volume V_{21}: the threshold volume for transition from F2 to F1. The opposite transition takes place at a much smaller bubble volume because of the absence of preexistent asymmetry: bubble volume has to reduce a lot (smaller than V_{21}) before the inter-vertex distance is that small that the situation becomes unstable, that one of the wall vertices slides faster, triggers a T1 upon contact with the previous film, thereby completing the transition (4.10d). The source of the instability creating the transition from F1 to F2 is unknown to us. It probably depends on an attractive interaction between to films, for an intervertex distance below a critical minimum.

For our channel geometry the transition F1 to F2 takes place at $V_{12}/hw^2 = 0.22 \pm 0.02$ and the inverse at $V_{21}/hw^2 = 0.56 \pm 0.02$. Our analysis of bubble

perimeter as a function of topology indicated a crossover at $V_b/hw^2 = \sqrt{3}/3 = 0.58$, the volume below which F2 is energetically favorable and above which F1. This point coincides with V_{21}. For a topology transition to take place it must be energetically favorable and also possible with respect to the bubble formation mechanism. This second condition,that we do not completely understand at this moment, leads to a large hysteresis between V_{12} and V_{21} (a factor 2.5 between these two volumes). The confinement in the channel does not allow the F1 structure to transit to F2, although $V_b/hw^2 < 0.58$, for volumes larger than $V_{12}/hw^2 = 0.22 \pm 0.02$. The difference in transition bubble volume probably depends heavily on the liquid fraction as this is the determinant factor for the vertex distance at which a T1 rearrangement is triggered [48, 51]. Therefore we expect that the amplitude of the oscillation will be less pronounced for wetter foams.

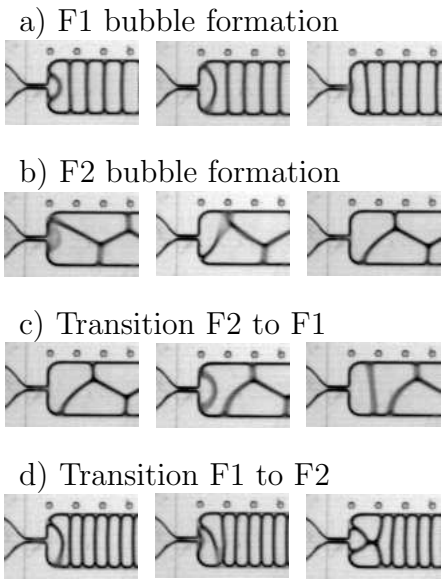

Figure 4.10: Case A: formation of the foam topology F1 (a) and F2 (b), and the transitions F2 to F1 (c) and F1 to F2 (d).

We model the oscillating behavior by linking foam topology and rheology. Driving pressure P_g is related to foam velocity v by the channel resistance to flow (dissipation). The foam speed is oscillating for constant driving pressure, therefore the channel resistance must oscillate as well. We can again write equation 4.4:

$$\Delta P_{channel} = \frac{\overline{\lambda}}{S} \sum_{i=1}^{n} L^p(i) \sigma Ca^{2/3}, \tag{4.14}$$

Knowing the bubble volumes and structure in the channel, with the analytical expressions for L^p_{F1} and L^p_{F2} (eqs. 4.6 and 4.7) we can sum the projected lengths

of all the bubbles in the channel. We obtain the total resistance prefactor, and hence the capillary number Ca (and gas flow rate Q_g) at a given applied pressure drop, from equation 4.14.

To model the foam flow we proceed in the following way. The bubble formation period T being constant whatever the bubble size, we predict the volume of the new $(n+1)$th bubble, at a given discretized time $t/T = n$, to be $V_b^{(n+1)} = Q_g^{(n+1)}\, T$. Using equation 4.14, we obtain the gas flow rate $Q_g^{(n+1)}$ as a function of the n_b bubbles downstream in the channel, and thus the next bubble volume, from

$$\overline{V_b}^{(n+1)} = \frac{1}{Ca_T}\left(\frac{2\overline{P}}{\overline{\lambda}\,\overline{R^n_{total}}}\right)^{3/2}, \tag{4.15}$$

with the following dimensionless quantities: $\overline{V_b} = V_b/hw^2$ the bubble volume, $\overline{R^n_{total}} = \sum_{k=n-n_b}^{n} L^{p(k)}/w$ the total resistance of the films, $Ca_T = \mu w/\sigma T$ and $\overline{P} = \Delta P_{channel} h/2\sigma$ the experimental parameters related to bubbling period and pressure. The sum of the projected lengths $\overline{R^n_{total}}$, takes into account the n_b bubbles in the channel.

To close the model, we enforce foam topology transitions at the experimentally observed values of the bubble volumes V_{12} and V_{21}. Essentially we calculate $\overline{V_b}^{(n+1)}$ by numerical integration over all the bubbles in the channel. Therefore a bubble influences the volume of its successors during its presence in the channel, while travelling from the orifice to the channel exit. This creates a retroaction of flow on generation. A comparison between experiment and model is shown in Fig. 4.11: it confirmes that we capture a large part of the essential of the physics. The model reproduces the oscillation frequency, the gas flow rate and number of bubbles in the channel correctly.

We can now interpret the topology oscillations as the result of an interaction between foam energy and dissipation. The black lines in Fig. 4.8 indicate a stable situation for which the exerted pressure gradient is balanced by dissipation. If we increase P_g, starting from a stable F2 situation, beyond the threshold for oscillations, the system will try to reach the stable theoretical positions indicated by the red lines in Fig. 4.8. It cannot attain these positions however, due to the structure transition to F1, that will take place beforehand. The F1 foam that now gradually starts filling the channel dissipates more than the previous structure. This leads to a disbalance between pressure gradient and dissipation: the flow rate decreases. The gas flow rate corresponding, at this pressure, to a stable flow, is again below the flow rate for which the F1 structure is energetically less favorable than F2 **and** for which it can transit to F2. This transition to the less dissipating F2 structure again creates a disbalance between pressure gradient and dissipation, leading to an acceleration, and so on.

For the pressure interval corresponding to oscillations, the foam flow rate averaged over time decreases slightly with P_g (Fig. 4.8). This corresponds to topology oscillations that are increasingly dominated by the F1 topology.

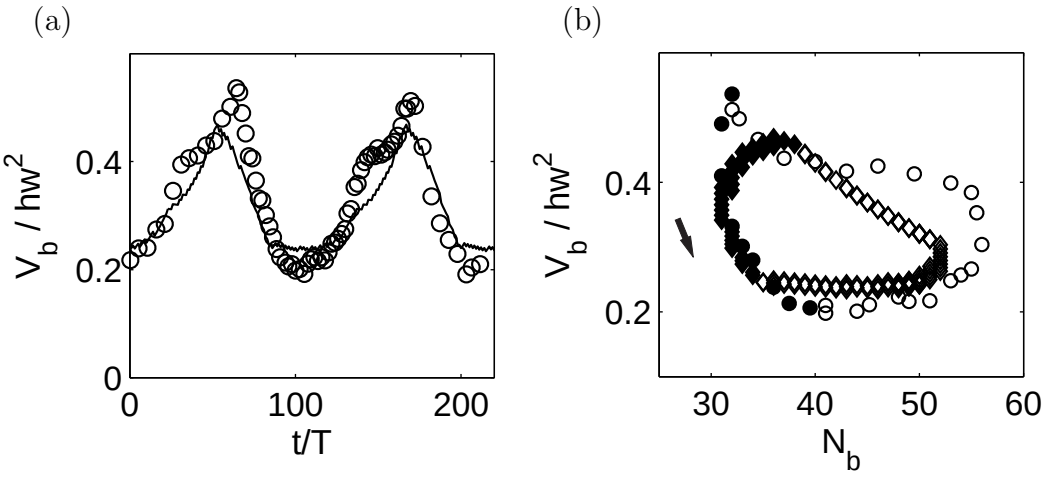

Figure 4.11: Cas A: comparison between experimental data (circles) and the model (continuous line) (a) for the bubble volume V_b at the entrance of the channel. Time is normalised by the bubbling period T. (b) Bubble volume against the total number of bubbles in the channel n_b. ($\diamond$): model, (o): experiment. Filled symbols indicate that newly formed bubbles form an F1 topology, open symbols the generation of F2. Parameters: $\overline{\lambda} = 67$, $\overline{Ca_T} = 8.9\ 10^{-4}$, $\overline{P} = 8.2$, $V_{12}/hw^2 = 0.25$, $V_{21}/hw^2 = 0.45$. $\overline{\lambda}$ was used as a fit parameter, all others are extracted from the experiments. The arrow indicates the direction of the oscillation cycle.

The extent and amplitude of the oscillations is determined by two quantities:

- the ratio of projected film lengths L_p for the two topologies. This ratio, by changing the prefactor in (4.4), controls the distance between the two curves for the (P_g-Q_g) relation. This ratio is purely geometric (if we neglect the small varation of L_p with the liquid fraction as observed in [9]) and constant for our case of low aspect ratio channels, for which films sliding on the sidewalls can be neglected. At aspect ratios closer to unity (square channels) these films on the sidewalls (green lines in Fig. 4.4) have a length comparable to the film length on the top an bottom wall. This film length also changes upon the transition from F1 to F2, thereby increasing the ratio L^p_{F1}/L^p_{F2}, at the bubble volume for which F1 and F2 are energetically equally favorable, from $L^p_{F1}/L^p_{F2} = 1.5$ for very flat channels, to 1.7 for square channels. Note that a change in L^p_{F1}/L^p_{F2} does not influence the oscillation amplitude, but only the extent of the pressure domain for which oscillations will take place.

- the hysteresis between the structure transition V_{21} and V_{12}. This hysteresis sets the limits for the foam flow rate during oscillations. We have not experimentally varied this hysteresis, that should be larger for dry foams. We suppose that a larger hysteresis corresponds to a larger amplitude, but a smaller pressure domain for which oscillations take place: at the low pressure (resp. high) end stable F2 (resp. F1) would become possible.

B) Topology coexistence

Now we will turn to another topology transition mechanism: topology coexistence (Fig. 4.12). In this case the channel is divided in two parts, each with a distinct structure. We obtain this new mechanism if we increase Q_l and thereby the foam speed (assuming $V_b \sim$ constant). We will proceed in the usual way: for a fixed liquid flow rate we vary the gas pressure and record the resulting flow in the outlet channel. The data we present is obtained in channel A.2.2. A phase diagram showing, for one particular channel geometry, for what combinations of Q_l and P_g the different mechanisms occur, will be presented in section 4.2.4.

For fixed Q_l and P_g, in the pressure domain corresponding to the transition region from F2 to F1, the topology in the channel seperates into two zones: one upstream having an F1 structure and one downstream with an F2 structure (Fig. 4.12). The position of the interface between the two zones depends on P_g. It moves downstream for increasing P_g, to disappear eventually upon joining the stable (P_g,Q_g) curve.

For a given P_g, the interface separating the two topologies stays at a fixed position. The foam moves downstream, so in the reference frame of the foam, the interface moves upstream with a speed that has equal magnitude but opposite

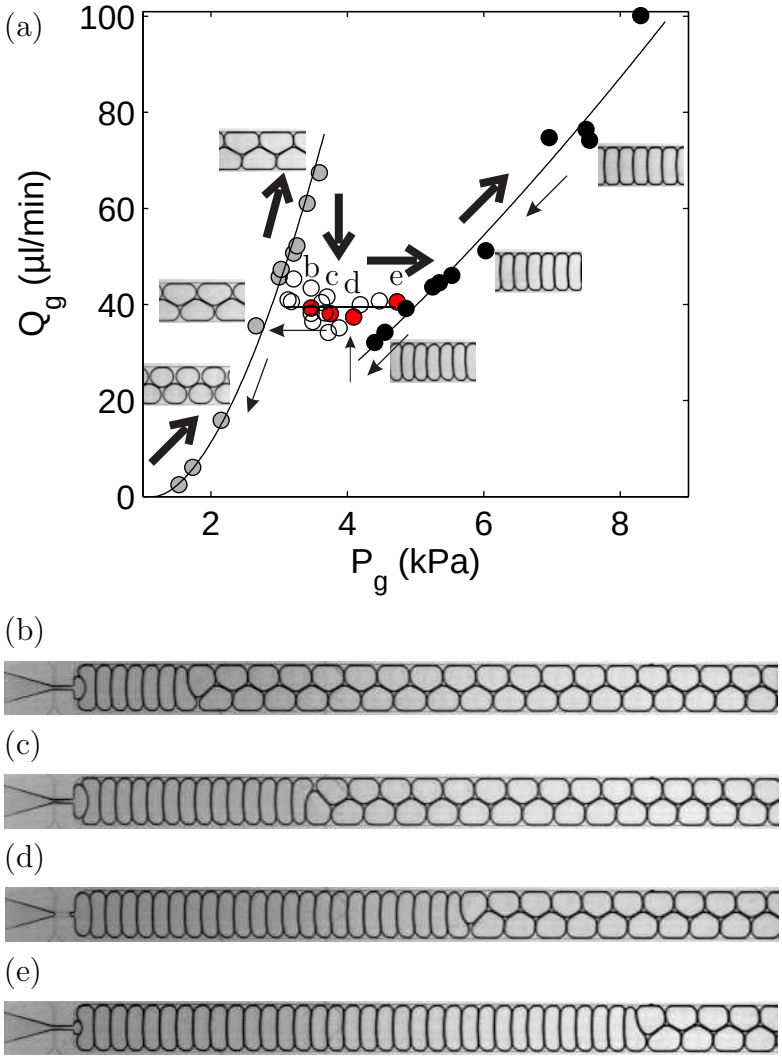

Figure 4.12: Case B: topology coexistence, $Q_l = 5$ μl/min. (a) Foam flow rate and type as a function of the applied pressure: stable F2 (grey symbols), coexistence (open symbols), and stable F1 (black symbols). Continuous lines are guides for the eye. The red points in (a) correspond to the different pictures (b), (c), (d) and (e) showing a coexistence of the two topologies that favors F1 at higher pressures. Arrows indicate the direction of the path upon increasing (thick arrows) and decreasing (thin arrows) pressure.

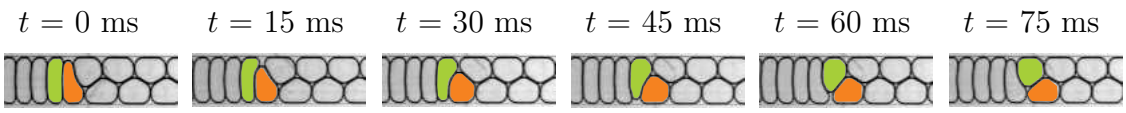

Figure 4.13: Case B: series of T1-events (T1-wave) moves upstream with a speed with same magnitude but opposite sign as the foam speed. Between 0 and 30 ms, a T1 takes place allowing the orange bubble to fit into the F2 topology; Same for the next green bubble between 30 and 60 ms.

sign as the foam's. This interface moves by a succession of T1 events (wall T1's, see Fig. 4.9b) that we call "T1-wave" (Fig. 4.13).

In the transition region the bubble volume, foam flow rate ($Q_g = 39 \pm 4$ μl/min), foam speed v_f and speed of the T1-wave v_{T1} (both $v_f = -v_{T1} = 8.3 \pm 0.5$ mm/s) are constant in time and independent of driving pressure P_g. An increase in P_g only leads to a higher amount of F1 bubbles, thereby balancing the pressure increase by a dissipation increase. This means that the interface position can adjust so that $v_f = -v_{T1}$; and this situation is stable.

We have observed (data and a possible explanation will be shown in the next section) that the speed of the T1 wave depends on bubble size. It increases for smaller bubbles and decreases for larger bubbles. Note that bubble size is related by the foam flow rate by $Q_g = V_b f$. This implies that an increase in the foam flow rate will lead to a decrease in the speed of the T1-wave and vice versa.

Now we can explain why the bubble volume (and hence the gas flow rate) corresponds to a stable equilibrium, if it is insensitive to small fluctuations $\Delta v = v_f + v_{T1}$ in the difference between the foam speed and the speed of the T1-wave. We start by assuming a small increase (decrease) in V_b. This increase (decrease) will lead to an increase (decrease) in v_f and, as we stated above, a decrease (increase) in v_{T1} and therefore to $\Delta v > 0$ ($\Delta v < 0$): the interface will move slightly downstream (upstream), thereby augmenting the dissipation in the channel, creating a disbalance with the pressure, and thereby decreasing (increasing) Q_g and v_f.

Durand and Stone recently investigated T1 relaxation times, the time interval between the intermediate state and the final state in Fig. 4.9a [21]. They found this relaxation time to depend on the surface viscoelastic properties, notably the surface shear plus elongational viscosity $\mu_s + \kappa$ and the Gibbs elasticity ϵ and **not** the shear viscosity of the bulk liquid. This indicates that forces due to film creation (between intermediate and final states) dominate over wall Plateau border friction. Their analysis gives a typical time of the relaxation:

$$\tau_{T1} = \frac{\mu_s + \kappa}{\epsilon} \approx 30 \text{ ms}, \tag{4.16}$$

for an SDS solution (SDS is the dominant surfactant in our soap solution). Here

the next T1 is triggered at the distance Δx (equal to the distance between two bubbles in the F1 configuration) so that

$$v_{T1} = \frac{\Delta x}{\tau_{T1}} \simeq \frac{350\ \mu\text{m}}{30\ \text{ms}} \ = \ 12\ \text{mm/s}. \tag{4.17}$$

We measure $v_f = |v_{T1}| = 8$ mm/s, which is very close to the prediction following Durand *et. al.*. A calculation of the T1-speed only assuming dissipation in the wall Plateau borders (so neglecting surface effects in the newly formed films) leads to unrealistic speeds that are about a factor hundred bigger (data not shown).

An interesting thing to note is the hysteresis at the transition from stable F1 and F2 to topology coexistence (Fig. 4.12). It is related to the bubble volumes V_{12} and V_{21} for which a topology transition at the orifice can take place. As we saw in Fig. 4.5, the bubble volume above which F1 and below which F2 is energetically favorable equals $V_b = 0.58\ hw^2$. The volumes we measured for the last stable F2 and F1 were $V_{bF2} = 0.40\ hw^2$ and $V_{bF1} = 0.27\ hw^2$ respectively. Note that these last measurements correspond to stable flow, and not to the transition values: $V_{bF2} < V_{21}$ and $V_{bF1} > V_{12}$ (and for the F2 structure this value still corresponds to the energetically most favorable topology). In the pressure range for topology coexistence V_b is approximately constant (at the volume for which $v_f = -v_{T1}$). This volume is both smaller than V_{21} and larger than V_{12}. This leads to the hysteresis in Fig. 4.12: we conclude that before the system can enter the topology coexistence regime, there is a barrier to overcome, for F2 V_b and thus Q_g must be above and for F1 below a certain threshold.

C) Topology oscillation and coexistence

In this section we will present a third transition mechanism from stable F2 to F1, that we obtain if we increase again Q_l (compared to (B)) and thereby the foam speed. It presents elements of both the time alternance (oscillation) in A and the space alternance (T1 wave) of B. This mechanism replaces mechanism B when we increase the liquid flow rate Q_l. The data we present is obtained in geometry A.2.2 and for a liquid flow rate $Q_l = 10\ \mu$l/min.

During the whole cycle an F1 foam is formed at the orifice (see Fig. 4.14). Pressures however are too low to allow stable F1. During the minimum of a cycle (smallest V_b) a transition takes place, close to the orifice, from F1 to F2. We see again a T1-wave moving upstream. The magnitude of the velocity however is slower than the one for the foam speed: the interface between T1 and T2 is advected out of the channel.

The instability that leads to the initiation of the transition from F1 to F2 is not very clear up till now. We think it to be related to a growing oscillation of the interfilm distance, until at some point this interfilm distance becomes so small that a first T1 can take place. Fig. 4.14b shows a hint of this oscillation as can be seen by the slightly varying distance between wall vertices in the small

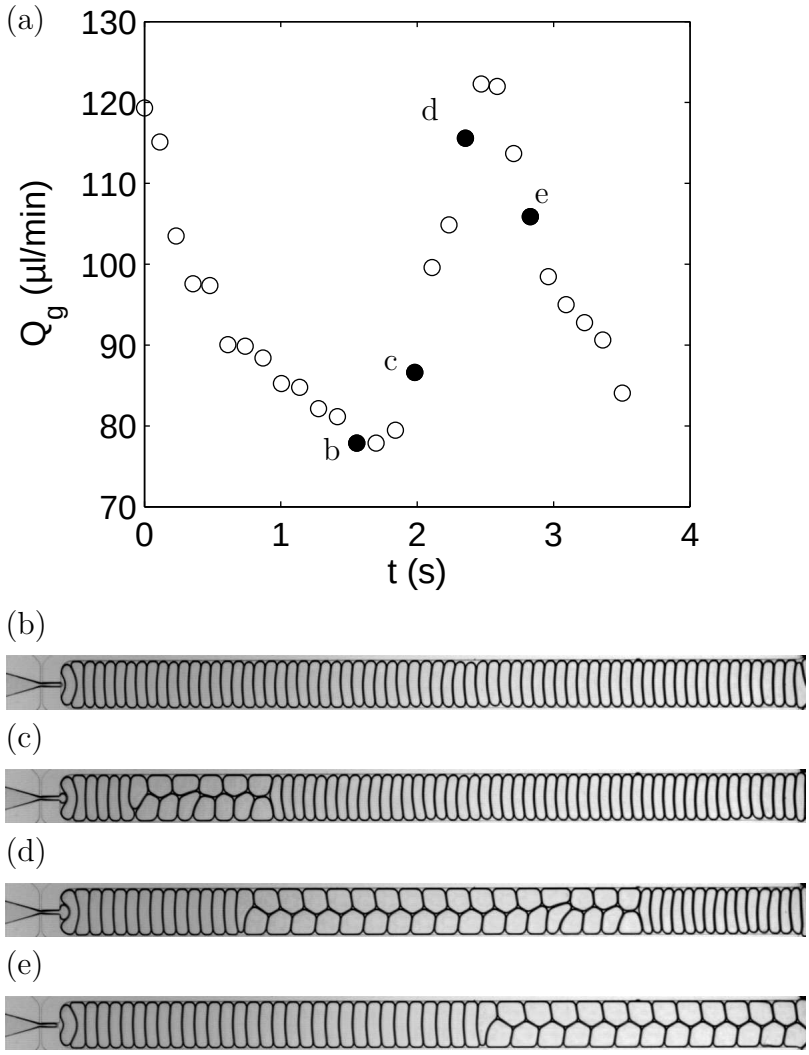

Figure 4.14: Periodically oscillating foam flow with an advected T1-wave. Input parameters are constant: $Q_l = 10$ μl/min and $P_g = 9.26$ kPa. (a) Gas flow rate (in μl/min) oscillates in time (s). (b) Minimum flow rate corresponds to a foam in the F1-structure. (c) Close to the orifice a transition to F2 takes place. The foam accelerates. (c) A T1-wave creates allows a growing part of the channel to have an F2 structure. (d) Its speed however is slower than the foam so the T1 wave is advected out of the channel. The foam slows down.

bubbles at the entrance of the outlet channel. We observed this to be a precursor for the creation of a transition to F2. In section 4.2.4 we will discuss a better example in a wider channel (Fig. 4.22).

Neither the foam speed nor the T1 speed are constant during a cycle (see Fig. 4.15). v_f is highest when the proportion of F2 is maximum, and lowest when the proportion of F1 is maximum. v_{T1} decreases when the bubble size grows, (*i.e.* when the amount of F2 increases) and grows when bubble size diminishes (corresponding to an increase of F1). Both speeds v_f and v_{T1} converge when the interface between F1 and F2 is transported downstream, thereby slowing down the foam and accelerating the T1-wave. The T1-wave is advected out of the channel before an equilibrium can be reached.

In case B (topology coexistence) at $Q_l = 5$ μl/min we measured $v_f = |v_{T1}| = 8$ mm/s. Now both speeds are higher, $v_f > |v_{T1}|$. We find averaged over one cycle: v_f = 19.7 and v_{T1} = -12.9 mm/s. v_f depends on P_g and Q_l (increasing f). So its increase is related to the factor two increase of Q_l. For v_{T1} things are slightly more complicated. It is still close to the speed predicted by Durand's model but higher than for (B) and oscillating. In this case T1s go faster for a smaller bubble size. V_b was 28 nl for the topology coexistence, and now the averaged V_b is 21 nl for the case of an advected T1 wave, *i.e.* a ratio of 0.75. This is not too different from the ratio of the speed of the two T1 waves: 0.62. We explain this in the following way: the smaller the bubbles in the F1-structure (for $V_b < 0.58$ hw^2), the further away they are from their equilibrium state, so the bigger the force that will drive them back upon a T1. So we claim that, while $V_b < 0.58$ hw^2, small bubbles are further from equilibrium, leading to fast T1'=s and large bubbles are closer to the energy minimum, so their T1s are slower.

We also assume that there is a link between the speed of the T1-wave and the foam liquid fraction. Assuming less dissipation for wetter foams, one might think that T1s are faster in that case. This is not what we observe. The injected liquid fraction $\alpha_l = 0.11$ for the situation B. In C α_l oscillates between 0.12 and 0.08, with only a small dependence on P_g: although the foam is drier, the speed of the T1-wave is higher. This seems to indicate the dominance of bubble size effects (restoring force) over the liquid fraction (dissipation).

Note that the T1-wave only moves upstream, although bubbles are in an energetically unfavorable state also downstream (see for example Fig. 4.14c or d). The confinement seems to be the dominant factor. The two F2 bubbles at the front (upstream edge) of the T1-wave create an asymmetry, one is protruding more than the other. This causes the first F1 bubble to be deformed asymmetrically: one of the films touching the sidewalls becomes shorter than the other. When this film becomes shorter than L_c, a T1 occurs, thereby propagating the wave. We have not seen this asymmetry at the tail (downstream edge) of the wave. The two tail F2 bubbles form a symmetric interface with the F1 foam (see again Fig. 4.14c or d), impeding any T1.

We will not present a systematic study of the different flow types if we sys-

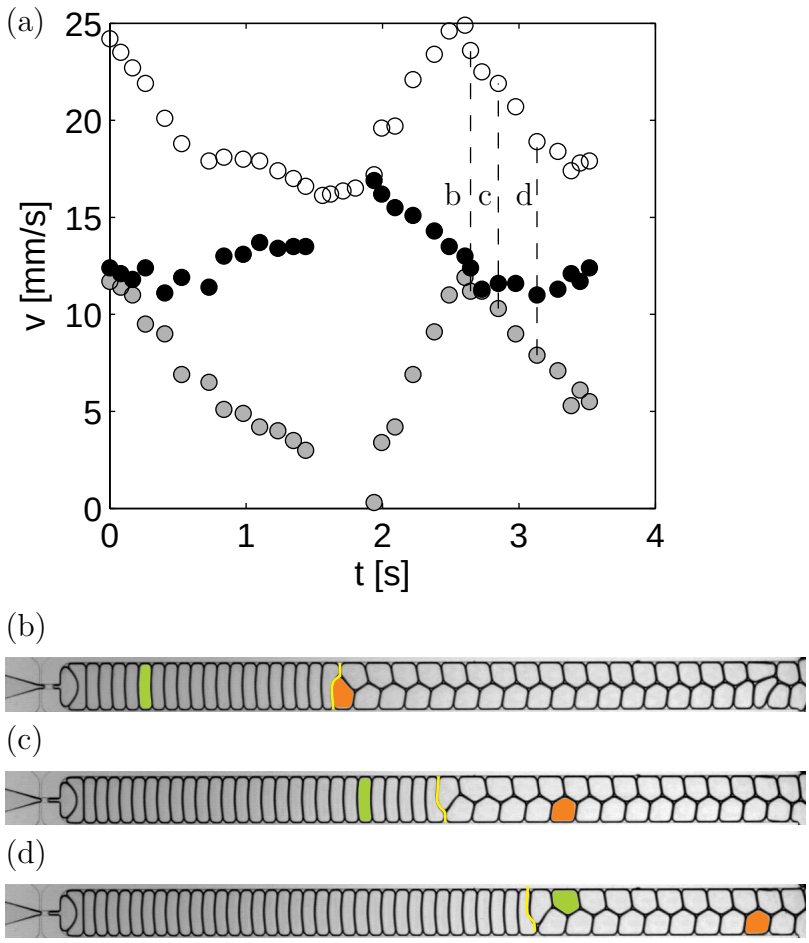

Figure 4.15: Case C: velocity of the foam and the T1-wave. (a) Foam speed v_f (open symbols), relative speed of the T1-wave $-v_{T1}$ (black symbols) $= v_{\mathrm{T1,absolute}}$ (grey symbols)- v_f. (b), (c) and (d) pictures at positions labelled in (a). Two bubbles are labelled to indicate foam speed. The yellow line indicates the T1 wave position. The interval $t \in [1.5, 1.9]$ corresponds to the absence of a T1 wave: the start corresponds to the advection out of the channel of a T1 wave, and the end with the creation of a new one.

tematically vary P_g with constant Q_l (as we did for A and B). We will just say that a pressure increase is accompanied by an increase of the proportion of the F1 structure, as in both previous cases (see Fig. 4.16).

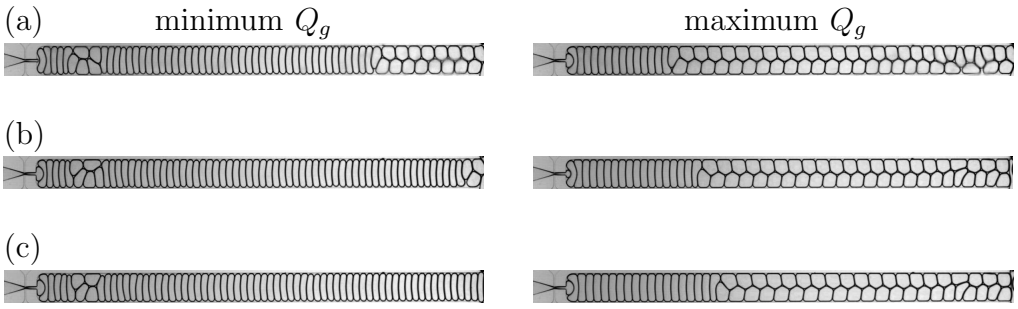

Figure 4.16: Case C: pictures corresponding to minimum (left column) and maximum (right column) foam flow rate Q_g during the pulsation. For increasing P_g ((a) $P_g = 8.22$, (b) $P_g = 8.97$ and (c) $P_g = 9.26$ kPa), the proportion of F1 structure increases.

Selection of the topology transition mechanism

For geometry A.2.2 we explored our system's two control parameters P_g and Q_l and recorded the resulting flow (Fig. 4.17). For increasing liquid flow rate Q_l, the transition region from F2 to F1 gives rise first to topology oscillations, then to topology separation and finally to oscillations characterized by an advected T1-wave.

We propose that the three different F2-F1 transition mechanism are governed by three distinct cases corresponding to $\Delta v = v_f + v_{T1}$ respectively a stationnary, a convected and an absolute F2/F1 transition instability:

- $\Delta v < 0$. Mechanism A. The speed of the T1-wave is larger than the one of the foam. In this case the wave will reach the orifice and lead to F2 generation directly at the orifice. We believe this to be the case for the topology oscillations. We can reinterpret the transition from F1 to F2 in this framework: if bubbles, close to the orifice, become small enough to rearrange into F2, this instability will become absolute by reaching the orifice.

- $\Delta v = 0$ Mechanism B. The speed of the foam and the T1-wave can adjust to have the same magnitude. This will lead to an interface between F1 upstream and F2 downstream. Its position is chosen to balance the pressure gradient: high gradients correspond to a larger part of the more dissipating F1 structure.

- $\Delta v > 0$ Mechanism C. The speed of the foam is larger than the one of the T1-wave. The T1-wave that originates close to the orifice is therefore advected out of the channel. This is followed by the generation of a new wave that in turn will be advected, and so on.

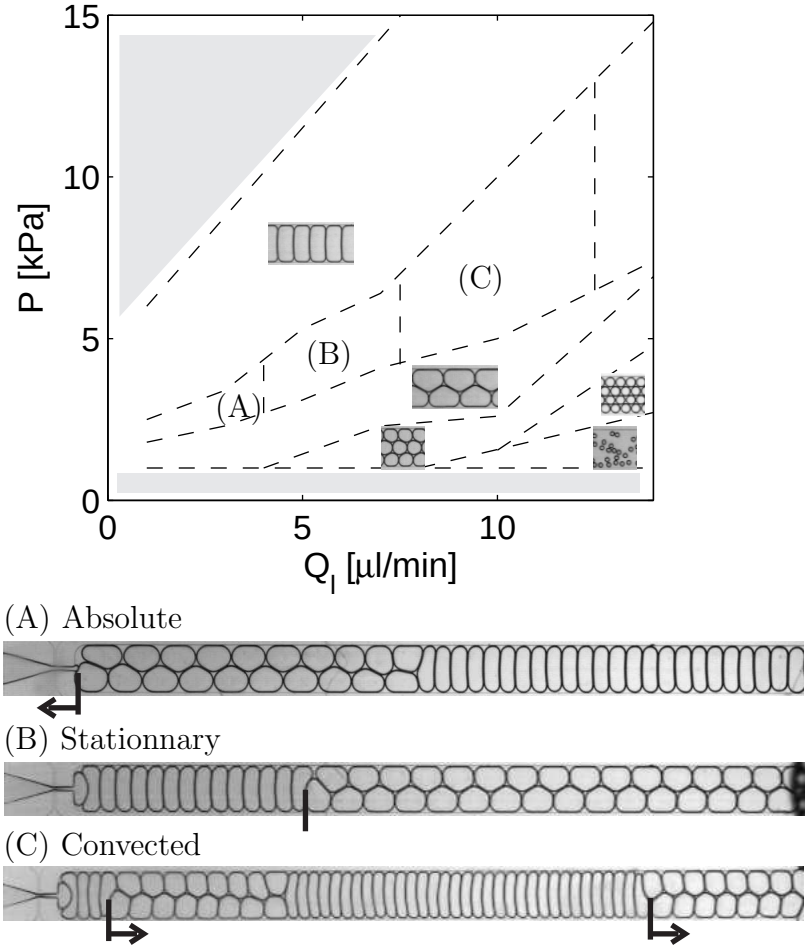

Figure 4.17: Phase diagram for low to moderate Q_l and P_g. For increasing liquid flow rate Q_l, the transition region from F2 to F1 gives rise to (A) topology oscillations, (B) topology separation and (C) oscillations characterized by an advected T1-wave. Lines and arrows indicate the position and direction of the F1/F2 transition. Gray areas are inaccesible and will be briefly discussed in section 4.2.4.

4.2.3 Transition from F2 to F3 and F3 to F4

An instability in the flow also takes place at the transition from F2 to F3 and from F3 to F4. In the following we will show some images of these instabilities and

show why they occur in a smaller parameter space and with a smaller amplitude than the instabilities around the transition from F2 to F1.

Fig. 4.18 shows an example of F2-F3 oscillations obtained in geometry A.3.3. The bubble volume oscillates between $V_b = 0.15\ hw^2$ for the transition from F2 to F3 and $V_b = 0.16\ hw^2$ for the inverse transition. Note that we predicted this instability to occur at $V_b = 0.19\ hw^2$ assuming an infinitely dry foam. The somewhat lower value for the measured transition volumes is due to the place occupied by the liquid.

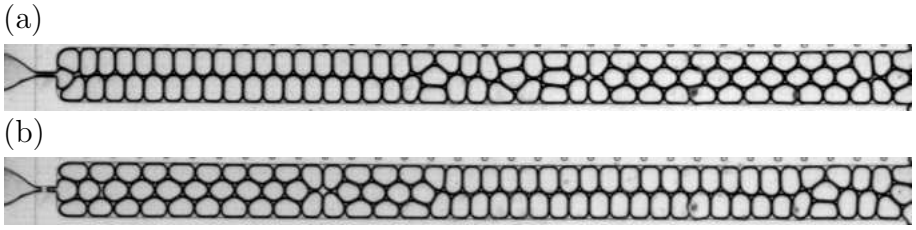

Figure 4.18: Foam state oscillates between the F2 and the F3 structure. (a) F2 formation, (b) F3 formation. $Q_l = 4\ \mu$l/min and $P_g = 1.73$ kPa.

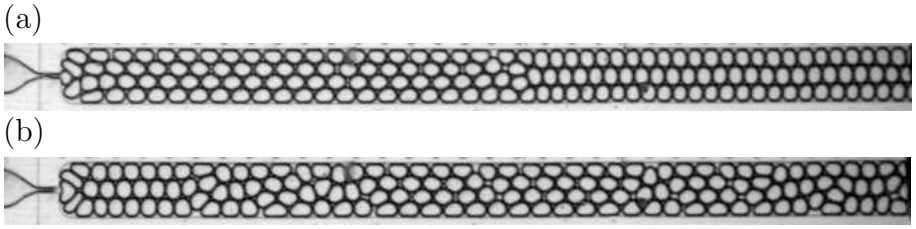

Figure 4.19: Foam state oscillates between the F3 and the F4 structure. (a) F3 formation, (b) F4 formation. $Q_l = 40\ \mu$l/min and $P_g = 5.48$ kPa.

For the F3 to F4 oscillations shown in Fig. 4.19 that are again obtained in geometry A.3.3, the difference between the minimum and maximum of the bubble volume has become smaller that the spread in the volume data: we measure a single value of $V_b = 0.08\ hw^2$. This value is again slightly smaller that the predicted value of $V_b = 0.10\ hw^2$.

The amplitude and the extent of the oscillations in V_b and Q_g decrease for increasing number of bubble rows. We can identify two causes:

- A decrease in the ratio of the projected film length per bubble at the transition volume: $L^p_{F1}/L^p_{F2} = 1.5$, decreasing to 1.25 for the transition F2-F3 and 1.17 for F3 to F4 (Fig. 4.5). Curves for stable P_g-Q_g combinations come closer, thereby decreasing the pressure range over which oscillations take place.

- A decrease in the hysteresis of the bubble volumes for which a transition to an energetically more favorable topology can take place. This leads to smaller amplitude of the flow rate oscillations.

4.2.4 Phase diagram

In the following we will present a phase diagram (Fig. 4.20), for one single geometry, in which we systematically varied the two control parameters P_g and Q_l and recorded the resulting flow in the outlet channel.

Globally, as expected we see, when increasing P_g, that for fixed Q_l, V_b grows, bubbles start touching, a jamming transition takes place and foams form with less and less bubble rows to eventually reach the bamboo structure.

For increasing liquid flow rate Q_l, at the transition from bubbly flow to foam flow, we first see the apparition of the F3 structure, then F4 and F5. This seems to indicate that the transition from bubbly flow to foam takes place at smaller bubble volumes for increasing Q_l. This means a decreasing liquid fraction for a fixed bubble volume at higher Q_l (drier foams), a sthe transition from bubbly flow to foam is only governed by liquid fraction. We did not see this effect in the channel geometry and range of flow rates used in section 3.1.2; we will discuss it at the end of this section.

Now we shall discuss the last few flow regimes depicted in Fig. 4.20 that we have not treated yet. In the polydisperse case (Fig. 4.20g) PD, newly formed bubbles can break their predecessor in multiple parts. Newly formed bubbles start as circular caps around the orifice. Bubbles in the channel are very elongated. In response to pushing bubbles, two films touch and break-up takes place (see Fig. 4.21). This regime appears for moderately small V_b and high Q_l.

This bubble mediated bubble break-up can lead to a new type of instability in the case of channel with a very large ratio of channel width to orifice width w/w_{or} (geometry A.3.4), see Fig. 4.22. This instability shows stable formation of extremely elongated F1-bubbles (a and b), but a bubble flow of constant volume is not possible, as it corresponds to thin bubbles that break-up due to a very small perturbation (c). This break-up is accompanied by an avalanche of T1s, relaxing the foam and decreasing its resistance. Upon evacuation of this zone, the resistance will again increase and a next cycle will start.

A visible wave-like motion is superimposed on the foam flow: a modulation of the interfilm distance is seen where the films touch the sidewalls. It is advected down the channel. We hypothesize that this is the same phenomenon as the one leading to the F1 to F2 transition in section 4.2.2 (B) and (C): when, due to this film interdistance modulation, two wall vertices come closer than a certain critical distance, a T1 will occur. Here the wave-like motion is more visible to the very large channel width.

Regimes (h) F1/F3-F4 and (i) F1/F2-F3 in Fig. 4.20 are a continuation of case (C) showing a transition from F1 to F2 by means of an advected T1-wave.

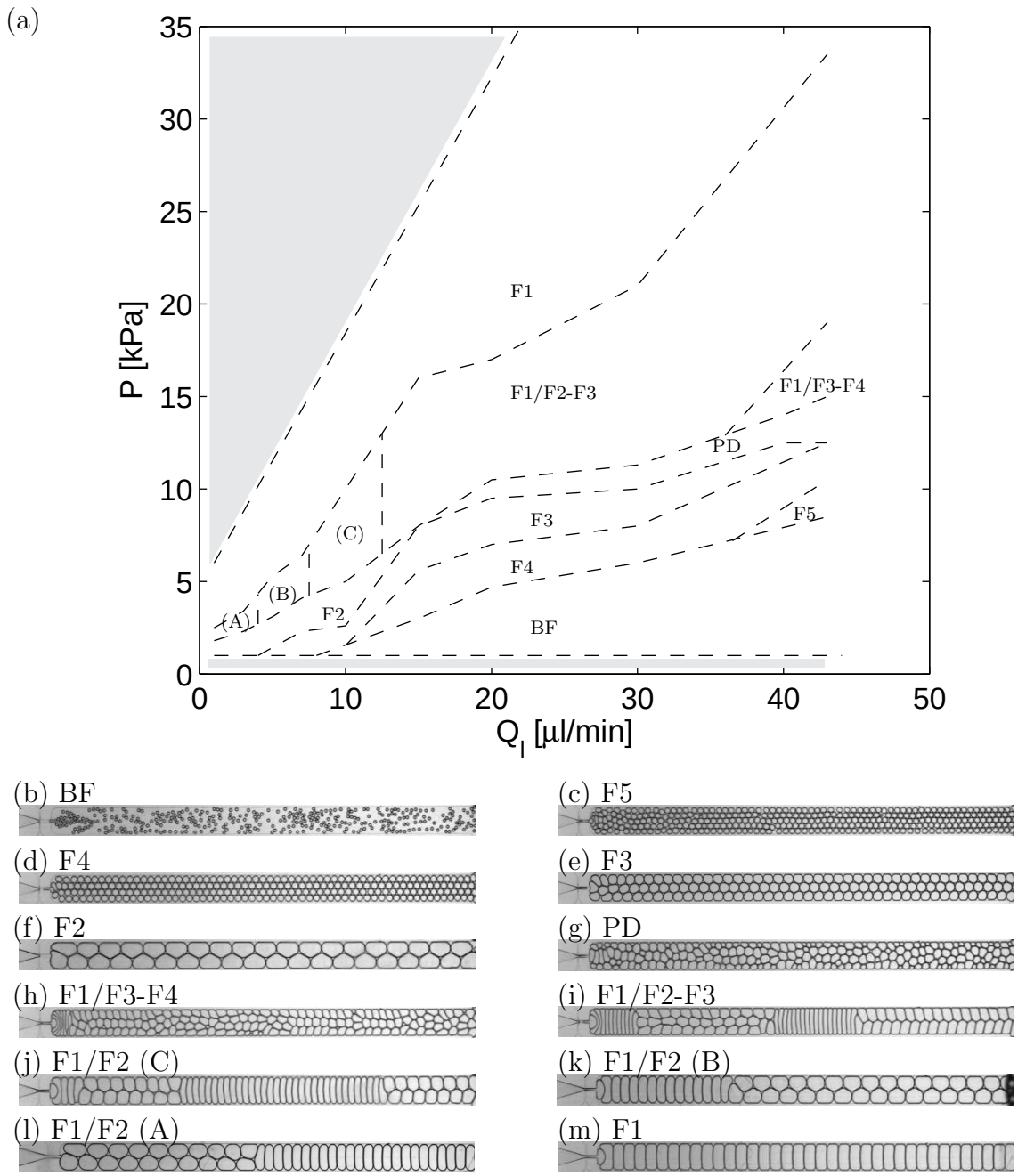

Figure 4.20: (a) Phase diagram for geometry A.2.2. By varying Q_l and P_g we encountered the following flows: (b) bubbly flow, (c) F5, (d) F4, (e) F3, (f) F2 (g) polydisperse, (h) oscillations from F1 to F3 and F4, (i) oscillations from F1 to F2 and F3, (j) oscillation F1-F2 by an advected T1-wave, (k) F1-F2 topology separation, (l) oscillations between F1 and F2 and (m) F1. Boundaries between the different flows are only indicative. Oscillations between F2 and F3 and higher F-numbers are not represented due to the small phase-space that they occupy.

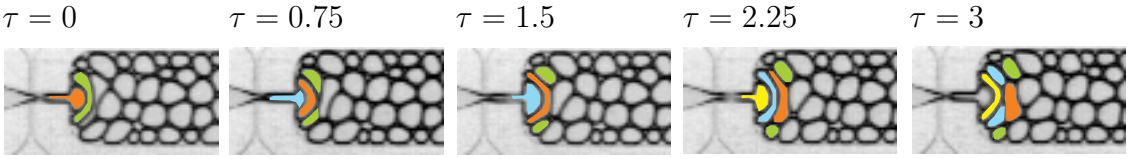

Figure 4.21: PD, case (g) of Fig. 4.20, polydisperse foam generation by bubble break-up. $Q_l = 40$ μl/min and $P_g = 1.06$ kPa. Time normalised by the bubbling frequency: $\tau = tf$.

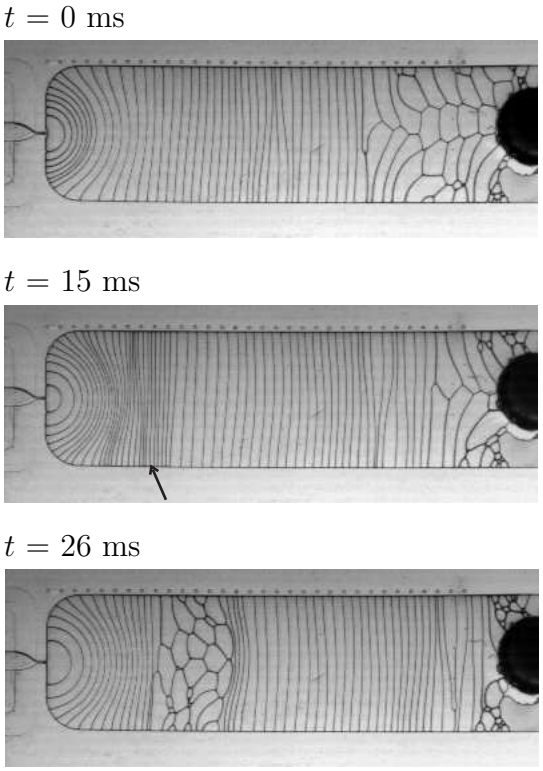

Figure 4.22: Instability due to bubble mediated bubble break-up in a very wide channel (geometry A.3.4). $Q_l = 17$ μl/min, $P_g = 14.1$ kPa. Arrow: onset of T1 formation.

Instead of a relaxation from F1 to F2, the foam transits from F1 first to F3 and then F2 (i) or to F4 and F3 (h). This means that at the transition away from the F1 state, bubble volumes have become so small that F3 and even F4 become the energetically most favorable state. This indicates that a transition away from the F1 state has become even harder compared to regime (j), probably because, upon increasing of the liquid flow rate, the foam has become drier (see also section 4.3.2). Topology transitions takes place by means of T1s. Dry foams can be deformed more than wet foams before a T1 takes place, related to a smaller minimum distance between two vertices before a T1 will take place [51]. Translated to our geometry this would correspond to a transition away from F1 at smaller bubble volumes for dry foams, which seems to be the case for regime (i) F1/F2-F3 and (h) F1/F3-F4.

We will end this section with a discussion of the regions in phase-space for which we do not observe bubble formation (indicated in gray in Fig. 4.20). The inaccesible low pressure region is below the threshold imposed by the capillary pressure of curved gas-liquid interface in the orifice (as shown in section 4.1.1). The high pressure region corresponds to the transition from bubbly to stratified flow. We did not investigate the details of this transition. The shape of the line indicating the transition hints that it takes place for an approximately constant big bubble size ($V_b \sim Q_g/Q_l$ with $Q_g \sim P_g^{3/2}$). We observed the transition to take place for $V_b < V_{channel}$. We hypothesize that above a certain V_b, a small increase in P_g will lead to larger and therefore less bubbles, so less dissipation, therefore a faster flow, that in turns leads to larger V_b. Equilibrium V_b however would correspond to $V_b > V_{channel}$, which is impossible.

4.3 Outlook

4.3.1 Compressible foam flows

In the following we will assume the validity of the ideal gas law, for the dispersed phase in our foam. We can compare the volume and pressure of a bubble with its volume and pressure in a reference state by:

$$PV_b = P_0 V_{b,0}. \tag{4.18}$$

In most cases studied here (and in all macroscopic foams) the relative variations of P are too small, both in statics (Laplace) and dynamics (friction) to induce a volume variation. So the foam flow is nearly incompressible. Since here the scale is small, we can obtain an exception by having a large pressure drop: either at high velocity or with many bubbles.

An example of a compressible microfoam is shown in Fig. 4.23. In this very long channel one can clearly see bubbles smaller at the orifice than at the channel exit. The total pressure drop over the channel is $P_g = 42$ kPa, so, a

bubble that has an initial volume $V_{b,i}$ will experience a decompression of a factor $V_{b,0}/V_{b,i} = P_g/P_0 = 1.4$, between formation at the orifice and the end of the outlet channel at atmospheric pressure $P_0 = 101$ kPa.

However the local area measurement (Fig. 4.23b) shows a decompression of a factor $V_{b,0}/V_{b,i} = 1.7$: bubble size grows more than what we can explain just by decompression. For the same reason the pressure P inferred from eq. (4.18) using this measurement exceeds the actual value ($\sim$200 kPa instead of 142 kPa).

Note that compressible foams are not restrained to very long channels. The only factor that matters is a high enough pressure drop. This can also be realised in short channels by working at high liquid flow rate Q_l. We have shown an example in Fig. 4.24 for high Q_l and P_g. Also in this case decompression is larger than what can be explained just be the pressure decrease: $V_{b,0}/V_{b,i} \approx 1.56 < P_g/P_0 = 1.35$.

The bubble size growth to more than what we can explain by just decompression might be due to the gas transport from high to low pressure bubble through the liquid films. This is an example of coarsening, a phenomenon that we have not seen before. This case is different in two aspects. First, in the very large total pressure drop; but in the case of the very long channel, also in the long residence time of a bubble in the channel, of about $\tau = n_b/f = 45$ s, compared to typical values $\tau < 0.5$ s.

Local pressure measurements are notoriously difficult in microfluidic systems. The most suitable option, both in precision and in ease of implementation, is by a applying a co-flow, for which pressure can be measured by coupling it to the position of the interface between flow and co-flow [1, 35]. In our context of foam flow in channels, dissipation is mainly localized close to the wall. Replacing one of these walls by a co-flow would therefore perturb the flow and influence the measurement. Our present pressure measurement using a compressed foam does not present this disadvantage, it is however to much influenced by coarsening.

4.3.2 Pressure driven drainage

Now we shall turn to a possible explanation of the observation (in section 4.2.4) that foams, for given bubble volume, seem drier for increasing Q_l. In section 3.1.2 we showed that the bubble volume is a function of the injected liquid fraction α_l: $V_b = V_l \beta \alpha_l^{-1}$. The liquid fraction that we should consider in this context is not the injected liquid fraction α_l, but the *actual* liquid volume fraction ϕ_l. α_l is equal to ϕ_l only if $\langle \overline{u_g} \rangle$ and $\langle \overline{u_l} \rangle$ are equal (as detailed in section 2.2.4). This equality was tacitly assumed so far (and verified for the data in section 3.1.2). It implies the absence of pressure driven drainage, a liquid flow through the moving foam.

We will now express the volume liquid fraction ϕ_l in terms of the bubble volume, while allowing for pressure driven drainage (which is an increase of the space and time averaged liquid velocity $\langle \overline{u_l} \rangle$ with respect to the space and time

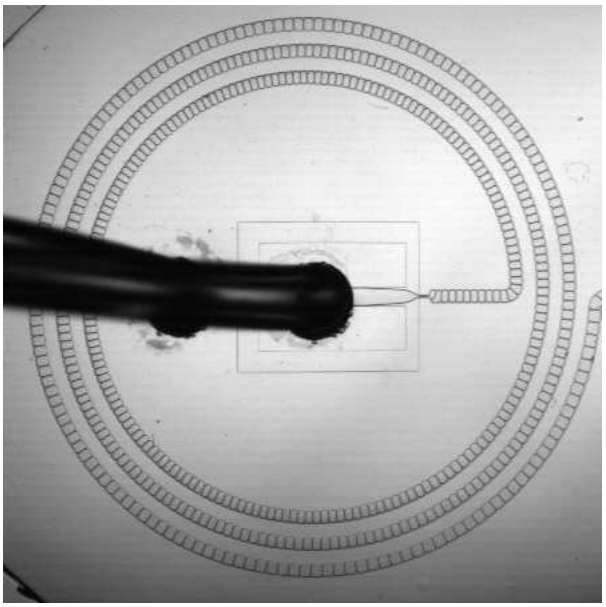

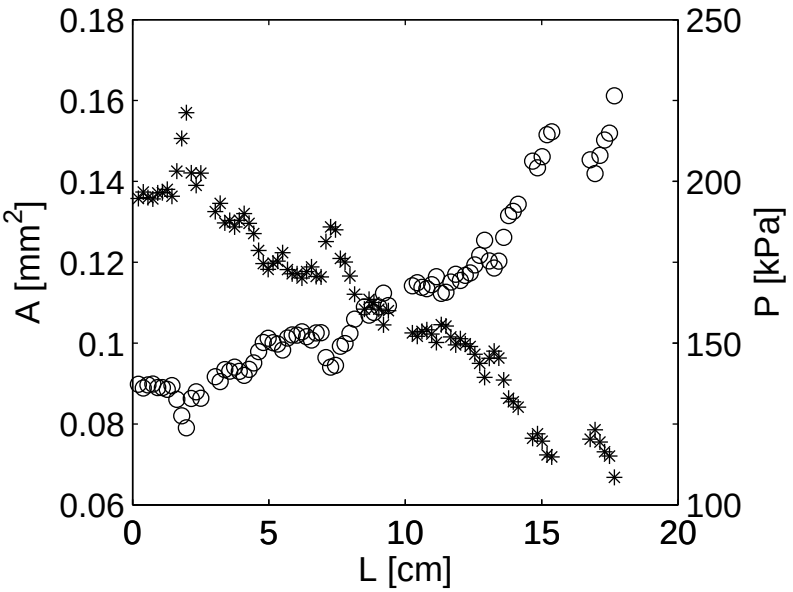

Figure 4.23: Compressible foam flow. (a) Ultralong channel, length $L = 18$ cm, $Q_l = 1$ μl/min and $P_g = 42$ kPa. The channel curvature does not influence the physics: the bubble length ΔL is much smaller than the average channel radius r_{channel}: $\Delta L / r_{\text{channel}} \approx 0.02 << 1$. (b) Local bubble area (circles) and pressure (asterisks) measurement. The temporary drops in bubble area and pressure at 2, 7 and 16 cm are an artifact due to inhomogeneous lighting of the channel.

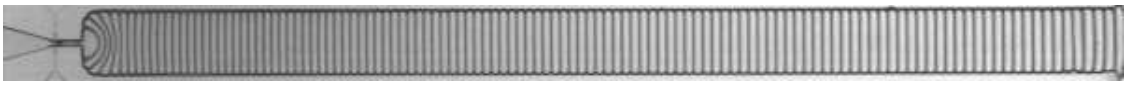

Figure 4.24: Compressible foam flow at high flow rate, $Q_l = 43$ μl/min and $P_g = 35$ kPa, $L = 16$ mm.

averaged gas velocity $\langle\overline{u_g}\rangle$), by using equation 2.13 and 3.2:

$$\phi_l = \frac{1}{1 + \frac{\langle\overline{u_l}\rangle}{\langle\overline{u_g}\rangle}(\overline{V}_b - 1)}, \tag{4.19}$$

with $\overline{V}_b = V_b/(V_l\beta)$. This equation can be simplified, using the approximation that $\alpha_l \simeq Q_l/Q_g$ for the foam state, to:

$$\phi_l = \frac{1}{1 + \frac{\langle\overline{u_l}\rangle}{\langle\overline{u_g}\rangle}\overline{V}_b}. \tag{4.20}$$

Now a foam will become drier, not only for increasing bubble volume, but also for increasing $\langle\overline{u_l}\rangle/\langle\overline{u_g}\rangle$.

We associate the higher P_g (and the related liquid pressure) for a given V_b at higher Q_l with an increase of $\langle\overline{u_l}\rangle/\langle\overline{u_g}\rangle$. This would explain the decrease of ϕ_l for constant V_b at higher Q_l. Unfortunately it is very hard to properly measure separately the liquid and gas velocity in the channel. The use or development of experimental techniques allowing this, would evidently be of great interest (for a first attempt see [39]).

An alternative way to explain that foams are drier for given bubble volume at higher liquid flow rates, would be by using our analysis on gas thread retraction after bubble break-up leading to wetter foams at low liquid flow rates. We suppose however that this effect will only play a role at very low flow rates $Q_l < 6$ μl/min (section 3.2.2). We see effects at much higher Q_l which discards an explanation depending on bubble generation.

Note that equation 4.19 concerns only the channel transit and becomes irrelevant in the context of the so-called 'tailor-made' foams. Here ideally one wants to produce a foam with a flow-focussing device with a bubble volume and liquid fraction to be set at will and independantly. At the channel outlet the liquid will be reinhected into the outgoing foam so that at the exit ϕ_l will equal α_l (on average, and locally if one assumes that the liquid is reinjected homogeneously). In this static foam, all modifications of the liquid fraction due to speed differences will disappear. To our knowledge the only way to vary V_b and α_l independently is by varying the channel geometry.

On the other hand, Garstecki *et. al.* claims in [28] that V_b and ϕ_l can be varied independently: in *their bubbly flows* (not on foam flows), the bubble volume depends solely on the ratio of gas pressure to liquid flow rate, $V_b \propto P_g/Q_l$. They define the gas fraction at the outlet channel entrance as: $\phi_{or} = fV_b/(fV_b + Q_l)$ with $f \propto Q_l P_g$. This corresponds to $\phi_{or} = 1 - \alpha_l$ in our case. Now, by keeping the ratio of gas pressure to liquid volume constant (to keep V_b constant), one can change Q_l, thereby modifying ϕ_{or} at constant V_b. Lowering Q_l should thus correspond to drier foams [28]. They show two images of a 2 row foam: a wet case and a dry case, with the liquid flow rate smaller for the dry foam.

This does not correspond to our findings with foams, where for a given geometry V_b depends on α_l. We have defined two exceptions: the case of pressure driven drainage; and the case of gas-liquid interface retraction after bubble release, at low liquid flow rate. Note that both effects give wetter (and not drier) foams at low liquid flow rates. Furthermore, if we express the bubble volume in terms of the injected liquid fraction, using the relations proposed in [28], we find:

$$\alpha_l = \frac{1}{1 + \epsilon V_b^2 Q_l}, \tag{4.21}$$

with ϵ a proportionality factor with units s/m^9. Here indeed we find a dependence on α_l; but it is in the direction opposite to Garstecki *et. al.*. It leads to the same conclusion as our explanation by pressure driven drainage, namely that foams are drier at higher liquid flow rates.

4.3.3 Distortion effects

For plug flows, friction on the foam-wall interface is dominant when compared to friction internal to the foam [9]. Foam-wall friction is a surface effect. The small typical lengths of our system even increase (compared with macroscopic foams) the relative importance of surface effects. Therefore we expect our system to be well suited for the study of foam-wall friction. Indeed, we have seen situations that critically depend on this effect, *e.g.* the instabilities upon topology-transitions that are caused by a discontinuity in the friction force. We will show a few examples of bubble deformations due to these effects.

We will first discuss deformations in the direction of the flow like in Fig. 4.25b and in the F2 part of (c). Here Plateau's equilibrium law, stating that three liquid films should meet at equal angle of 120°, or 90° where they meet a wall, is clearly violated. For deformed films, the line tensions γ in the three films do not cancel out, but form a resultant force opposite to the flow direction (see Fig. 4.26). This resultant force compensates dissipative forces located in the wall Plateau border area, where the film between two bubbles touches the wall. These deformations are associated with high foam flow velocities [8, 19]. Indeed Fig. 4.25b shows a situation corresponding to both high gas and liquid flow rate (upper right corner of the phase diagram in Fig. 4.20). The results we have

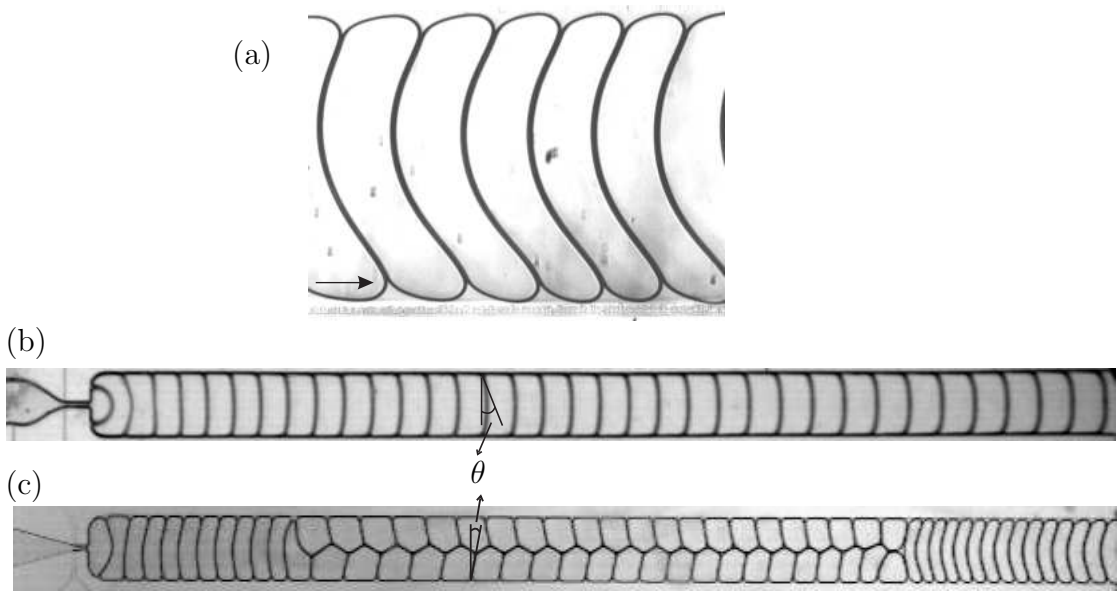

Figure 4.25: Distorted foams. We observed different directions of the deformation: (a) boomerang-like shapes (arrow indicates flow direction), (b) deformation in the direction of the flow. Both deformation directions can occur in the same channel for the same control parameters like in (c) showing an F2/F1 transition by means of an advected T1-wave, with a different deformation direction for the F1 and the F2 part. (a) Geometry A.5 ultraflat channel with a height $h \approx 8$ μm. (b) Geometry A.2.2 μm, $Q_l = 40$ μl/min and $P_g = 21$ kPa. (c) Geometry A.2.1 with $h = 50$, $Q_l = 2$ μl/min and $P_g = 13$ kPa.

shown in the preceding sections all show undeformed films: this implies that for our typical velocity range, the line tension is much bigger than the viscous force.

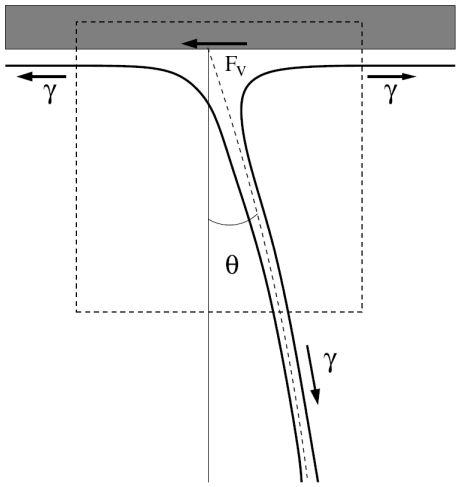

Figure 4.26: Sideview of a wall Plateau border in contact with the channel wall. To compensate the dissipative viscous force F_v, the film deforms by an angle θ. A component of the line tension γ equal to $\gamma \sin(\theta)$ will now oppose the viscous force. Fig. from Cantat *et. al.* [8].

Another distorted bubble shape we observed is the somewhat counter-intuitive boomerang-like form in Fig. 4.25a, with films near the wall pointing backwards. We have encountered this effect for small channel aspect ratios (in Fig. 4.25a it is as small as 0.02), in combination with high liquid flow rates. It could be related to the phenomenon of pressure-driven drainage (which we assume more dominant at small channel aspect ratios due to less expandable corner sections in which the liquid flows). The liquid could lead to a smaller friction on the edges (corners), where water accumulates than at the center. Edges are likely more entrained by a faster liquid flow ($\langle\overline{u_l}\rangle > \langle\overline{u_g}\rangle$) than the centers. Now, in the case of pressure driven drainage, within the reference frame moving at the liquid velocity, the bubbles move in the opposite direction, from right to left. The distortion of bubble shapes in this reference frame then becomes similar to the observations explained in the last paragraph.

An interesting case is formed by the flow in Fig. 4.25c, that displays both types of distortion. The F2 films are curved towards the direction of the flow, and the F1 films are curved backwards. This might be caused by a larger restraining of the flow to channel corners in the F1 case. In the F2 topology, in addition to the channel corners, the liquid can flow in the two Plateau borders (one for the bottom and one for the top wall) in between the two bubble rows, thereby leading to a less pronounced velocity difference between the gas and liquid flow.

4.4 Résumé

Ce chapitre traite l'écoulement de la mousse dans le canal de sortie après sa formation. Nous montrons que son écoulement est non-linéaire, ce qui donne lieu à un comportement très riche.

Dans le paragraphe 4.1, nous présentons des données expérimentales pour le débit de la mousse en fonction de la pression du gaz pour débit de liquide fixe. Ces données montrent une écoulement non-linéaire. Nous trouvons un seuil dans la pression du gaz P_c en dessous de laquelle il n'y a pas de formation de bulles. Ce seuil est d'origine capillaire et lié a la pression nécessaire pour déformer l'interface gaz-liquide afin qu'elle puisse entrer dans l'orifice. Pour des pressions plus grande que P_c la mousse se met à écouler avec un comportement type loi de puissance avec un exposant plus petit que un. Nous comparons les données expérimentales avec le modèle d'écoulement bouchon de Cantat *et. al.* [9].

Si on augmente la pression, la taille des bulles augmente aussi, ce qui mène à des changements de topologie. Ces changements induisent un autre effet non-linéaire : des discontinuités dans la relation pression-débit. Par exemple la transition d'une mousse F2 à F1 induit une chute notable du débit. Ces discontinuités nous mènent à l'introduction du concept de longueur de frottement L_p, qui est une mesure pour la friction en fonction de la taille des bulles et de la topologie.

Le paragraphe 4.2 s'occupe plus en détail des effets discrets liés à un changement de topologie. Nous dérivons des équations analytiques pour l'énergie et le longueur de frottement en fonction de la taille des bulles pour différentes topologies. Ces équations montrent que pour une taille de bulle croissante, la topologie qui représente le minimum d'énergie a un nombre de rang de bulles de plus en plus petit. Pour chaque taille de bulle où deux topologies partagent la même énergie, une discontinuité dans la longueur de frottement se présente. Cela explique la discontinuité dans la relation pression-débit que on a présenté dans le paragraphe 4.1.

En plus, nous montrons que la zone de transition entre F2 et F1 a un comportement particulièrement riche. Pour des pressions de gaz intermédiaires entre une formation de F2 et de F1 stable nous avons mis en évidence trois mécanismes de transition de topologie différents. Le premier présente une oscillation périodique de la topologie accompagnée par une oscillation de la taille des bulles et du débit de la mousse. Si on augmente la vitesse de la mousse nous trouvons un deuxième mécanisme qui montre une coexistence des deux topologies en même temps. A vitesse de la mousse encore plus haute ce mécanisme et remplacé par un troisième qui est caractérisé par une oscillation et coexistence de topologie. Un élément clé de ces mécanismes de transition consiste de ce que nous appelons 'l'onde de T1' : Une avalanche de T1 qui indique la limite entre la zone occupée par la structure F2 et par la structure F1. Le rapport entre la vitesse de l'onde de T1 et celle de la mousse permet de classifier les différents mécanismes.

Nous finissons ce chapitre avec un paragraphe de perspectives (4.3). Nous

montrons quelques exemples de mousses compressibles, nous discutons le phénomène de drainage relative du liquide par rapport au gaz, et nous montrons des images de mousses déformées.

Chapter 5

Microfoam manipulation

Until now we have discussed the generation of a microfoam, how its properties depend on both the control parameters and the system geometry, and its subsequent flow characterized by a topology dependent resistance. For applications in a lab-on-a-chip context, one would also like to exert forces on the microfoam flow to achieve tasks like bubble breaking, sorting, and guiding in a channel system. In this chapter, we will present our work on a passive method depending on the interaction between flow and channel geometry, and an active external method using acoustics.

5.1 Passive manipulation in an Y-channel: splitting, sorting

In this section we will investigate the flow of a microfoam in a channel presenting two Y junctions. At the first Y junction the outlet channel splits in two separated channels with a width $w_y = w/2$, at the second these two channels recombine (Fig. 5.1). It is an example of passive manipulation without any externally actuated elements. Like all passive methods, it has the advantage of being robust and easy to use.

The flow in the outlet channel before the first Y junction behaves qualitatively similar to what we have seen before: for increasing gas pressure P_g or decreasing liquid flow rate Q_l, bubble size grows, and foams with less and less bubble rows are formed. At the first Y junction, depending on the topology, bubbles either sort or split.

For F2 and higher topologies, bubbles stay intact but the foam is split into the two channels. Upon recombination at the second Y junction, the initial configuration is usually restored. Fig. 5.1c shows an exception where an initial F3 foam is recombined to give F2, although that is not the lowest energy state. This is another example of the importance of the preparation method of a foam with respect to the topology it will assume. Recombination of two channels seems

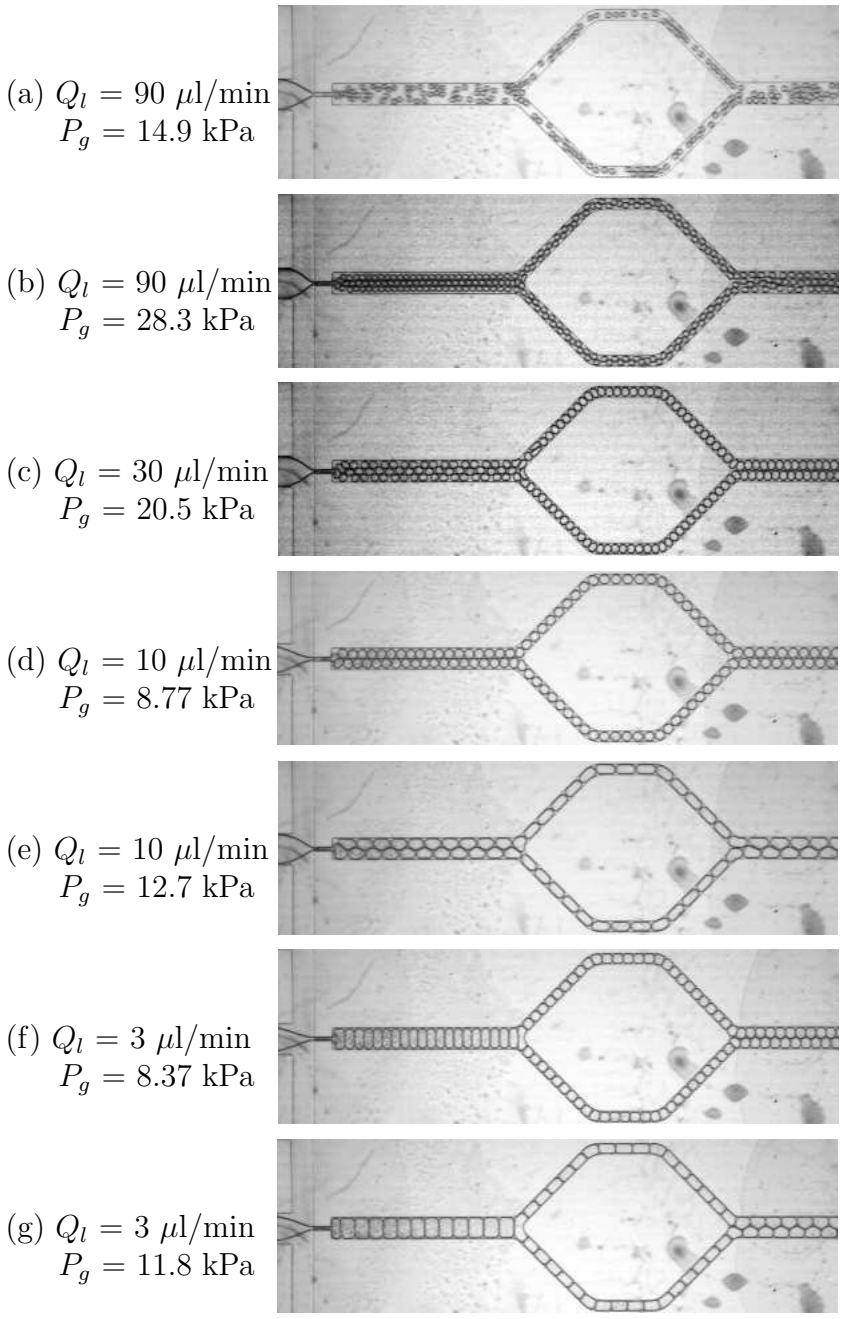

Figure 5.1: Sorting or splitting in an Y junction. Growing bubble size gives rises to different topologies in the outlet channel: (a) bubbly flow, (b) and (c) F3, (d) and (e) F2 and (f) and (g) F1 topology.

to favor F2 formation.

For an F1 foam arriving at the first Y junction, bubbles break into two equal parts. The break-up criterium seems to be that a bubble must span the complete channel width, which is another way of saying that only F1 foams break. For instance the F2 foam in Fig. 5.1e and the F1 in Fig. 5.1f have a nearly equal bubble volume. While the F2 foam is separated into two distinct rows, the bubbles in the F1 foam are splitted.

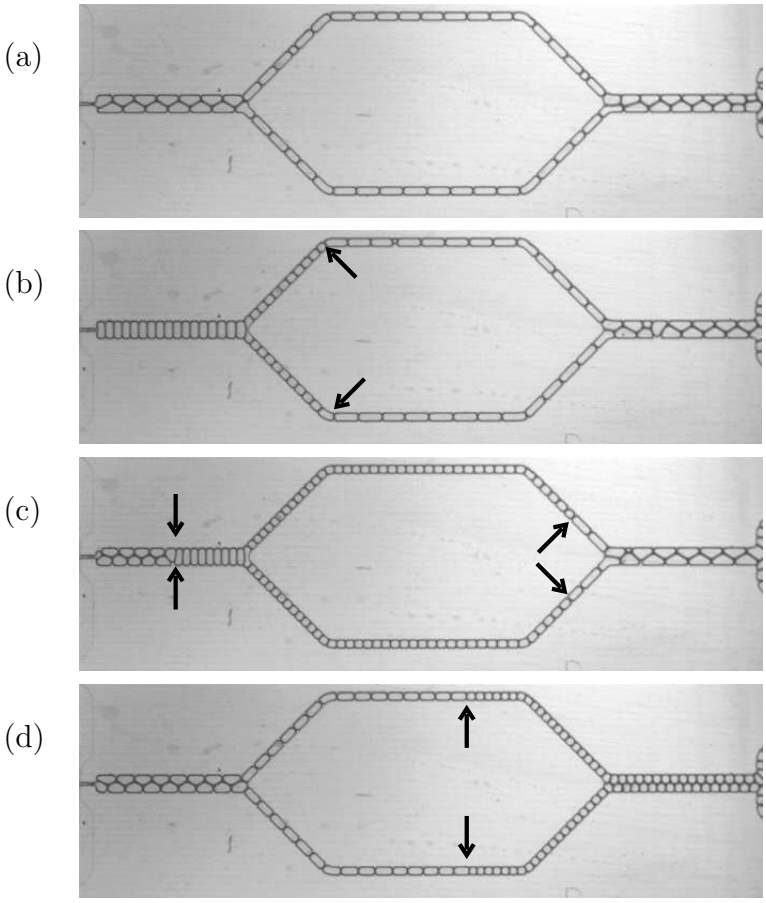

Figure 5.2: Periodic topology oscillation in geometry A.7.2 (but without the sound inlet channel). (a) A cycle starts with an F2 foam in the first part of the outlet channel. (b) Bubbling frequency f and bubble size V_b grow, leading to a transition to F1. (c) Due to the increased resistance to flow, f and V_b drop leading to the inverse transition F2 to F1. (d) Last splitted bubbles are evacuated from the channel. Arrows indicate transition between bubbles initially packed in an F1 and F2 structure. Control parameters: $Q_l = 4$ μl/min and $P_g = 5.90$ kPa.

The bubble splitting case is the foam version of the mechanism first shown by Link et. al. in [42] for drops at high capillary numbers. In our channels Ca is typically very low ($\sim 10^{-4} - 10^{-3}$). Drop break-up at similar Ca has been

investigated by Ménétrier and Tabeling [45]. We do not know, to what extent their analysis can be applied to our high gas fraction case (that is above the rigidity loss transition [6]), in which bubbles are less free to deform than their drops.

Topology instability and bubble splitting

For flows in the transition region between the F1 and F2 topology we encounter the same type of instability as treated in section 4.2. Fig. 5.2 shows an example, combining a periodical topology oscillation (mechanism A in section 4.2.2) with bubble splitting at the first Y junction whenever an F1 foam is formed at the orifice. It is interesting to note that the actual topology transition only takes place at the part of the outlet channel which is before the first Y junction. In the arms between junctions, we only observe F1 foams. After junction, foams always form an F2 foam. Although the discontinuity in the resistance to flow only occurs in less than a quarter of the total channel length, it is not dampened out by the influence of the remaining channel length. It shows that retro-actions between foam generation and flow not only take place in simple systems, with only a straight channel section. Also in more complicated systems care has to be taken if one wants to ensure a stable flow.

5.2 Active manipulation: ultrasound

In this section we will describe a preliminary, qualitative experiment in which we apply acoustic forcing to a bubbly flow. We will mostly show qualitative results. This work is an example of an active method, using an externally actuated element. Compared with passive methods, it shows a large flexibility.

By using the setup as described in section 2.2.5 we will investigate the interaction between low frequency ultrasound (typically about $f \simeq 145$ kHz) and a bubbly flow, both in a straigh channel section (geometry A.7.1) and in an Y junction geometry (geometry A.7.2). We can vary both the ultrasound frequency and the voltage amplitude applied to the piezo-element.

We will first describe the transmission mechanism for the ultrasound. We claim that it is related to standing waves in the glass plate to which the channel system is glued. Then we will briefly discuss the interaction between a bubble and a standing pressure wave. After that we will describe our experimental observations, and finally we will try to estimate the order of magnitude of the forces that can be exerted.

Standing waves in the glass plate

When we designed this system, our initial idea was that the sound would pass through the liquid-filled sound inlet channel (see Fig. 2.12 in chapter 2). This

might have been a bit naive: the wavelength of sound in water at frequencies around 1 kHz is in the order of 1 cm. The water inlet channel is only 100 μm high and 250 μm wide, making it very improbable that the ultrasound can propagate into it (as in a waveguide). This was indeed confirmed by an experiment (data not shown) in which a similar behavior as in the following was observed in the absence of a channel directly connecting the piezo to the flow channel. In this case the piezo element was simply glued to the glass and the PDMS.

A bubble will oscillate in response to a pressure wave. The resonance frequency f_0 for a spherical air bubble in bulk liquid depends on its radius R and is given by the Minnaert equation [46]:

$$f_0 R_0 \approx 3m/s. \tag{5.1}$$

For our bubbles that are non-spherical due to the squeezing between the channel walls, we replace eq. 5.1 by:

$$f_0 \left(\frac{3V_{b,0}}{4\pi} \right)^{1/3} \approx 3m/s. \tag{5.2}$$

For typical bubble volumes ($V_b \approx 40$ nl) that we will encounter in the following, the resonance frequency would be $f_0 \simeq 14$ kHz.

We will see that the experimental observation is very sensitive to f, but not to the bubble volume. Furthermore, we see an effect for frequencies $f = 125$ kHz for the system with a straight outlet channel and around $f = 145$ kHz for the Y junctions: typically an order of magnitude larger than the bubble resonance frequencies, around which we see now effect. It seems we excite at a resonance frequency of another part of the system. A good candidate is the glass cover slide, to which both the channel system cast in PDMS and the piezo element are glued.

In collaboration with undergraduate student David Rabaud, we decided to investigate the behaviour of the glass plate connected to a vibrating piezo element. We simply glued the piezo element to the same cover slides as used in our microfluidic devices and visualize its response to ultrasound by deposing a fine layer of sand on it (see Fig. 5.3).

Standing waves do develop in the glass plate, as can be seen on the images in Fig. 5.3, where the sand grains accumulate in the pressure nodes. For frequencies varying between $f \approx 25$ kHz and $f \approx 100$ kHz we saw so-called Chladni figures, which are vibration patterns in a thin membrane or plate named in honour of the 18th century scientist Ernest Chladni. For frequencies corresponding to the ones we will use in the following ($f \sim$ 125-145 kHz), vibrations became so violent that all the sand was shaken out of the plates, even at low sound amplitudes. This seems to confirm that the dominant mechanism of sound transfer from the piezo to the flow is by a standing wave in the glass plate.

(a) (b)

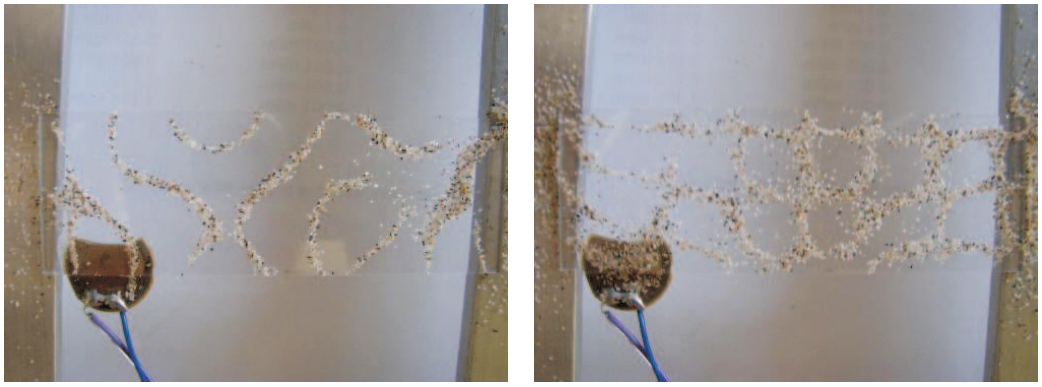

Figure 5.3: Sand patterns on a glass plate. (a) $f = 27.5$ kHz and (b) $f = 46.6$ kHz. The excitation amplitude of the transducer is ∼10 V.

Primary Bjerknes forces

The interaction of an oscillating bubble and a standing pressure field leads to the so-called primary Bjerknes force F_{B1} [40]. We will first briefly discuss this force and then show how it is manifested in our experiments.

At a given moment in time, in a standing pressure field with gradient $\vec{\nabla}P$, a bubble experiences a force

$$\vec{F_{B1}} = -V_b\vec{\nabla}P. \tag{5.3}$$

Both the bubble volume and the pressure gradient oscillate, so averaged over time, a bubble experiences a net force

$$< \vec{F_{B1}} >= - < V_b\vec{\nabla}P > . \tag{5.4}$$

$< V_b\vec{\nabla}P >$ averages out in the direction that $\vec{\nabla}P$ takes when the bubble volume is largest. A bubble of less than its Minnaert resonant size oscillates in-phase with the sound field and bubbles larger than their Minnaert resonance size oscillate π out-of-phase with the field. Therefore the quantity $- < V_b\vec{\nabla}P >$ will be in one direction for bubbles with $r < r_0$ and in the opposite direction for $r > r_0$. Therefore in a standing-wave field, bubbles of less than resonant size travel up the pressure gradient towards the pressure antinodes, and those larger than resonance travel down the gradient to the node [40] (which corresponds to our case of bubbles larger than resonance).

Ultrasound guided bubble motion: ultrasound switch

In our case the standing pressure field seems to be due to vibrational modes of the glass plate. The standing wave pattern creates zones of attraction and repulsion

in the glass plate that, combined with the pressure gradient in the channels, can be used to guide bubble motion.

We use a Y junction geometry with control parameters and geometry chosen to produce a very diluted bubbly flow with bubble diameter of the same order as the channel width ($w = 500$ μm). The unperturbed flow (Fig. 5.4a) leads to bubbles that break up in two equal parts in the first Y junction. In the presence of ultrasound at certain particular frequencies the behavior at the Y junction changes dramatically. Break-up can be avoided; depending on the sound frequency bubbles will either go in the upper Fig. 5.4b or lower branch Fig. 5.4c. We interprete this guiding of bubbles in one of the branches as the result of an attraction by a pressure node (for our bubbles with $R > R_0$) situated close to the upper branch in Fig. 5.4b, and close to the lower branch in Fig. 5.4c.

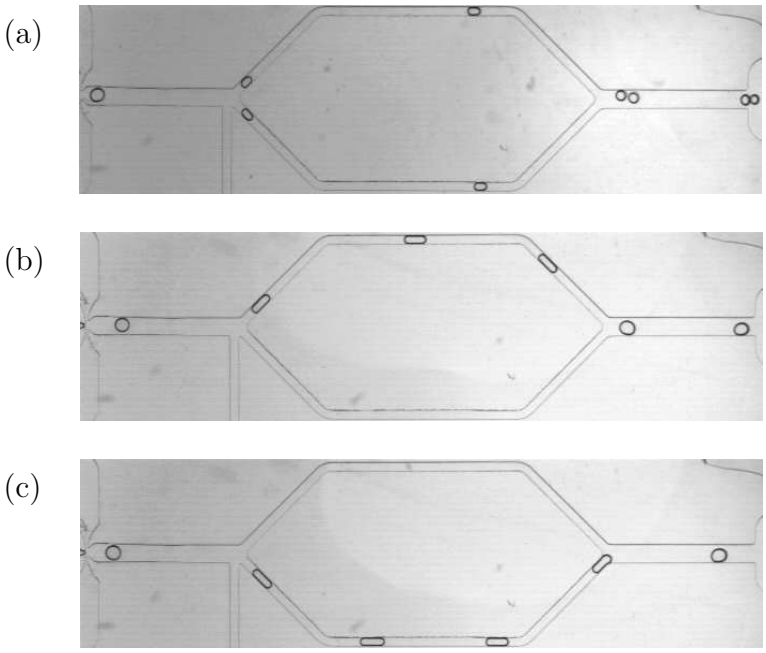

Figure 5.4: Ultrasound controlled bubble motion. (a) No ultrasound: bubbles break up in two equal parts. (b) Ultrasound frequency $f = 147\pm1$ Hz, amplitude $V = 37$ V: bubbles are guided into the upper channel branch. (c) For the same amplitude but with $f = 143\pm1$ Hz, bubbles all go into the lower branch. Ultrasound amplitude is equal for both cases: $V = 37$ V. Flow parameters: $Q_l = 250$ μl/min and $P_g = 3.90$ kPa.

Controlled asymmetric bubble break-up

We repeat the experiment described above for $f = 143$ kHz (Fig. 5.4c), now with a varying ultrasound amplitude V. When we increase V from 0 to 30 V, bubble

break up becomes increasingly asymmetric, with the larger of the two bubbles formed going into the downward channel (see Fig. 5.5). For $f = 147$ kHz, the result is similar, but the larger bubble goes into the upper branch.

To summarize, depending on sound frequency, bubbles are attracted to one of the two branches of the Y. Varying the sound amplitude allows to control the size of the two daughter bubbles after break-up at the Y junction, and for amplitudes around $V = 20$ V, bubble break up is entirely stopped.

Magnitude of the acoustic force

Now we will investigate the influence of the flow by varying the gas pressure, for fixed ultrasound settings (with high enough amplitude $V > 20$ V) and liquid flow rate (Fig. 5.6).

The flow in the outlet channel before the first Y junction, displays the behavior we expect: for increasing P_g, bubble size grows, and the liquid fraction drops. Only a small perturbation due to the sound can be seen in Fig. 5.6b and c: the bubbling frequency becomes slightly irregular, leading to a variable bubble spacing. For low gas pressures all the bubbles are deviated into the lower channel branch ((a) to (d)). For higher P_g a certain proportion of the bubbles does break at the Y junction, with the bigger part going into the lower branch (e). Increasing P_g further leads to an asymmetric break-up of all the bubbles (f). The larger bubble density in the lower branch is related to the difference in bubble size in the two channel branches. The larger bubbles resist more to flow and therefore move at a lower speed. At the highest P_g shown here, there is no visible influence of the ultrasound on the flow (g).

We will now try to interpret this result. For increasing P_g, pressure forces on a bubble grow. Initially the acoustic force deviates all the bubbles into the lower branch, but for increasing gas pressure P_g, bubbles start breaking up and finally, the flow in both branches becomes symmetric. So the observations in Fig. 5.6 correspond to an increase in the pressure force on a bubble. We can estimate the pressure gradient per bubble to be $\Delta P = (P_g - P_c)/N$, with $P_c = 1.5$ kPa the orifice contribution (see section 3.1.1) and N the number of bubbles in the channel. This leads to a force per bubble $F_b \approx \Delta P \times S$, with S the channel section. This allows us to estimate the order of magnitude of the acoustic force. We will assume that for the flow in Fig. 5.6d the pressure and acoustic force are approximately equal. Following this reasoning, the acoustic force $F_c = F_b \approx 0.3$ mN, much larger than the forces that can be achieved with *e.g.* an optical tweezer (typically a few pN).

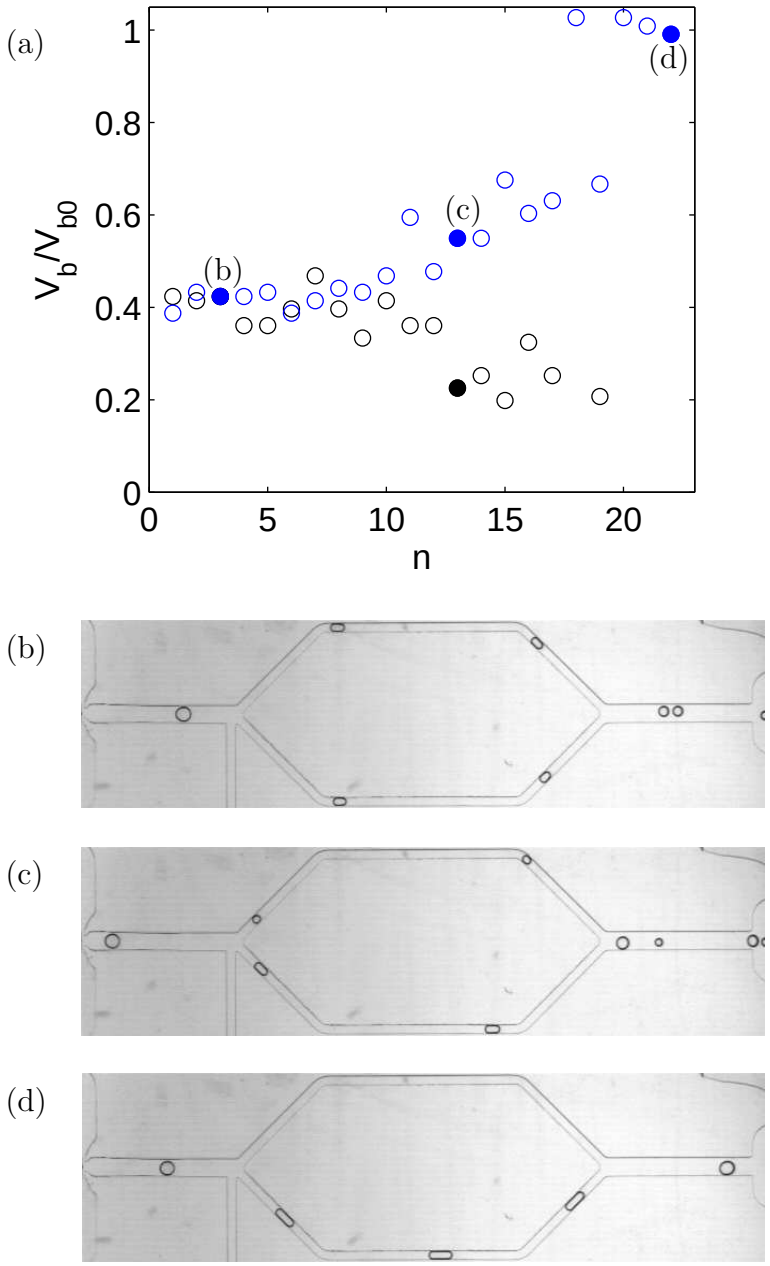

Figure 5.5: Controlled asymmetric bubble break-up by increasing the ultrasound amplitude from 0 to 30 V. (a) Bubble size (normalized by the bubble volume before break-up V_{b0}) *vs.* bubble number n. Blue symbols correspond to bubbles in the lower branch, black to the upper branch. For increasing ultrasound amplitude we encounter: (b) $V = 0$ V, unperturbed flow, bubble break-up in two equal parts, (c) intermediate V, asymmetric break-up, the largest part flows into the lower branch, (d) $V = 30$ V, no break-up, bubbles are entirely deviated downwards. The ultrasound frequency is set at $f = 143 \pm 1$ kHz, flow parameters: $Q_l = 250$ μl/min, $P_g = 3.90$ kPa.

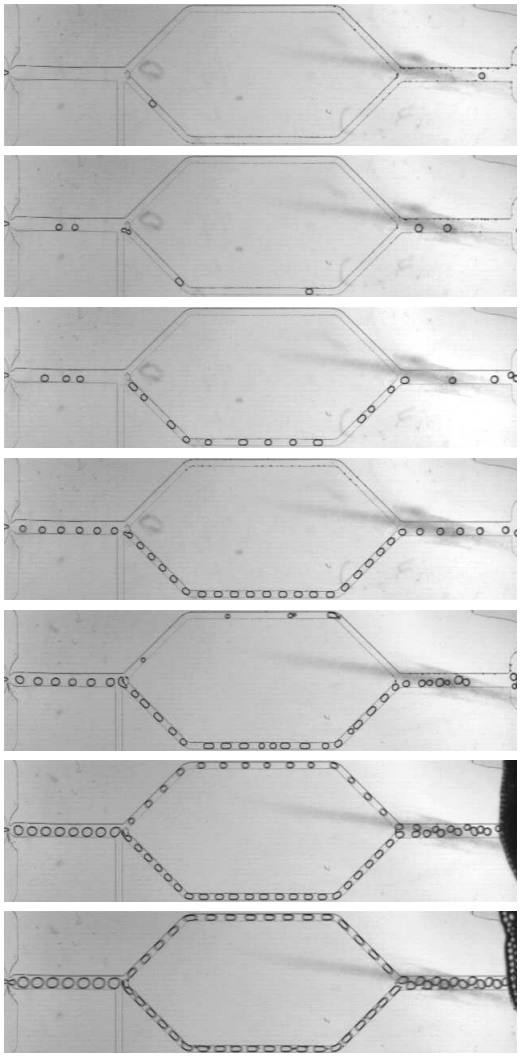

Figure 5.6: Competition between the pressure gradient and the acoustic force. Ultrasound parameters: $f = 139$ kHz and $V = 23.7$ V. Liquid flow rate: $Q_l = 430$ μl/min.

Secondary Bjerkness force: bubble clustering

Now we will turn to the secondary Bjerknes force which takes place between two oscillating bubbles. It is created by the hydrodynamic interaction between an oscillating bubble and the liquid flow field created by a second bubble. For bubbles oscillating in phase it leads to an attractive force. For the opposite case of oscillations in antiphase the force is repulsive. Bubbles oscillate in phase for both radii greater than, equal or less than R_0, so equally sized bubbles will always oscillate in phase and experience a mutually attractive force.

In our setup the attractive secondary Bjerknes force leads to a clustering effect, observed in a straight channel and at lower liquid fractions (see Fig. 5.7). In addition to this effect, the bubble cluster is attracted to one of the channel sides by the primary Bjerknes force.

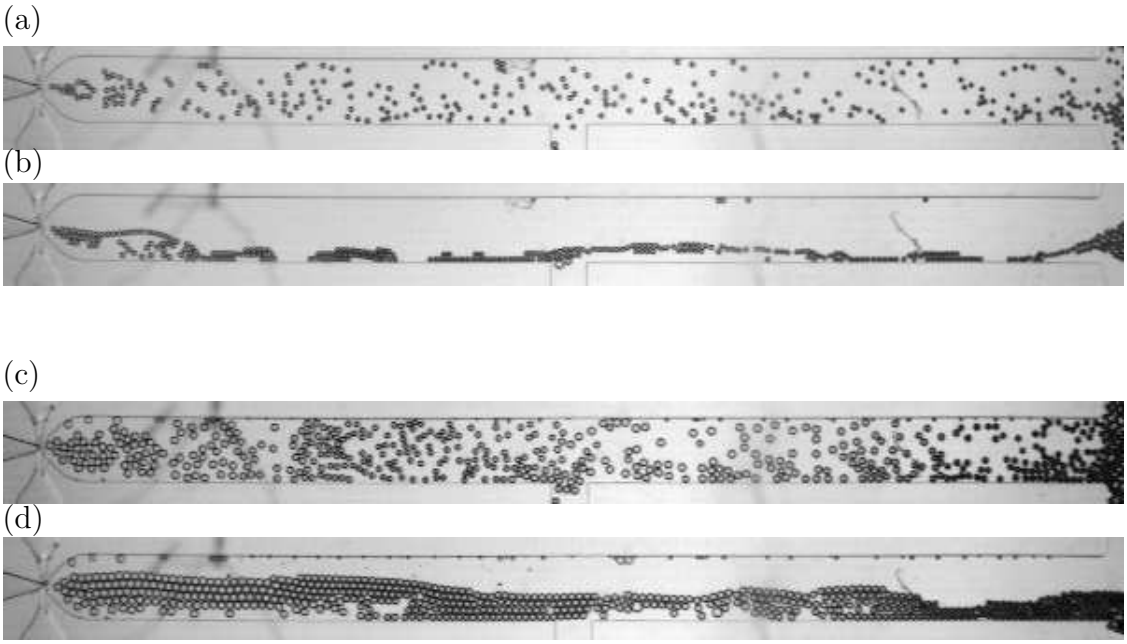

Figure 5.7: Bubbles in an unperturbed flow ((a) and (c)) cluster reversibly when the ultrasound is turned on ((b) and (d). Flow parameters: $P_g = 2.20$ kPa ((a) and (b)) and $P_g = 3.52$ kPa ((c) and (d)), $Q_l = 50$ μl/min. Ultrasound frequency $f = 125$ kHz and amplitude $V = 32$ V.

Possible applications

We showed in this chapter a method to apply forces on a bubbly flow. The use of acoustics, generated by a piezo element offers the advantages of low cost, straightforward implementation and easy miniaturization. Although the results

that we have presented here are very preliminary, we will speculate about the contexts in which it might be usefull:

- The primary Bjerknes force can be used to sort bubbles. Once the variation of the standing wave pattern in the glass plate with the ultrasound frequency is known, one can create zones of attraction and repulsion in a channel system. The localization of these zones is controlled by the ultrasound frequency. Furthermore they can be switched on and off on demand, allowing for a great flexibility in the guiding of bubbles on a microfluidic element.

- The secondary Bjerknes force leads to an attraction between bubbles. This actually creates a foam, by "squeezing" out the liquid. We therefore have a means to externally and dynamically controll one of the most important foam characteristics which is the liquid fraction.

- Bubbles in a bubbly flow move with respect to each other by complex hydrodynamical interactions (see *e.g.* [5] for bubbly flow in a geometry comparable to the one described here). A way to controll this flow is again by the clustering effect here presented. It leads to "packaging" between bubbles, that restrains relative motion.

5.3 Résumé

Jusqu'à maintenant nous avons discuté la génération et l'écoulement d'une micro-mousse. Dans le contexte des laboratoires-sur-puce on aimerait aussi avoir des moyens de manipulation de la mousse après sa formation. Dans ce chapitre nous présentons une façon passive et une façon active de ce genre de manipulation.

Dans le paragraphe 5.1 nous présentons une façon passive, donc sans moyens d'actuation extérieur, pour manipuler une mousse. Nous montrons le comportement d'une micro-mousse dans un canal qui se sépare en deux (jonction de type Y). En fonction de la topologie deux comportements différents de la mousse sont possible : les rang des bulles se séparent ou les bulles se divisent en deux parts. Ici l'interaction entre mousse et la géométrie du canal permet une opération de tri et une opération de brisure contrôlée.

La suite de ce chapitre est consacré à la manipulation active de l'écoulement à l'aide des forces ultrasonores. Un élément piézo-électrique nous permet de générer des ultrasons. Ces ultrasons créent une onde stationnaire dans la lame de verre qui constitue le fond de notre dispositif. Une bulle va osciller si on l'expose à des ultrasons avec une fréquence de résonance qui dépend de la taille des bulles. L'interaction entre une bulle oscillante et une onde de pression stationnaire donne lieu aux forces de Bjerkness. Les forces de Bjerknes primaires mènent à une attraction vers les noeuds de pression pour des bulles plus grandes que leur taille

de résonance, ce qui est notre cas. Pour des bulles de la même taille, la force de Bjerknes secondaire crée une force attractive entre bulles.

Nous utilisons les forces de Bjerknes primaire pour développer un système de aiguillage de bulles. Dans un géométrie avec une jonction de type Y, nous pouvons diriger les bulles dans l'une ou l'autre des deux branches de sorties en modifiant les fréquences du son. Ce dispositif permet également la division des bulles en deux morceaux asymétriques bien contrôlés en variant l'amplitude du transducteur. Nous montrons aussi l'effet des forces de Bjerknes secondaires. Elles conduisent à un effet d'aggrégation.

Chapter 6

Summary and outlook

6.1 Summary

This experimental thesis studies the generation, flow, and manipulation of a foam in a microchannel system.

After an introduction, in which we discussed the state of the art in both microfluidics and foam research, with which this thesis is a continuity, we described the ensemble of materials and methods that we have used during the experiments. We have described the different steps in microfabrication with the soft-lithography technique. After that we presented our experimental setup and control parameters: the gas pressure and liquid flow rate. Image analysis yields acces to bubble size, gas flow rate and foam topology. We have also showed some possibilities and limitations of the use of two photon microscopy for 3D imaging of a foam.

We studied the generation of microfoams (chapter 3). We first investigated for the standard regime of dry foam formation, how the input parameters determine the relation between bubble size and formation frequency. We then show that the bubble generation critically depends on the position of gas thread pinch-off. We have shown that the pinch-off position is governed either by the gas pressure, the liquid flow rate and by orifice length. For dry foam formation all three parameters must be above a certain threshold value. The driest foams are achieved for a pinch-off that is entirely confined to the orifice. Then we introduced the dimensionless topology parameter To, characterizing the link between channel geometry and foam topology.

In chapter 4 we showed that the microfoam flow is highly non-linear. The relation between pressure and flow rate presents a threshold, a power-law dependence and discontinuities upon the topology transitions. These discontinuities are related to the foam structure by a characteristic size L_p, namely the wall Plateau border length in the direction normal to the flow. The transition between F1 and F2 turns out to be rich. In the discontinuity region between F1 and F2,

we have observed three different transition mechanisms: (A) periodic topology oscillations, (B) topology coexistence and (C) both topology oscillation and coexistence. We claimed that the selection criterium between the mechanisms is based on the speed with which the foam topology can change. It takes place by means of a wave of T1s. The speed of this wave can either be larger, equal or smaller than that of the foam flow leading to (A) an absolute, (B) a stationary and (C) an advected wave respectively. Furthermore, for one specific geometry we have presented an experimental phase diagram. It suggests that higher liquid flow rates induce pressure driven drainage through the foam, a velocity difference between the gas and liquid speed. We have also observed compressible flows, either at high velocities or in very long channels. We found that in both cases the pressure drop can not be related directly to the volume increase. Possibly the effect of coarsening: the flow of gas through the liquid from high to low pressure bubbles.

Finally, in chapter 5 we have discussed two different methods, one passive and one active, to manipulate a microfoam. We have shown the behavior of a microfoam at an Y junction. Depending on the foam topology, upon reaching the junction, the foam either sorts or splits. Then we demonstrated how ultrasound can be employed to manipulate bubbles. A piezo-element creates a standing wave pattern in the glass slide to which the microchannel is glued. Due to the ultrasound, bubbles oscillate in volume. The interaction between an oscillating bubble and a standing pressure wave leads to two forces: the primary and secondary Bjerknes force. The primary Bjerknes force can be employed to create zones of attraction and repulsion in a channel sytem, thereby guiding the bubbles. The secondary Bjerknes force causes an attraction between bubbles, creating a clustering effect.

6.2 Outlook

The goal of this experimental work was to apply to foams the techniques and lengthscales of microfluidics and explore its resulting characteristics. It indicates numerous directions for future research.

- **Drainage** is an intensively studied phenomenon in a macrofoam [66]. It implies a flow of the liquid with respect to a foam sample. In 3D it is usually gravity driven and leads to an accumulation of water at the bottom of the foam. In section 4.3.2 we saw evidence indicating that for microfoams too the liquid flows with respect to the bubbles. This flow is not driven by gravity. A plausible candidate for the forcing mechanism seems to be the pressure (exerted by the syringe pump) to create the liquid flow. In agreement with this, the effect becomes more pronounced at higher gas (and thus liquid) pressures (section 4.3.2).

It would be interesting to study this effect quantitatively. In section 2.3 we saw the possibilities of two photon microscopy. Another promising approach might be the application of micro PIV, or measuring the liquid content by adding a fluorescent dye [37, 39].

- A better knowledge about the speed and **localization of the liquid** is also interesting in the context of (section 4.1.2) dissipation of a 2D foam [9, 60, 12, 13]. Models assume bubbles moving in a static liquid, which is not our case. Experimental data for the liquid flow could help adapting these models.

  Furthermore, these experiments could help to explain why substantial variations in the injected liquid fraction α_l do not lead to a big visible change in film and Plateau border thickness. For instance in section 4.2.2, Fig. 4.7, α_l varies between 4 % and 10 % without noticeable change in wall Plateau border thickness in the accompanying pictures. This effect can not only be related to drainage but also to the channel corners, that possibly accommodate easier to variations in the gas flow than other wall Plateau borders.

- Microfoams can be compressed, both at high speeds and in long channels. The volume increase we measured are however too large to be completely atributed to the total pressure drop between orifice and channel outlet (section 4.3.1). This might be due to **coarsening**, a gas flow from high to low pressure zones. Gas transports takes place through the films between bubbles. It might be interesting to investigate if, in microfoams, the fast liquid flow in the wall Plateau borders plays a role.

- It would be interesting to understand the transition from bubble formation to stratified gas liquid flow (section 4.2.4), in other words: the **high speed limit of foam formation**. It has been investigated at much lower continuous phase fractions, for oil-water systems in a T junction [33]; and in a co-flow geometry [34], where the transition was associated with the absolute or convective instability of the dispersed phase jet. It remains to be seen if such an analysis is correct for our dry foam case where we rather believe the transition to be related to the stability of the foam flow at high speed [50].

- The **instability** initiating the transition from an **F1 to an F2** foam in section 4.2.2 also remains a largely open question. At the moment of the transition, the F2 state has a lower energy than the metastable F1 state. This alone however is not enough to explain the transition, as a foam can remain indefinitely in a metastable state [66]. We invoked a wave-like motion superposed on the bubble flow, leading to an oscillation in the distance

between successive wall vertices (section 4.2.2 and 4.2.4). When two vertices touch a first T1 takes place. This T1 nucleates the F2 structure, which induces a second T1, and so on. We conjecture the wave-like motion to be related to an attractive interaction between films, driving the instability. It is opposed by surface tension: for instance the slanted films in Fig. 4.22 are more costly than films parallel to the channel section. Volume conservation implies that an increase in the distance between wall vertices on one channel side must be compensated by a decrease on the other side.

- The work on the interaction between bubbles and **ultrasound** (section 5.2) is still in a preliminary phase. David Rabaud, who is starting a PhD thesis in our lab, could try and control the **standing wave** pattern in the glass slide. It also remains an open question whether the Bjerknes forces (usually applied on isolated round bubbles) can be applied on a foam: the small liquid content might induce a modification of the bubbles response to ultrasound.

- The acoustic forces in section 5.2 act on the system as a whole. Going up to higher sound frequencies would lead to smaller wavelengths: for sound in water with $f = 15$ MHz, a wavelength $\lambda = 100$ μm can be reached. This would allow to use a liquid filled channel as a **waveguide**, to direct the sound to a specific location in the channel system. These high frequencies are three orders of magnitude larger than typical bubble resonance frequencies. So Bjerknes forces are excluded. The only action of sound might be due to the radiation pressure, that could possibly be used to push a bubble.

6.3 Perspectives

L'objective de ce travail expérimental était l'application aux mousses des techniques et des ordres de grandeurs typique de la microfluidique, et d'explorer les caractéristiques des mousses qui en résultent. Cette étude indique de nombreuses perspectives.

- Dans le paragraphe 4.3.2 nous avons trouvé des indices de l'existence de **drainage relatif**, une différence entre la vitesse moyenne du gaz et du liquide. Ce drainage est probablement dû au forçage du pousse-seringue. Une étude quantitative serait très intéressante, par exemple avec de l'aide de la microscopie à deux photons, de micro-PIV ou de mesures du contenu de liquide basées sur l'ajout d'un colorant fluorescent.

- De meilleures connaissances sur la vitesse et la **localisation du liquide** sont intéressantes dans le contexte de l'étude de la dissipation d'une mousse 2D (paragraphe 4.1.2). Les modèles supposent des bulles qui se propagent dans un liquide stagnant, ce que n'est pas notre cas. Des données

expérimentales pour l'écoulement du liquide peuvent être utiles pour adapter ces modèles.

- Les micro-mousses peuvent être comprimées, à la fois à haute vitesse et dans des canaux très longs. Pourtant, le changement de volume qu'on a mesuré est trop grand pour être complètement attribué à une décompression lié à la pression (paragraphe 4.3.1). Cela peut-être à cause du **vieillissement**, un flux de gaz d'une zone de haute vers une de basse pression. En général, le transport de gaz a lieu au travers des films de liquide. Il serait intéressant d'étudier si, dans le cas des micro-mousses, l'écoulement rapide de liquide dans les coins du canal joue un rôle.

- Il serait intéressant de comprendre la transition d'un régime avec la formation de bulles vers un écoulement de liquide et gaz stratifié (paragraphe 4.2.4), ou dans d'autre mots : **la limite supérieure en débit de gaz de la formation des micro-mousses**. Nous pensons cette limite d'être liée à la stabilité de l'écoulement de mousse à haute vitesse.

- L'**instabilité** qui initie la transition d'une mousse **F1 vers F2** reste une question ouverte. Nous supposons un attraction positive entre films, opposée par la tension de surface.

- Le travail sur l'interaction entre bulles et **ultrasons** (paragraphe 5.2) est encore dans une phase préliminaire. David Rabaud, qui commence une thèse dans notre laboratoire, essaye de mieux contrôler les ondes stationnaires dans la lame de verre. De même la question de savoir si les forces de Bjerknes sont applicables aussi sur une mousse et pas seulement à des bulles reste ouverte.

- Monter la fréquence des ultrasons pourrait permettre l'utilisation d'un **guide d'onde** pour diriger les ultrasons vers un endroit spécifique du système. Cela permettrait une application locale des forces.

Appendix A

Channel geometries

This appendix recollects all the different channel geometries used in this thesis. The figures correspond to the actual drawings used for the lithography masks, with a 3× magnification. The figure captions give values for the most important geometrical parameters.

Figure A.1: Classic geometry. $h = 250$ μm, $w_{or} = 100$ μm, $l_{or} = 400$ μm, $w = 700$ μm, $L = 17$ mm.

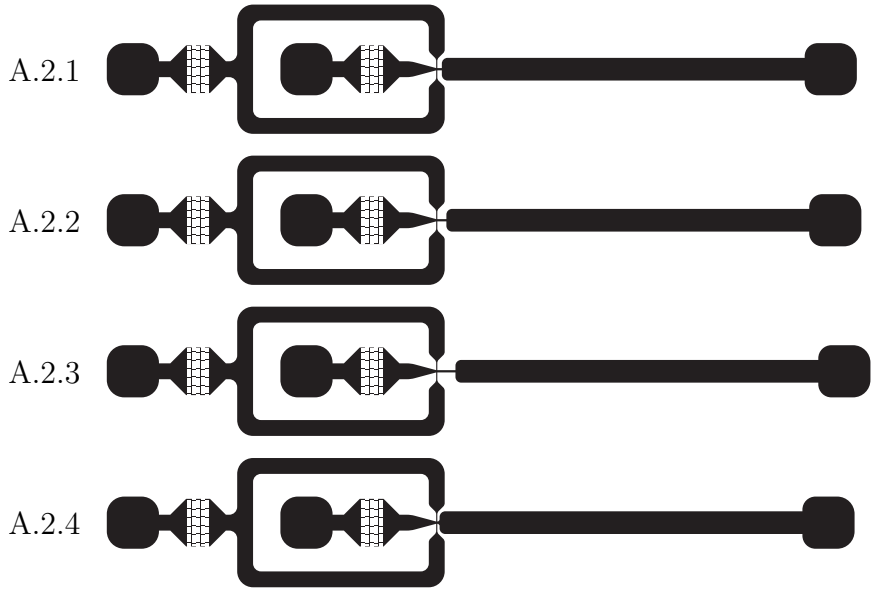

Figure A.2: Adapted orifice geometry. $h = 100$ μm, $w_{or} = 100$ μm, $w = 1000$ μm, $L = 16$ mm, A.2.1: $l_{or} = 200$ μm, A.2.2: $l_{or} = 400$ μm, A.2.3: $l_{or} = 800$ μm, A.2.4: $l_{or} \simeq 50$ μm.

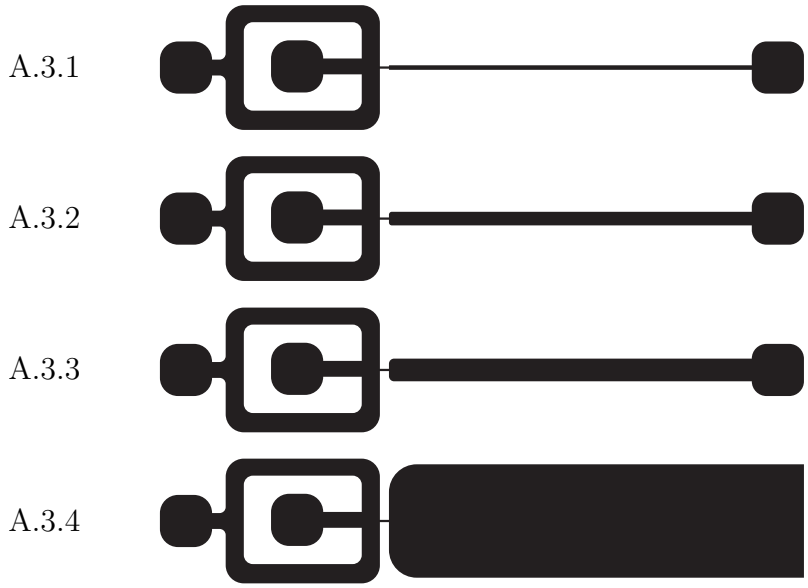

Figure A.3: Varying channel width w. $h = 100$ μm, $w_{or} = 100$ μm, $l_{or} = 400$ μm, $L = 16$ mm, A.3.1: $w = 200$ μm, A.3.2: $w = 600$ μm, A.3.3: $w = 1000$ μm, A.3.4: $w = 5000$ μm.

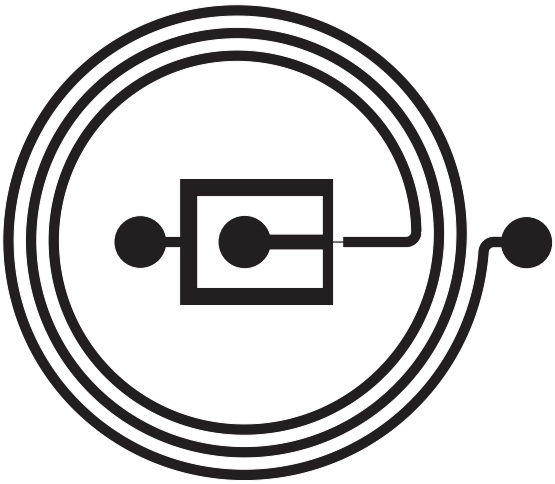

Figure A.4: Ultralong channel. $h = 75$ μm, $w_{or} = 100$ μm, $l_{or} = 400$ μm, $w = 500$ μm, $L = 18$ cm.

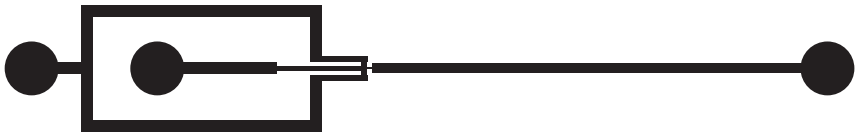

Figure A.5: Ultraflat channel. $h = 8$ μm, $w_{or} = 75$ μm, $l_{or} = 200$ μm, $w = 400$ μm, $L = 20$ mm.

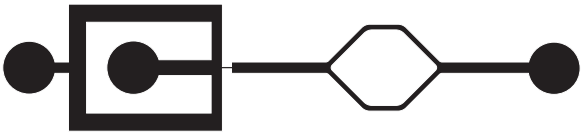

Figure A.6: Y junction. $h = 100$ μm, $w_{or} = 100$ μm, $l_{or} = 400$ μm, outlet width $w_1 = 500$ μm, branch width $w_2 = 250$ μm, $L = 13$ mm.

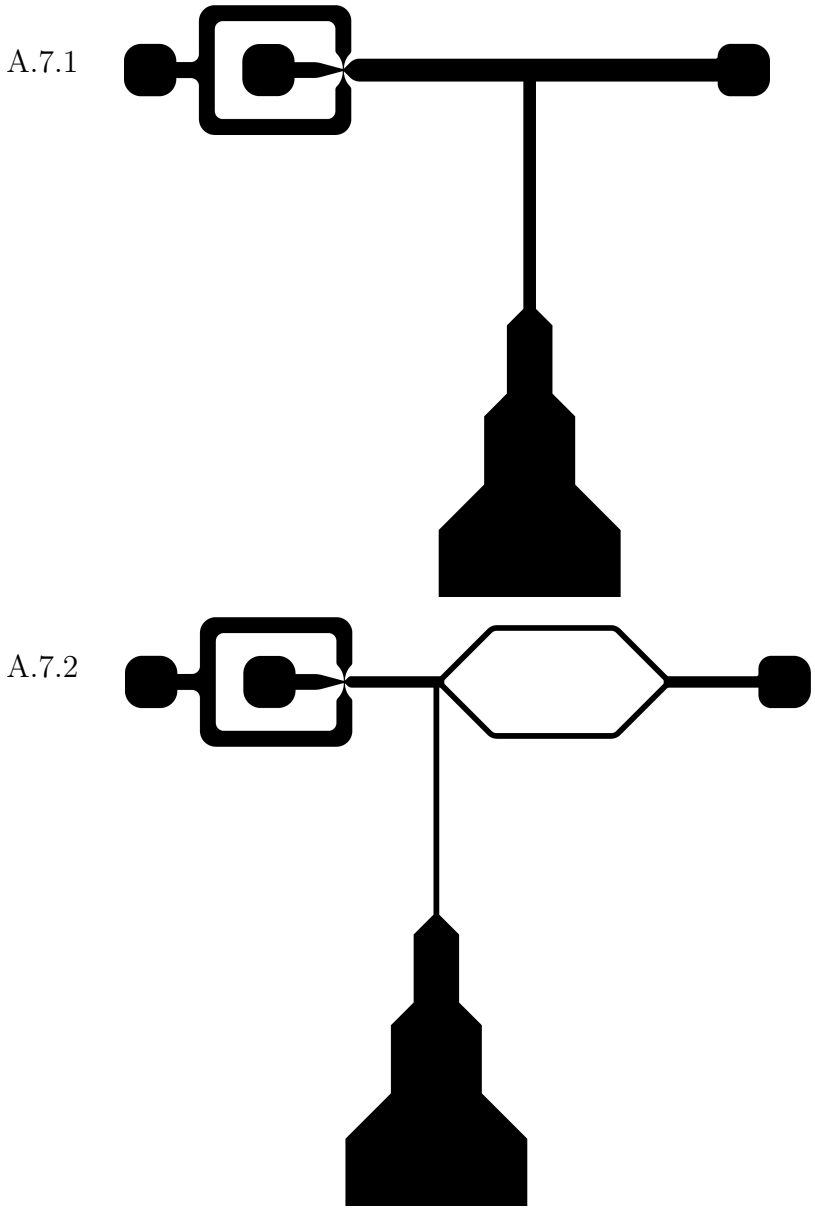

Figure A.7: Ultrasound. $h = 100$ μm, $w_{or} = 100$ μm, $l_{or} \simeq 50$ μm. A.7.1: $w = 1000$ μm, branch width $w_2 = 250$ μm. A.7.2: outlet width $w_1 = 500$ μm.

Bibliography

[1] M. Abkarian, M. Faivre, and H. A. Stone. High-speed microfluidic differential manometer for cellular-scale hydrodynamics. *PNAS*, 103:538–542, 2006.

[2] S. L. Anna, N. Bontoux, and H.A. Stone. Formation of dispersions using "flow focusing" in microchannels. *Appl. Phys. Lett.*, 82:364–366, 2003.

[3] V. Barbier, M. Tatoulian, H. Li, F. Arefi-Khonsari, A. Ajdari, and P. Tabeling. Stable modification of pdms surface properties by plasma polymerization: Application to the formation of double emulsions in microfluidic systems. *Langmuir*, 22(12):5230–5232, June 2006.

[4] V. Barbier, H. Willaime, P. Tabeling, and F. Jousse. Producing droplets in parallel microfluidic systems. *Phys. Rev. E*, 74:046306, 2006.

[5] T. Beatus, T. Tlusty, and R. Bar-Ziv. Phonons in a one-dimensional microfluidic crystal. *Nature phys.*, 2:743–748, 2006.

[6] F. Bolton and D. Weaire. Rigidity loss transition in a disordered 2d froth. *Phys. Rev. Lett.*, 65:3449–3451, 1990.

[7] F. P. Bretherton. The motion of long bubbles in tubes. *J. Fluid Mech.*, 10:166–188, 1961.

[8] I. Cantat and R. Delannay. Dissipative flows of 2d foams. *Eur. Phys. J. E*, 18:55–67, 2005.

[9] I. Cantat, N. Kern, and R. Delannay. Dissipation in foam flowing through narrow channels. *Europhys. Lett.*, 65:726–732, 2004.

[10] G. F. Christopher and S. L. Anna. Microfluidic methods for generating continuous droplet streams. *Journal of Physics D: Applied Physics*, preprint.

[11] C. Cramer, P. Fischer, and E. J. Windhab. Drop formation in a co-flowing ambient fluid. *Chem. Eng. Sc.*, 59:3045–3058, 2004.

[12] N. D. Denkov, V. Subramanian, D. Gurovich, and A. Lips. Wall slip and viscous dissipation in sheared foams: Effect of surface mobility. *Colloids and Surfaces A*, 263:129–145, 2005.

[13] N. D. Denkov, S. Tcholakova, K. Golemanov, and V. Subramanian A. Lips. Foam-wall friction: Effect of air volume fraction for tangentially immobile bubble surface. *Colloids and Surfaces A*, 282-283:329–347, 2005.

[14] B. Dollet, F. Elias, C. Quillet, A. Huillier, M. Aubouy, and F. Graner. Two-dimensional flows of foam: drag exerted on circular obstacles and dissipation. *Colloids and Surfaces A*, 2005.

[15] B. Dollet and F. Graner. Two-dimensional flow of foam around a circular obstacle: local measurements of elasticity, plasticity and flow. *J. Fluid Mech.*, 585:181–211, 2007.

[16] B. Dollet, W. van Hoeve, J-. P. Raven, P. Marmottant, and M. Versluis. Role of the channel geometry on the bubble pinch-off in flow focusing devices. *preprint*, 2007.

[17] Benjamin Dollet. *Ecoulements bidimensionnels de mousses autour d'obstacles*. PhD thesis, Université Joseph Fourier - Grenoble I, 2005.

[18] Benjamin Dollet, Miguel Aubouy, and François Graner. Anti-inertial lift in foams: A signature of the elasticity of complex fluids. *Phys. Rev. Lett.*, 95:168303, 2005.

[19] W. Drenckhan, S. J. Cox, H. Holste, D. Weaire, and N. Kern. Rheology of ordered foams-on the way to discrete microfluidics. *Colloids Surf. A*, 263:52–64, 2005.

[20] D. C. Duffy, J. C. McDonald, O. J. A. Schueller, and G. M. Whitesides. Rapid prototyping of microfluidic systems in poly(dimethylsiloxane). *Anal. Chem.*, 70:4974–4984, 1998.

[21] M. Durand and H. A. Stone. Relaxation time of the topological t1 process in a two-dimensional foam. *Phys. Rev. Lett.*, 97:226101, 2006. cond-mat/0608426.

[22] Wilfried Engl, Matthieu Roche, Annie Colin, Pascal Panizza, and Armand Ajdari. Droplet traffic at a simple junction at low capillary numbers. *Phys. Rev. Lett.*, 95:208304, 2006.

[23] P. Garstecki, M. A. Fischbach, and G. M. Whitesides. Design for mixing using bubbles in branched microfluidic channels. *Appl. Phys. Lett.*, 86:244108, 2005.

[24] P. Garstecki, M. J. Fuerstman, M. A. Fischbach, S. K. Sia, and G. M. Whitesides. Mixing with bubbles: a practical technology for use with portable microfluidic devices. *Lab Chip*, 6:207–212, 2006.

[25] P. Garstecki, M. J. Fuerstman, H. A. Stone, and G. M. Whitesides. Formation of droplets and bubbles in a microfluidic t-junction-scaling and mechanism of break-up. *Lab chip*, 6:437–446, 2006.

[26] P. Garstecki, H. A. Stone, and G. M. Whitesides. Auxiliary material to: Mechanism for flow-rate controlled breakup in confined geometries: a route to monodisperse emulsions. *EPAPS Document E-PRLTAO-94-026518*, 2005.

[27] Piotr Garstecki, Micheal J. Fuerstman, and George M. Whitesides. Nonlinear dynamics of a flow-focusing bubble generator: An inverted dripping faucet. *Phys. Rev. Lett.*, 94:234502, 2005.

[28] Piotr Garstecki, Irina Gitlin, Willow DiLuzio, George M. Whitesides, Eugenia Kumacheva, and Howard A. Stone. Formation of monodisperse bubbles in a microfluidic flow-focusing device. *Appl. Phys. Lett.*, 85(13):2649–2651, 2004.

[29] Piotr Garstecki, Howard A. Stone, and George M. Whitesides. Mechanism for flow-rate controlled breakup in confined geometries: A route to monodisperse emulsions. *Phys. Rev. Lett.*, 94:164501, 2005.

[30] Alfonso M. Gañán-Calvo. Perfectly monodisperse microbubbling by capillary flow focusing: An alternate physical description and universal scaling. *Phys. Rev. E*, 69:027301, 2004.

[31] Alfonso M. Gañán-Calvo and Jose M. Gordillo. Perfectly monodisperse microbubbling by capillary flow focusing. *Phys. Rev. Lett.*, 87:274501, 2001.

[32] F. Graner. La mousse. *La Recherche*, 345:46–49, 2001.

[33] P. Guillot and A. Colin. Stability of parallel flows in a microchannel after a t junction. *Phys. Rev. E*, 72:066301, 2005.

[34] P. Guillot, A. Collin, A. S. Utada, and A. Ajdari. Stability of a jet in confined pressure-driven biphasic flows at low reynolds number. *Phys. Rev. Lett.*, preprint, 2007.

[35] P. Guillot, P. Panizza, J.-B. Salmon, M. Joanicot, A. Collin, C.-H. Bruneau, and T. Colin. Viscosimeter on a microfluidic chip. *Langmuir*, 22:6438–6455, 2006.

[36] J. Husny and J. J. Cooper-White. The effect of elasticity on drop creation in t-shaped microchannels. *J. Non-Newtonian Fluid Mech.*, 137:121–136, 2006.

[37] Stephan A. Koehler, Sascha Hilgenfeldt, and Howard A. Stone. Liquid flow through aqueous foams: The node-dominated foam drainage equation. *Phys. Rev. Lett.*, 82(21):4232, May 1999.

[38] J. Lambert, I. Cantat, R. Delannay, G. Le Caër, A. Renault, S. Ruellan, F. Graner, S. Jurine, P. Cloetens, and J. A. Glazier. Extraction of relevant physical parameters from 3d images of foams obtained by x-ray tomography. *Coll. Surf. A.*, 263:295–302, 2005.

[39] T. Lauffenburger. Stage de m1: Drainage dans une micromousse. Master's thesis, INPG, Grenoble, 2006.

[40] T. G. Leighton. *The acoustic bubble*. Academic Press, 1994.

[41] P. Lenz, C.M. Ajo-Franklin, and S.G. Boxer. Patterned supported lipid bilayers and monolayers on poly(dimethylsiloxane). *Langmuir*, 20(25):11092–11099, 2004.

[42] D. R. Link, S. L. Anna, D. A. Weitz, and H. A. Stone. Geometrically mediated breakup of drops in microfluidic devices. *Phys. Rev. Lett.*, 92:054503, 2004.

[43] Elise Lorenceau, Yann Yip Cheung Sang, Reinhard Höhler, and Sylvie Cohen-Addad. A high rate flow-focusing foam generator. *Physics of fluids*, 18:097103, 2006.

[44] J. Cooper McDonald, David C. Duffy, Janelle R. Anderson, Daniel T. Chiu, Hongkai Wu, Olivier J.A. Schueller, and George M. Whitesides. Fabrication of microfluidic systems in poly(dimethylsiloxane). *Electrophoresis*, 21:27–40, 2000.

[45] L. Ménétrier-Deremble and Patrick Tabeling. Droplet breakup in microfluidic junctions of arbitrary angles. *Phys. Rev. E*, 74:035303(R), 2006.

[46] M. Minnaert. On musical air-bubbles and sounds of running water. *Phil Mag*, 16:235–248, 1933.

[47] M. Prakash and N. Gershenfeld. Microfluidic bubble logic. *Science*, 315:832–835, 2007.

[48] H. M. Princen. Rheology of foams and highly concentrated emulsions: I elastic properties and yield stress of cylindrical model system. *J. Coll. Interf. Sci.*, 91(1):160–175, 1983.

[49] Stephen R. Quake and Axel Sherer. From micro- to nanofabrication with soft materials. *Science*, 290:1536–1540, 2000.

[50] C. Raufaste. *Rheologie et imagerie des ecoulements 2D de mousse: approche experimentale, numerique et theorique*. PhD thesis, Universite Grenoble I, 2007.

[51] C. Raufaste, B. Dollet, S. Cox, Y. Jiang, and F. Graner. Yield drag in a two-dimensional foam flow around a circular obstacle: Effect of the liquid fraction. *Eur. Phys. J. E*, 23:217–228, 2007.

[52] A. Saugey, W. Drenckhan, and D. Weaire. Wall slip of bubbles in foams. *Phys. Fluids*, 18, 2006.

[53] I. Shestopalov, J. D. Tice, and R. F. Ismagilov. Multi-step synthesis of nanoparticles performed on millisecond time scale in a microfluidic droplet-based system. *Lab Chip*, 4:316–321, 2004.

[54] C. S. Smith. On blowig bubbles for bragg's dynamic crystal model. *Appl. Phys. Lett.*, 20:631, 1949.

[55] H. Song, J. D. Tice, and R. F. Ismagilov. A microfluidic system for controlling reaction networks in time. *Angew. Chem. Int. Ed.*, 42:768–771, 2003.

[56] Todd M. Squires and Stephen R. Quake. Microfluidics: Fluid physics at the nanoliter scale. *Rev. Mod. Phys.*, 77:977, 2005.

[57] H.A. Stone, A.D. Stroock, and A. Ajdari. Engineering flows in small devices: microfluidics toward a lab-on-a-chip. *Annu. Rev. Fluid. Mech.*, 36:381–411, 2004.

[58] Patrick Tabeling. *Introduction à la microfluidique*. Belin, 2003.

[59] S. Takeuchi, P. Garstecki, D.B. Weibel, and G.M. Whitesides. An axisymmetric flow-focusing device. *Advanced Materials*, 17:1067–1072, 2005.

[60] E. Terriac, J. Etrillard, and I. Cantat. Viscous force exerted on a foam at a solid boundary: Influence of the liquid fraction and of the bubble size. *Europhys. Lett.*, 74:909–915, 2006.

[61] T. Thorsen, R. W. Roberts, F. H. Arnold, and S. R. Quake. Dynamic pattern formation in a vesicle-generating microfluidic device. *Phys. Rev. Lett.*, 86:4163–4166, 2001.

[62] Marc A. Unger, Hou-Pu Chou, Todd Thorsen, Axel Scherer, and Stephen R. Quake. Monolithic microfabricated valves and pumps by multilayer soft lithography. *Science*, 288:113–116, 2000.

[63] A.S. Utada, E. Lorenceau, D.R. Link, P.D. Kaplan, H.A. Stone, and D.A. Weitz. Monodisperse double emulsions generated from a microcapillary device. *Science*, 308:537–541, 2005.

[64] A. van der Net, L. Blondel, A. Saugey, and W. Drenckhan. Simulating and interpretating images of foams with computational ray-tracing techniques. *Colloids Surf. A: Physicochem. Eng. Aspects (2007)*, In press:xx, 2006.

[65] Willem van Hoeve. Monodisperse microbubble formation in microfluidic flow-focusing devices. Master's thesis, University of Twente, The Netherlands, 2006.

[66] D. Weaire and S. Hutzler. *The physics of foams.* Oxford University Press, Oxford, 1999.

[67] G. M. Whitesides. The origins and the future of microfluidics. *Nature*, 442:368–373, 2006.

[68] www.flowfocusing.com.

Résumé

Cette thèse se situe à la frontière de deux domaines : celui de la rhéologie des mousses et celui de la microfluidique. On présente comment créer une mousse dans un système microfluidique avec une taille minimale de bulle autour de 100 μm et on étudie son écoulement. Après un rappel de l'état de l'art en microfluidique biphasique et dans le domaine de l'écoulement de mousse 2D, on présente l'ensemble de techniques expérimentales qui permettent de produire le système microfluidique et d'imager l'écoulement résultant. Ensuite, on étudie la génération de mousse microfluidique avec la méthode du pincement liquide. On mesure la dépendance des propriétés de la mousse (fraction liquide, topologie) envers les paramètres de contrôle et la géométrie. Nous montrons que la rhéologie l'écoulement est fortement non-linéaire. La relation pression-débit présente en effet un seuil, une loi de puissance et des discontinuités liés aux transitions de topologie. On met en évidence un effet rétroactif de l'écoulement dans le canal sur la formation de la mousse, qui entraîne un comportement dynamique très riche. On trouve notamment une oscillation entre différentes topologies reliée à une instabilité qui peut être de type advectif, stationnaire ou absolu. Finalement on étudie une méthode pour l'application de forces acoustiques sur un écoulement biphasique, afin de manipuler les bulles de la mousse depuis l'extérieur.

Abstract

This thesis is on the edge of two domains: foam rheology and microfluidics. We present how to create a foam in a microfluidic channel system with a typical smallest dimension for the bubbles of 100 μm and we study its flow. After recalling the state of the art in two-phase microfluidics and 2D foam flows, we present the ensemble of experimental techniques that allow to produce the channel system and image the resulting flow. Then, we investigate microfluidic foam generation using the flow focusing technique. We measure the dependence of the foam properties (liquid fraction, topology) on the input parameters and geometry. We show that the rheology of the foam flow is very non-linear. The pressure-flow rate relation notably presents a threshold, a power law, and discontinuities related to topology transitions. We bring into evidence a retroactive effect of the flow in the channel on foam formation, that leads to a rich dynamical behaviour. We notably find an oscillation between different topologies that we relate to an instability that can either be advected, stationary or absolute. We eventually investigate a method to apply forces on the two-phase flow by ultrasound, to manipulate the foam externally.